

LARGE-EDDY SIMULATIONS OF TURBULENT FLOWS IN INTERNAL
COMBUSTION ENGINES

By

Araz Banaeizadeh

A DISSERTATION

Submitted to
Michigan State University
in partial fulfillment of the requirements
for the degree of

DOCTOR OF PHILOSOPHY

Mechanical Engineering

2010

ABSTRACT

**LARGE-EDDY SIMULATIONS OF TURBULENT FLOWS IN
INTERNAL COMBUSTION ENGINES**

By

Araz Banaeizadeh

The two-phase compressible scalar filtered mass density function (FMDF) model is further developed and employed for large-eddy simulations (LES) of turbulent spray combustion in internal combustion (IC) engines. In this model, the filtered compressible Navier-Stokes equations are solved in a generalized curvilinear coordinate system with high-order, multi-block, compact differencing schemes for the turbulent velocity and pressure. However, turbulent mixing and combustion are computed with a new two-phase compressible scalar FMDF model. The spray and droplet dispersion/evaporation are modeled with a Lagrangian method. A new Lagrangian-Eulerian-Lagrangian computational method is employed for solving the flow, spray and scalar equation. The pressure effect in the energy equation, as needed in compressible flows, is included in the FMDF formulation.

The performance of the new compressible LES/FMDF model is assessed by simulating the flow field and scalar mixing in a rapid compression machine (RCM), in a shock tube and in a supersonic co-axial jet. Consistency of temperatures predicted by the Eulerian finite-difference (FD) and Lagrangian Monte Carlo (MC) parts of the LES/FMDF model are established by including the pressure on the FMDF. It is shown that the LES/FMDF model is able to correctly capture the scalar mixing in both compressible subsonic and supersonic flows.

Using the new two-phase LES/FMDF model, fluid dynamics, heat transfer, spray and combustion in the RCM with flat and crevice piston are studied. It is shown that the temperature distribution in the RCM with crevice piston is more uniform than the RCM with flat piston. The fuel spray characteristics and the spray parameters

affecting the fuel mixing inside the RCM in reacting and non-reacting flows are also studied. The predicted liquid penetration and flame lift-off lengths for respectively non-reacting and reacting sprays are found to compare well with the available experimental data. Temperatures and evaporated fuel mass fractions as predicted by the LES-FD and FMDF-MC for both reacting and non-reacting cases are shown to be consistent inside the RCM.

Several non-reacting and reacting flows relevant to IC engines are also simulated with the new two-phase LES/FMDF model. The non-reacting flows in three geometrical configurations are considered: (1) a poppet valve in a sudden expansion, (2) a simple piston-cylinder assembly with a stationary open valve and harmonically moving flat piston, and (3) a realistic 3-valve single-cylinder direct-injection spark-ignition engine. The first and the second configurations are considered for validation of LES and for better understanding of the large-scale unsteady flow motions around the valve in the cylinder as generated by the piston movement. The predicted flow statistics by LES for the first two configurations compare well with the available experimental data. The LES results for third flow configuration show significant cycle-to-cycle variations (CCV) in the velocity field but insignificant CCV in the thermodynamic variables. During the intake stroke, the in-cylinder flow is highly inhomogeneous and turbulent, but during the compression stroke the flow becomes more homogeneous as turbulent decays. Turbulent mixing and combustion (with and without spray) in the 3-valve engine are simulated using the new two-phase compressible LES/FMDF model. Consistency of LES and FMDF results for single-phase reacting flows without spray but with flame ignition and premixed flame propagation, and two-phase reacting flows with spray, mixing and non-premixed combustion indicates the applicability and accuracy of the LES/FMDF model for complex turbulent combustion systems with moving boundaries.

To my father
whose memories are always vivid in my mind

ACKNOWLEDGMENT

I am sincerely grateful to my advisor Professor Farhad Jaber for his support, patience, encouragement and guidance. My knowledge in turbulent flows and turbulence modeling specifically large-eddy simulation and filtered mass density function was not achievable without his supervision. I would also like to appreciate the members of my doctoral committee, Professors Charles Petty, Harold Schock, Guowei Wei and Tonghun Lee for their constructive comments.

This work is supported by the US Department of Energy under agreement number DE-FC26-07NT43278 and the National Aeronautics and Space Administration under the contract number NNX07AC50A. Additional support was provided by the Michigan Economic Development Corporation (MEDC). All computations are conducted on the supercomputer machines at the High Performance Computing Center at Michigan State University.

I owe my deepest gratitude to my partner, companion, best friend, ..., Anoosheh. During my MS and PhD studies, I have learned so many things from her; how to be a good researcher and how to have a good life due to her perfectionist character.

It is an honor for me to show my appreciation to my parents. My father used to encourage me to go to the graduate school since I was a student in the elementary school. My mother's prayers have always followed me. My parents did whatever they could to eliminate the source of concerns that I face in my life and help me focus on my studies.

It is a pleasure to thank my brothers, they always supported their younger brother emotionally, educationally and financially.

TABLE OF CONTENTS

List of Tables	viii
List of Figures	ix
Nomenclature	xvi
1 Introduction	1
2 Mathematical formulations and numerical solution	3
2.1 Governing equations	3
2.1.1 Filtered LES equations	3
2.1.2 Compressible two-phase FMDF	7
2.1.3 Lagrangian fuel droplets	12
2.2 Numerical solution procedure	13
3 Compressible Scalar FMDF for LES of High speed Turbulent Flows	19
3.1 Introduction	19
3.2 Results	22
3.2.1 Rapid compression machine	22
3.2.2 Shock tube	23
3.2.3 Co-axial helium-air jet	25
3.3 Conclusions	28
4 LES of fluid flow and combustion in RCMs	49
4.1 Introduction	49
4.2 Results	52
4.2.1 Non-reacting flows	52
4.2.2 Reacting flows without spray	56
4.2.3 Reacting flows with spray	57
4.3 Conclusions	61
5 LES of turbulent flow and spray combustion in IC engines	81
5.1 Introduction	81
5.2 Results	84
5.2.1 Non-reacting flows	85
5.2.1.1 Sudden expansion with a poppet valve	85
5.2.1.2 Piston-cylinder assembly with an intake/exhaust valve	86
5.2.1.3 Three-valve DISI engine	88
5.2.2 Reacting flows	93
5.2.2.1 Reacting flow without spray	94

5.2.2.2	Spray combustion in DISI engine	96
5.3	Conclusions	99
6	Summary and conclusions	132
	Bibliography	135

LIST OF TABLES

- 4.1 Four spray experimental conditions used in the RCM. For all cases, gas phase temperature and density are $1000K$ and $14.8Kg/m^3$, respectively. 60

LIST OF FIGURES

2.1	For interpretation of the references to color in this and all other figures, the reader is referred to the electronic version of this dissertation. (a) Elements of hybrid two-phase LES/FMDF methodology. (b) A two-dimensional view of a portion of the LES/FMDF computational domain; solid black thick lines show a sample ensemble domain, FD cells are specified by the blue lines, the solid smaller circles are sample MC particles, and the solid larger circles are sample liquid droplets. .	18
3.1	(a) Experimental set-up of the rapid compression machine (RCM) [58]. (b) 3-dimensional and 2-dimensional views of the 2-block grid used for the RCM simulation.	29
3.2	(a) Temperatures obtained from the finite difference (FD) and Monte Carlo (MC) data at different piston locations during the compression in the rapid compression machine. (b) Different piston locations during the compression.	30
3.3	Comparison of (a) pressures and (b) velocities obtained by the FD with artificial viscosity (solid lines with solid triangular symbols) and without artificial viscosity (solid lines with hollow triangular symbols) with the analytical solutions (solid lines no symbol) for Sod's shock tube problem.	32
3.4	Comparison of temperatures, obtained by the FD, MC without $'D\bar{p}/Dt'$, MC with $'\partial\bar{p}/\partial t'$, MC with limiter on $'D\bar{p}/Dt'$ for the Sod shock tube problem.	33
3.5	Comparison of LES-FD filtered densities with the MC particle weighted number density calculated by Eq. (2.36) with (a) 6, (b) 24 and (c) 48 MC particles per cell. (d) Comparison of LES density with MC density calculated by Eq. (2.38).	34

3.6	(a) Geometrical details of the supersonic co-annular jet (Dimensions given in mm), and (b) three-dimensional and two-dimensional views of the 6-block grid.	36
3.7	Instantaneous (a) three-dimensional and (b) two-dimensional contour plots of vorticity for the supersonic co-annular jet.	37
3.8	Instantaneous contours of the scalar at central region of the flow, the downstream of nozzles as predicted by the (a) Smagorinsky and (b) MKEV models. (c) Comparison of the mixing layer thickness predicted by the MKEV model (dashed line with the square symbols) and the Smagorinsky model (dashed double dot line with the triangle symbols) with the experimental data (solid line with diamond symbols). . . .	37
3.9	Comparison of time-averaged axial velocity as predicted by the MKEV model (solid lines) and the Smagorinsky model (dashed double dot lines) with the experimental data (symbols) at different radial (r) and axial (X) locations.	38
3.10	Comparison of the root mean square values of axial velocity, predicted by the MKEV (solid lines) and the Smagorinsky model (dashed double dot lines), with the experimental data (symbols).	39
3.11	Instantaneous two-dimensional contour plots of filtered temperature predicted by the (a) LES-FD, (b) FMDF-MC, and instantaneous contour plots of the scalar mass fraction predicted by the (c) LES-FD, (d) FMDF-MC.	40
3.12	(a) Scatter plots of the temperature predicted by LES-FD and FMDF-MC with " $D \langle p \rangle_l / Dt$ ". (b) Scatter plots of scalar mass fraction predicted by LES-FD and FMDF-MC. (c) Scatter plots of the temperature, predicted by LES-FD and FMDF-MC without " $D \langle p \rangle_l / Dt$ ". The solid lines are the 45° lines. "R" denotes the correlation coefficient. .	41
3.13	(a) Time-averaged contours of " $\langle u_j \rangle_L \partial \langle p \rangle_l / \partial x_j$ " term downstream of the nozzles. (b) Scatter plots of the temperature versus " $\langle u_j \rangle_L \partial \langle p \rangle_l / \partial x_j$ " term.	43
3.14	Time-averaged contours of $He-O_2$ mass fraction predicted by (a) LES-FD, (b) FMDF-MC. (c) Comparison of the time-averaged $He-O_2$ mass fraction, obtained with the LES-FD and MKEV model (solid lines), LES-FD and Smagorinsky model (dashed dot lines) and FMDF-MC model (dashed dot lines with hollow symbols) with the experimental data (solid symbols).	45

3.15	Time-averaged values of the filtered temperature predicted by the LES-FD (solid lines) and the FMDF-MC (dashed dot lines with hollow symbols). $T_{ref} = 300$	47
3.16	Root mean square values of the filtered (a) scalar mass fraction and (b) temperature predicted by the LES-FD (solid lines) and the FMDF-MC (dashed dot lines with hollow symbols). $T_{ref} = 300$	48
4.1	(a) Experimental set-up of the rapid compression machine (RCM) [58] and 3-dimensional view of the 4-block grid used for the RCM simulation. (b) 2-dimensional views of the grids employed in the cylinder part and crevice section.	63
4.2	Iso-levels of temperature at -5 msec. for (a) flat and (b) crevice piston.	64
4.3	2D temperature contour plots, at (a) -15, (b) -5, (c) 0 and (d) +5 milliseconds for the flat piston as predicted by the LES-FD and FMDF-MC.	65
4.4	2D temperature contour plots, at (a) -15, (b) -5, (c) 0 and (d) +5 milliseconds for the crevice piston as predicted by the LES-FD and FMDF-MC.	67
4.5	Predicted temperature values along a radial line in the central plane and comparison with the experimental data for (a) flat and (b) crevice piston.	69
4.6	Predicted Volume averaged pressure during compression and combustion for two cases of (a) and (b) and compared with the experimental data. (a): simulation with the pre-exponential value provided in Ref. [90] and (b): with pre-exponential value 3 times larger than (a).	70
4.7	2D contours of FMDF-MC temperature in two planes parallel and perpendicular to the piston during the autoignition and the flame propagation of ethanol for the crevice piston.	71
4.8	(a) 2D contours of LES-FD temperature at same time shown in Fig. 4.7(d). (b) Scatter plots of LES-FD and FMDF-MC temperatures.	73
4.9	(a) Schematic cross section of the Sandia combustion vessel, (b) 3D view of computational domain and fuel particles.	74

4.10	Liquid penetration depth at different (a) ambient gas densities or temperatures, (b) injection pressures and (c) injection diameters. (d) Flame lift-off at different ambient temperatures.	75
4.11	2D contours plots of temperature in two planes parallel and perpendicular to the piston at the end of compression and before the fuel injection.	77
4.12	Iso-levels and contours of temperature with fuel droplets during the injection for case 1 described in Table 4.1.	77
4.13	Evaporated fuel mass fraction and temperature contours as predicted by the LES-FD and FMDF-MC for (a) case 1, (b) case 2, (c) case 3 and (d) case 4 described in Table 4.1. Predicted liquid penetration and flame lift-off are also indicated.	78
4.14	Scatter plots of LES-FD and FMDF-MC temperatures for case 4, (a) before reaction and (b) after reaction.	80
5.1	(a) Geometrical details of the sudden expansion configuration with fixed valve. There is no piston and the valve is fixed, (b) Two-dimensional and three-dimensional cross sectional view of the 5-block grid system employed for LES of the sudden-expansion plus valve flow configuration.	101
5.2	(a) Two-dimensional and (b) three-dimensional contour plots of vorticity.	101
5.3	(a) Mean axial velocity and (b) rms of axial velocity normalized with the inlet velocity. Solid lines and dashed lines show the LES results with dynamic and constant coefficient ($C_d = 0.1$) Smagorinsky, respectively. Symbols represent the experimental (LDA) data.	103
5.4	(a) Geometrical details of the simulated piston-cylinder assembly with fixed valve and moving piston (Moore et al.[23]),(b) Three-dimensional and two-dimensional view of the 4-block grid system employed for LES of flow in a simple piston-cylinder configuration with fixed valve and flat moving piston.	104
5.5	Instantaneous contours of the axial velocity normalized by the mean piston speed, (a) at crank angle of 24, (b) at crank angle of 48 (c) at crank angle of 108, (d) at crank angle of 180.	105

5.6	(a) Mean axial velocity and (b) rms of axial velocity, normalized by the mean piston speed, at crank angle of 36° and location of 10 mm from the cylinder head calculated by azimuthally averaging of the instantaneous filtered velocity for six subsequent cycles.	106
5.7	(a) Mean axial velocity and (b) rms of axial velocity, normalized by the mean piston speed, at crank angle of 36° . Solid lines and dashed lines are LES results obtained by the dynamic and constant coefficient ($C_d = 0.1$) Smagorinsky models, respectively, and symbols are LDA data.	107
5.8	(a) Mean axial velocity and (b) rms of axial velocity (b) normalized by the mean piston speed, at crank angle of 144° . Solid lines and dashed lines are LES results obtained by the dynamic and constant coefficient ($C_d = 0.1$) Smagorinsky models, respectively, and symbols are LDA data.	108
5.9	Schematic pictures of the MSUs 3-valve DISI engine.	109
5.10	Three-dimensional and two-dimensional cross sectional views of the 18-block grid system used for LES of MSUs 3-valve DISI engine. . . .	110
5.11	Volumetric averaged values of (a) temperature, (b) vorticity and (c) turbulent viscosity at different crank angles and cycles.	111
5.12	Comparison of in-cylinder flow statistics at different crank angles; (a) rms of the three velocity components and temperature, and (b) piston speed, turbulent viscosity, vorticity, velocity magnitude and rms of axial velocity.	113
5.13	(a) Nine different zones or sections inside the cylinder for calculating turbulent intensity, (b) turbulent intensity in 9 special filter at different crank angles.	114
5.14	(a) Temperature, (b) vorticity, and (c) kinetic energy of several fluid particles traveling in the cylinder during the intake stroke and beginning of compression stroke.	115
5.15	Three-dimensional contours of the pressure and several sample Lagrangian particles during the intake at crank angles of (a) 60° , (b) 90° and (c) 180°	117
5.16	Two-dimensional contours of the axial velocity during the intake at crank angles of (a) 60° , (b) 90° and (c) 180°	119

5.17	Scatter plots and iso-levels of temperatures as predicted by LES-FD and FMDF-MC during the flame propagation in the DISI engine at crank angle (a) 345° , (b) 355° and (c) 365°	121
5.18	Fuel droplets' pattern during the intake at crank angles of (a) 84° , (b) 100° and (c) 148°	124
5.19	Instantaneous contour plots of evaporated fuel mass fraction predicted by (a) LES-FD and (b) FMDF-MC, and temperature contour plots predicted by (c) LES-FD and (d) FMDF-FD, when the crank angle is 270°	125
5.20	Consistency of LES-FD and FMDF-MC for (a) evaporated fuel mass fraction and (b) temperature during the compression at crank angles of 250° , 290° and 330° along the three line connecting the exhaust (Ex), and two intake (In1,In2) valve to the piston.	126
5.21	Scatter plots and instantaneous contour plots of evaporated fuel mass fraction predicted by (a) LES-FD and (b) FMDF-MC, and temperature contour plots predicted by (c) LES-FD and (d) FMDF-FD, at the crank angle of 335° before ignition.	127
5.22	Scatter plots and iso-levels of temperatures as predicted by LES-FD and FMDF-MC during the flame propagation in the DISI engine at crank angle (a) 345° , (b) 355° and (c) 365°	128
5.23	Volume-averaged values of temperature, equivalence ratio and pressure as predicted by LES-FD and FMDF-MC.	131

Nomenclature

a	=	speed of sound, m/s
C_d	=	Smagorinsky model constant
C_m	=	MKEV model constant
C_ω	=	mixing model constant
C_μ, C_β, C_κ	=	artificial viscosity and conductivity model constants
e	=	internal energy, J/Kg
E	=	total internal energy, J/Kg
$\hat{F}, \hat{G}, \hat{H}$	=	inviscid fluxes
$\hat{F}_v, \hat{G}_v, \hat{H}_v$	=	viscous fluxes
G	=	filter function
H	=	total enthalpy, J/Kg
J	=	Jacobian of transformation
N_s	=	number of species
p	=	pressure, Pa
P_L	=	filtered mass density function, Kg
Pr_t	=	turbulent Prandtl number
\dot{Q}	=	heat release rate, J/Kg.s
R	=	mixture gas constant, J/Kg.K
$ \tilde{S} $	=	rate-of-strain magnitude, 1/s
S_o	=	source term
Sc	=	Schmidt number

t	=	time, s
T	=	temperature, K
T_{ref}	=	reference temperature, K
u, v, w	=	velocity components, m/s
u_{ref}	=	reference velocity, m/s
U	=	solution vector
\mathbf{x}	=	position vector, m
x_i	=	ith component of the position vector, m
X_i^+	=	probabilistic representations of position, m
W	=	Wiener process, s ^{1/2}
$w^{(n)}$	=	weight of a Monte Carlo particle
Γ, Γ_t	=	diffusion coefficient, turbulent diffusion coefficient, Kg/m.s
δ	=	Dirac delta function
Δ_G	=	filter size, m
$\kappa, \kappa_e, \kappa^*$	=	thermal, effective, artificial conductivity, J/m.s.K
μ, μ_e, μ^*	=	molecular, effective, artificial viscosity, Kg/m.s
ν_t	=	subgrid-scale turbulent kinematic viscosity, m ² /s
ξ, η, ζ, τ	=	independent variables in transformed domain
$\xi_t, \xi_x, \xi_y, \xi_z$	=	metric coefficients of the coordinate transformation
$\eta_t, \eta_x, \eta_y, \eta_z$		
$\zeta_t, \zeta_x, \zeta_y, \zeta_z$		
ρ	=	density, Kg/m ³
σ	=	fine-grained density
ϕ_α	=	compositional value of scalar α
ϕ_α^+	=	probabilistic representations of scalar α
Φ	=	composition vector

Ψ = composition sample space vector

Ω_m = mixing frequency, 1/s

$\dot{\omega}_\alpha$ = reaction rate of species α , 1/s

Subscript

i, j = variable number

α = scalar number

Conventions

$\langle \rangle_l$ or $-$ = filtered value

$\langle \rangle_L$ or \sim = Favre filtered value

$\langle | \rangle_L$ = conditional Favre filtered value

$\langle \rangle_{l'}$ = secondary filter function

$\langle \rangle$ = time-averaged value

Chapter 1

Introduction

The flow field in internal combustion (IC) engines is complicated combinations of boundary layers, shear layers, recirculating flows behind valves, highly unsteady in-cylinder turbulent motions, spray and combustion with substantial cycle-to-cycle variations (CCV). Accurate numerical simulation of such a complicated flow field requires robust turbulent, spray and combustion models and numerical methods capable of handling complex geometries, deforming mesh, liquid fuel droplet dispersion, evaporation and combustion. Most of numerical techniques used for the in-cylinder turbulent flow simulations have traditionally been based on the Reynolds-averaged Navier-Stokes (RANS) models. RANS models are not able to predict the CCV and highly unsteady three-dimensional fluid motions in IC engines. Since direct numerical simulation (DNS) of the flow in a realistic IC engine is not feasible, large-eddy simulation (LES) seems to be the best choice for numerical simulation of such flows. In this dissertation, a high-order compressible flow solver based on LES model is further developed for flows in complex geometries with moving boundaries. For simulating the combustion in IC engines, the filtered mass density function (FMDF) is extended for compressible flows by including the pressure effect in the FMDF transport equation. High-order Eulerian finite-difference (FD) and Lagrangian Monte Carlo (MC)

methods are used for the solution of LES and FMDF equations, respectively. The effect of liquid droplets in the LES and FMDF formulations are included for spray combustion problems. A new Lagrangian-Eulerian-Lagrangian numerical method is employed for the solution of LES/FMDF for turbulent spray combustion in complex geometries and moving boundaries.

This dissertation is organized as follows. In chapter 2, the mathematical formulation for the two-phase compressible LES/FMDF model and the numerical solution procedure for solving the LES/FMDF equations are presented. In chapter 3, the effect of compressibility on the FMDF is investigated by simulating three compressible subsonic and supersonic flows: (1) the flow in a rapid compression machine (RCM), (2) the flow in a shock tube and (3) a supersonic co-axial jet flow. In chapter 4, the fluid dynamics, the heat transfer, the spray and the combustion inside the RCM are studied. In the RCM simulations, two kinds of flat and crevice piston is used. In chapter 5, using the new two-phase LES/FMDF model, three reacting and non-reacting flows, all related to IC engines, are simulated: the steady flow through a poppet valve in a sudden expansion configuration, the flow inside a simple piston-cylinder assembly with a stationary open valve and harmonically moving flat piston and the flow in a three-valve direct-injection spark-ignition engine. Non-reacting turbulent flow simulations are conducted in the first two configurations and the predicted results are compared with the available experimental data. For the last configuration, non-reacting turbulent flow, single-phase combustion and spray combustion are simulated. For all simulated flows, the consistency and the accuracy of LES/FMDF is established whenever it is possible.

Chapter 2

Mathematical formulations and numerical solution

In this chapter, governing equations for the compressible two-phase LES/FMDF model together with the numerical solution procedure are presented.

2.1 Governing equations

The new two-phase LES/FMDF model is based on three interacting components: (1) the standard filtered LES equations, (2) the FMDF equations and its Lagrangian stochastic solver, (3) the Lagrangian spray equations. These equations are presented in the following sections.

2.1.1 Filtered LES equations

The Favre filtered [1] compressible mass, momentum, energy and scalar equations in curvilinear coordinate system may be written in the following compact form [2, 3, 4, 5]:

$$\frac{\partial(JU)}{\partial\tau} + \frac{(\partial\hat{F} - \hat{F}_v)}{\partial\xi} + \frac{(\partial\hat{G} - \hat{G}_v)}{\partial\eta} + \frac{(\partial\hat{H} - \hat{H}_v)}{\partial\zeta} = S_o J, \quad (2.1)$$

where $J = \frac{\partial(x,y,z,t)}{\partial(\xi,\eta,\zeta,\tau)}$ is the Jacobian of transformation and $U = (\bar{\rho}, \bar{\rho}\tilde{u}, \bar{\rho}\tilde{v}, \bar{\rho}\tilde{w}, \bar{\rho}\tilde{E}, \bar{\rho}\tilde{\phi})$ is the solution vector. The primary variables are the filtered density, $\bar{\rho}$, the velocity components, $\tilde{u}, \tilde{v}, \tilde{w}$, the total internal energy, $\tilde{E} = \tilde{e} + \frac{1}{2}\tilde{u}_i\tilde{u}_i$, and the scalar mass fraction, $\tilde{\phi}$. The inviscid fluxes in Eq. (2.1), \hat{F} , \hat{G} and \hat{H} are defined as:

$$\hat{F} = J \begin{bmatrix} \bar{\rho}\hat{U} \\ \bar{\rho}\tilde{u}\hat{U} + \bar{p}\hat{\xi}_x \\ \bar{\rho}\tilde{v}\hat{U} + \bar{p}\hat{\xi}_y \\ \bar{\rho}\tilde{w}\hat{U} + \bar{p}\hat{\xi}_z \\ (\bar{\rho}\tilde{E} + \bar{p})\hat{U} - \hat{\xi}_t \\ \bar{\rho}\tilde{\phi}\hat{U} \end{bmatrix}, \hat{G} = J \begin{bmatrix} \bar{\rho}\hat{V} \\ \bar{\rho}\tilde{u}\hat{V} + \bar{p}\hat{\eta}_x \\ \bar{\rho}\tilde{v}\hat{V} + \bar{p}\hat{\eta}_y \\ \bar{\rho}\tilde{w}\hat{V} + \bar{p}\hat{\eta}_z \\ (\bar{\rho}\tilde{E} + \bar{p})\hat{V} - \hat{\eta}_t \\ \bar{\rho}\tilde{\phi}\hat{V} \end{bmatrix}, \hat{H} = J \begin{bmatrix} \bar{\rho}\hat{W} \\ \bar{\rho}\tilde{u}\hat{W} + \bar{p}\hat{\zeta}_x \\ \bar{\rho}\tilde{v}\hat{W} + \bar{p}\hat{\zeta}_y \\ \bar{\rho}\tilde{w}\hat{W} + \bar{p}\hat{\zeta}_z \\ (\bar{\rho}\tilde{E} + \bar{p})\hat{W} - \hat{\zeta}_t \\ \bar{\rho}\tilde{\phi}\hat{W} \end{bmatrix},$$

$$\begin{aligned} \hat{U} &= \hat{\xi}_t + \hat{\xi}_x\tilde{u} + \hat{\xi}_y\tilde{v} + \hat{\xi}_z\tilde{w}, \\ \hat{V} &= \hat{\eta}_t + \hat{\eta}_x\tilde{u} + \hat{\eta}_y\tilde{v} + \hat{\eta}_z\tilde{w}, \\ \hat{W} &= \hat{\zeta}_t + \hat{\zeta}_x\tilde{u} + \hat{\zeta}_y\tilde{v} + \hat{\zeta}_z\tilde{w}, \end{aligned} \tag{2.2}$$

with $\hat{\xi}_x = J^{-1}\partial\xi/\partial x, \dots$, etc., being the metric coefficients [2]. Inviscid fluxes are calculated based on the relative velocity of flow and grids by adding the time derivative of metrics $\hat{\xi}_t$, $\hat{\eta}_t$ and $\hat{\zeta}_t$ to the \hat{U} , \hat{V} and \hat{W} . In Eqs. (2.1) and (2.2), \bar{p} is the filtered pressure and S_o represents the source term. \hat{F}_v , \hat{G}_v and \hat{H}_v are the viscous fluxes and defined in Ref. [4]. The subgrid stress terms are closed here by gradient-type closures. In these closure, an effective viscosity, $\mu_e = \mu + \bar{\rho}\nu_t$, is employed by combining the molecular viscosity, μ with the turbulent kinematic viscosity, ν_t . Turbulent viscosity is modeled by the Smagorinsky model [6, 7] or modified kinetic energy velocity (MKEV) closures. In the Smagorinsky closure, the turbulent kinematic viscosity is modeled

as:

$$\nu_t = (C_d \Delta)^2 |\tilde{S}|. \quad (2.3)$$

In Eq. (2.3), $|\tilde{S}|$ is the magnitude of the rate-of-strain tensor, $\Delta = (volume)^{1/3}$ represents the characteristic size of the filter function and C_d is the model constant which can be either fixed or obtained by the dynamic procedure [8, 9, 10]. In the MKEV closure, the turbulent kinematic viscosity is obtained by the following equation:

$$\nu_t = C_m \Delta_G \sqrt{|\tilde{u}_i^* \tilde{u}_i^* - \langle \tilde{u}_i^* \rangle_{l'} \langle \tilde{u}_i^* \rangle_{l'}|}, \quad (2.4)$$

where C_m is the model coefficient, $\tilde{u}_i^* = \tilde{u}_i - u_{ref}$, and l' denotes the secondary filter function. The SGS velocity correlations in the energy and scalar equations are also modeled with a gradient type closure,

$$\bar{\rho}(\widetilde{u_i E} - \tilde{u}_i \tilde{E}) + (\widetilde{p u_i} - \tilde{p} \tilde{u}_i) = -\bar{\rho} \frac{\nu_t}{Pr_t} \frac{\partial \tilde{H}}{\partial x_i}, \quad (2.5)$$

$$\bar{\rho}(\widetilde{u_i \phi} - \tilde{u}_i \tilde{\phi}) = -\bar{\rho} \frac{\nu_t}{Sc_t} \frac{\partial \tilde{\phi}}{\partial x_i}, \quad (2.6)$$

where $\tilde{H} = \tilde{E} + \frac{\tilde{p}}{\bar{\rho}}$, is the total filtered enthalpy and Pr_t and Sc_t are the turbulent Prandtl and Schmidt numbers, respectively. The convection of the SGS kinetic energy by the SGS velocity is assumed to be negligible.

The first term on the left hand side of Eq. (2.1), the temporal term, is decomposed into two terms using the chain rule as:

$$\frac{\partial(JU)}{\partial \tau} = J \frac{\partial U}{\partial \tau} + U \frac{\partial J}{\partial \tau}. \quad (2.7)$$

The time derivative of Jacobian is zero in a fixed grid system. In a moving grid system is not zero and is calculated based on the geometric conservation law (GCL) [2, 11]:

$$\frac{\partial J}{\partial \tau} = -[(\hat{\xi}_t)_\xi + (\hat{\eta}_t)_\eta + (\hat{\zeta}_t)_\zeta], \quad (2.8)$$

where

$$\begin{aligned} \hat{\xi}_t &= -[x_x(\hat{\xi}_x) + y_x(\hat{\xi}_y) + z_x(\hat{\xi}_z)], \\ \hat{\eta}_t &= -[x_x(\hat{\eta}_x) + y_x(\hat{\eta}_y) + z_x(\hat{\eta}_z)], \\ \hat{\zeta}_t &= -[x_x(\hat{\zeta}_x) + y_x(\hat{\zeta}_y) + z_x(\hat{\zeta}_z)]. \end{aligned}$$

The vector (x_x, y_y, z_z) is the grid speed vector which is calculated numericly here based on the piston and intake/exhaust valve speeds.

The discretization procedure of the carrier fluid is based on the fourth order compact finite difference scheme [12]. The "spectral nature" of compact differencing makes it suitable for LES. However, compact schemes cause significant numerical oscillations when there are discontinuities like shock waves in the flow. Cook and Cabot [13, 14, 15] introduced high-wavenumber artificial viscosity to damp the numerical oscillations of the compact scheme. Fiorina and Lele [16] and Kawai and Lele [17] extended the artificial viscosity method to curvilinear grids. In the Cook [15] and Kawai et al. [17] method, the total stress tensor is written as:

$$\tau_{ij} = (\mu_e + C_\mu \mu^*)(2\tilde{S}_{ij}) - \left(C_\beta \mu^* - \frac{2}{3}(\mu_e + C_\mu \mu^*) \right) (\tilde{S}_{kk} \delta_{ij}), \quad (2.9)$$

where

$$\mu^* = \bar{\rho} \left| \sum_{l=3}^3 \left(\sum_{m=3}^3 \left(\frac{\partial^r \xi_l}{\partial x_m^r} \right)^2 \right)^{r/2} \frac{\partial^r \tilde{S}}{\partial \xi_l^r} \Delta_l^{r+2} \right|. \quad (2.10)$$

Furthermore, the conductivity coefficient in the total internal energy equation is modified as $\kappa_e = \kappa + \kappa^*$, where κ is the fluid conductivity and κ^* the artificial conductivity defined as:

$$\kappa^* = C_\kappa \frac{\bar{\rho} \tilde{a}}{\tilde{T}} \left| \sum_{l=3}^3 \left(\sum_{m=3}^3 \left(\frac{\partial^r \xi_l}{\partial x_m^r} \right)^2 \right)^{r/2} \frac{\partial^r \tilde{e}}{\partial \xi_l^r} \Delta_l^{r+1} \right|. \quad (2.11)$$

In the above equations, $C_\mu = 0.002$, $C_\beta = 1$ and $C_\kappa = 0.01$ are model constants, $r = 4$ is the order of derivatives, and $\Delta_l^2 = \sum_{n=1}^3 \left(\frac{x_{n,i+1} - x_{n,i-1}}{2} \right)^2$ is the grid spacing in the ξ_l direction [17]. Note that, ξ_1 , ξ_2 and ξ_3 are equivalent to ξ , η and ζ , respectively.

2.1.2 Compressible two-phase FMDF

The scalar FMDF, considered here, represents the joint PDF of the scalar vector at the subgrid-level and is defined as:

$$P_L(\Psi; \mathbf{x}, \mathbf{t}) = \int_{-\infty}^{+\infty} \rho(\mathbf{x}', \mathbf{t}) \sigma[\Psi, \Phi(\mathbf{x}', \mathbf{t})] \mathbf{G}(\mathbf{x}' - \mathbf{x}) d\mathbf{x}', \quad (2.12)$$

$$\sigma[\Psi, \Phi(\mathbf{x}', \mathbf{t})] = \Pi_{\alpha=1}^{N_s+1} \delta(\psi_\alpha - \phi_\alpha(\mathbf{x}, \mathbf{t})), \quad (2.13)$$

where G denotes the filter function, Ψ is the scalar vector in the sample space and σ is the "fine-grained" density [18], defined based on a series of delta functions, δ . The scalar vector, $\Phi \equiv \phi_\alpha$, ($\alpha = 1, \dots, N_s + 1$), includes the species mass fractions and the specific enthalpy ($\phi_{\alpha \equiv N_s+1}$). The transport equation for the FMDF may be derived from the following unfiltered equation for the scalar vector:

$$\rho \frac{\partial \phi_\alpha}{\partial t} + \rho u_i \frac{\partial \phi_\alpha}{\partial x_i} = \frac{\partial}{\partial x_i} \left(\Gamma \frac{\partial \phi_\alpha}{\partial x_i} \right) + \rho S_\alpha^R + S_\alpha^{cmp} + S_\alpha^{spy} - \phi_\alpha S_m. \quad (2.14)$$

Here, for simplicity, we consider the scalar equation in the Cartesian coordinate system. In Eq. (2.14), for the species mass fraction equation ($\alpha = 1, \dots, N_s$), the source

term $S_\alpha^R = \dot{w}_\alpha$ represent the production or consumption of species α due to reaction and $S_\alpha^{spy} = S_m$ is the production of species α due to droplet evaporation. For the energy or enthalpy equation ($\alpha = N_s + 1$) the source term $S_\alpha^R = \dot{Q}$ is the heat of combustion, $S_\alpha^{cmp} = \frac{1}{\rho}(\frac{\partial p}{\partial t} + u_i \frac{\partial p}{\partial x_i} + \tau_{ij} \frac{\partial u_j}{\partial x_i})$ is due to compressibility effect and $S_\alpha^{spy} = S_h$ is due to phase change or droplet evaporation. To derive the FMDF equation, one may start from the the time-derivative of FMDF (Eq. (2.12)):

$$\frac{\partial P_L(\Psi; x, t)}{\partial t} = -\frac{\partial}{\partial \psi_\alpha} \left[\left\langle \frac{\partial \phi_\alpha}{\partial t} | \Psi \right\rangle_l P_L(\Psi; x, t) \right], \quad (2.15)$$

where $\langle f | \Psi \rangle_l$ denotes the conditional filtered value of function "f". The FMDF transport equation is derived by inserting Eq. (2.14) into Eq. (2.15):

$$\begin{aligned} \frac{\partial P_L}{\partial t} &+ \frac{\partial [\langle u_i | \Psi \rangle_l P_L]}{\partial x_i} \\ &- \left\langle \left(\frac{1}{\rho} \left[\frac{\partial \rho}{\partial t} + \frac{\partial (\rho u_i)}{\partial x_i} \right] \right) | \Psi \right\rangle_l P_L \\ &= \frac{\partial}{\partial \psi_\alpha} \left[\left\langle - \left(\frac{1}{\rho} \frac{\partial}{\partial x_i} \Gamma \frac{\partial \phi_\alpha}{\partial x_i} \right) | \Psi \right\rangle_l P_L \right] \\ &- \frac{\partial}{\partial \psi_\alpha} \left[\left\langle S_\alpha^R | \Psi \right\rangle_l P_L \right] - \frac{\partial}{\partial \psi_\alpha} \left[\left\langle S_\alpha^{cmp} | \Psi \right\rangle_l P_L \right] \\ &- \frac{\partial}{\partial \psi_\alpha} \left[\left\langle \frac{S_\alpha^{spy}}{\rho} | \Psi \right\rangle_l P_L - \left\langle \frac{\psi_\alpha S_m}{\rho} | \Psi \right\rangle_l P_L \right]. \end{aligned} \quad (2.16)$$

In Eq. (2.16), the source/sink terms are different for species and energy, and are defined as:

$$\begin{cases} S_\alpha^R = \dot{w}_\alpha & , & S_\alpha^{cmp} = 0 & , & S_\alpha^{spy} = S_m & \alpha \equiv 1, \dots, N_s \\ S_\alpha^R = \dot{Q} & , & S_\alpha^{cmp} = \frac{1}{\rho}(\frac{\partial p}{\partial t} + u_i \frac{\partial p}{\partial x_i} + \tau_{ij} \frac{\partial u_j}{\partial x_i}) & , & S_\alpha^{spy} = S_e & \alpha \equiv N_{s+1} \end{cases} \quad (2.17)$$

Equation (2.16) is an exact transport equation for the scalar FMDF. In this equation molecular Prandtl and Schmidt number are the same, so the mass/thermal diffusion coefficients be $\Gamma = \mu/Sc$. The second term on the right-hand side (RHS) of Eq. (2.16)

is the chemical reaction term and is closed when the effect of SGS pressure fluctuations are ignored and $\langle S_\alpha^R | \Psi \rangle_l = S_\alpha^R(\psi)$. This term is not closed in the filtered scalar equation and "conventional" LES methods. However, the FMDF equation cannot be solved directly due to presence of three unclosed terms. The first one is the convection term (the second term on the LHS of Eq. (2.16)) which can be decomposed into large-scale convection by the filtered velocity and the SGS convection as [19]:

$$\langle u_i | \Psi \rangle_l P_L = \langle u_i \rangle_L P_L + (\langle u_i | \Psi \rangle_l P_L - \langle u_i \rangle_L P_L), \quad (2.18)$$

the SGS convection is modeled here with a gradient type closure:

$$(\langle u_i | \Psi \rangle_l P_L - \langle u_i \rangle_L P_L) = \Gamma_t \frac{\partial (P_L / \langle \rho \rangle_l)}{\partial x_i}, \quad (2.19)$$

where $\Gamma_t = \langle \rho \rangle_l \nu_t / Pr_t$ is the turbulent diffusivity and Pr_t is the turbulent Prandtl number. Here, we use the notation $\langle \rangle_L$ and $\langle \rangle_l$ for the Favre filtered and filtered values, respectively.

The second unclosed term in the FMDF transport equation (the first term on the RHS of Eq. (2.16)) is also decomposed into two parts: the molecular transport and the SGS dissipation. The SGS dissipation is modeled with the linear mean-square estimation (LMSE) [20, 21] or the interaction by exchange with the mean (IEM) model [22]:

$$\frac{\partial}{\partial \psi_\alpha} \left[\left\langle - \left(\frac{1}{\rho} \frac{\partial}{\partial x_i} \left(\Gamma \frac{\partial \phi_\alpha}{\partial x_i} \right) \right) | \Psi \right\rangle_l P_L \right] = \frac{\partial}{\partial x_i} \left[\Gamma \frac{\partial (P_L / \langle \rho \rangle_l)}{\partial x_i} \right] + \frac{\partial}{\partial \psi_\alpha} [\Omega_m (\psi_\alpha - \langle \phi_\alpha \rangle_L) P_L], \quad (2.20)$$

where the SGS mixing frequency, $\Omega_m = C_\omega (\Gamma + \Gamma_t) / (\Delta_G \langle \rho \rangle_l)$ is obtained from the molecular and SGS turbulent diffusivities (Γ and Γ_t) and the filter size (Δ_G).

To extend the Reynolds-averaged Navier-Stokes (RANS) PDF method to compressible flows, Delarue and Pope [23] considered the pressure as one of the random

variables in the PDF formulation and solved a set of modeled stochastic equations for the joint velocity-frequency-energy-pressure PDF. In the scalar FMDF model considered in this study, the pressure is not directly included in the FMDF formulation, and only the effect of filtered pressure on the scalar FMDF is considered. The last term on the RHS of Eq. (2.16) represents the effect of pressure and viscosity on the scalar. The part due to temporal derivative of pressure is written here as:

$$\left\langle \left(\frac{1}{\rho} \frac{\partial p}{\partial t} \right) | \Psi \right\rangle_l P_L = \frac{1}{\langle \rho \rangle_l} \left(\frac{\partial \langle p \rangle_l}{\partial t} \right) P_L \quad \alpha \equiv N_{s+1}. \quad (2.21)$$

The spatial derivative part is decomposed further into the resolved and SGS parts:

$$\begin{aligned} \left\langle \left(\frac{1}{\rho} u_i \frac{\partial p}{\partial x_i} \right) | \Psi \right\rangle_l P_L &= \frac{1}{\langle \rho \rangle_l} \langle u_i \rangle_L \frac{\partial \langle p \rangle_l}{\partial x_i} P_L \\ &+ \left(\left\langle \left(\frac{1}{\rho} u_i \frac{\partial p}{\partial x_i} \right) | \Psi \right\rangle_l P_L - \frac{1}{\langle \rho \rangle_l} \langle u_i \rangle_L \frac{\partial \langle p \rangle_l}{\partial x_i} P_L \right) \quad \alpha \equiv N_{s+1}. \end{aligned} \quad (2.22)$$

Similarly, the viscous dissipation part is decomposed into the resolved and SGS parts as:

$$\begin{aligned} \left\langle \left(\frac{1}{\rho} \tau_{ij} \frac{\partial u_i}{\partial x_j} \right) | \Psi \right\rangle_l P_L &= \frac{1}{\langle \rho \rangle_l} \langle \tau_{ij} \rangle_L \frac{\partial \langle u_i \rangle_L}{\partial x_j} P_L \\ &+ \left(\left\langle \left(\frac{1}{\rho} \tau_{ij} \frac{\partial u_i}{\partial x_j} \right) | \Psi \right\rangle_l P_L - \frac{1}{\langle \rho \rangle_l} \langle \tau_{ij} \rangle_L \frac{\partial \langle u_i \rangle_L}{\partial x_j} P_L \right) \quad \alpha \equiv N_{s+1}. \end{aligned} \quad (2.23)$$

Here, we ignore the SGS viscous term in Eq. (2.23) and the SGS pressure term in Eq. (2.22).

There are three terms in the FMDF equation (Eq. (2.16)) due to spray/droplet; the third term on the LHS due to the mass addition and the last two terms on the RHS due to droplet-gas interactions. Here, these terms are approximated as:

$$\begin{aligned}
-\frac{\partial}{\partial \psi_\alpha} \left[\left\langle \frac{S_\alpha^{spy}}{\rho} | \Psi \right\rangle_l P_L - \left\langle \frac{\psi_\alpha S_m}{\rho} | \Psi \right\rangle_l P_L \right] + \frac{\langle S_m | \psi \rangle_l P_L}{\langle \rho \rangle_l} = \\
= -\frac{\partial}{\partial \psi_\alpha} \left[\frac{\langle S_\alpha^{spy} \rangle_l P_L}{\langle \rho \rangle_l} - \frac{\psi_\alpha \langle S_m \rangle_l P_L}{\langle \rho \rangle_l} \right] \\
+ \frac{\langle S_m \rangle_l P_L}{\langle \rho \rangle_l}. \quad (2.24)
\end{aligned}$$

By inserting Eqs. (2.18)-(2.24) into Eq. (2.16), the final form of the FMDF transport equation for a two-phase compressible reacting system becomes:

$$\begin{aligned}
\frac{\partial P_L}{\partial t} + \frac{\partial [\langle u_i \rangle_L P_L]}{\partial x_i} = & \frac{\partial}{\partial x_i} \left[(\Gamma + \Gamma_t) \frac{\partial (P_L / \langle \rho \rangle_l)}{\partial x_i} \right] \\
& + \frac{\partial}{\partial \psi_\alpha} [\Omega_m (\psi_\alpha - \langle \phi_\alpha \rangle_L) P_L] \\
& - \frac{\partial}{\partial \psi_\alpha} [S_\alpha^R(\psi) P_L] - \frac{\partial}{\partial \psi_\alpha} [\tilde{S}_\alpha^{cmp} P_L] \\
& - \frac{\partial}{\partial \psi_\alpha} \left[\frac{\langle S_\alpha^{spy} \rangle_l P_L}{\langle \rho \rangle_l} - \frac{\psi_\alpha \langle S_m \rangle_l P_L}{\langle \rho \rangle_l} \right] + \frac{\langle S_m \rangle_l P_L}{\langle \rho \rangle_l}, \quad (2.25)
\end{aligned}$$

where

$$\begin{cases} S_\alpha^R = \dot{\omega}_\alpha & , \quad \tilde{S}_\alpha^{cmp} = 0 & , \quad \langle S_\alpha^{spy} \rangle = \langle S_m \rangle \\ S_\alpha^R = \dot{Q} & , \quad \tilde{S}_\alpha^{cmp} = \frac{1}{\langle \rho \rangle_l} \left(\frac{\partial \langle p \rangle_l}{\partial t} + \langle u_i \rangle_L \frac{\partial \langle p \rangle_l}{\partial x_i} + \langle \tau_{ij} \rangle_L \frac{\partial \langle u_i \rangle_L}{\partial x_j} \right) & , \quad \langle S_\alpha^{spy} \rangle = \langle S_h \rangle \end{cases}$$

for

$$\begin{cases} \alpha \equiv 1, \dots, N_s \\ \alpha \equiv N_{s+1} \end{cases}.$$

In Eq. (2.25), Ω_m denote the SGS mixing frequency, modeled as $\Omega_m = C_\omega(\Gamma + \Gamma_t)/(\Delta_G \langle \rho \rangle_l)$. Note that, by setting the $\tilde{S}_\alpha^{cmp} = 0$, $S_m = 0$ and $S_h = 0$, Eq. (2.25) will be the scalar FMDF transport equation for single-phase, constant pressure

reacting flows in Ref. [19].

2.1.3 Lagrangian fuel droplets

As mentioned before, the spray (droplet) field is simulated here with a Lagrangian model. In this model, the evolution of the droplet displacement vector, velocity vector, temperature, and mass is based on a set of non-equilibrium Lagrangian equations [26, 24, 25]:

$$\frac{dX_i}{dt} = V_i, \quad (2.26)$$

$$\frac{dV_i}{dt} = \frac{F_i}{m_d} = \frac{f_1}{\tau_d}(\tilde{u}_i - V_i), \quad (2.27)$$

$$\frac{dT_d}{dt} = \frac{Q_d + \dot{m}_d L_v}{m_d C_L} = \frac{Nu}{3Pr} \frac{C_{p,G}}{C_L} \frac{f_2}{\tau_d} (T_G - T_d) + \frac{\dot{m}_d}{m_d} \frac{L_v}{C_L}, \quad (2.28)$$

$$\frac{dm_d}{dt} = \dot{m} = -\frac{Sh}{3Sc_G} \frac{m_d}{\tau_d} \ln(1 + B_M), \quad (2.29)$$

$\tau_d = \rho_L D^2 / (18\mu_G)$ is the particle time constant, D is the droplet diameter, C_L is the heat capacity of liquids, $L_v = h_v^0 - (C_L - C_{p,V})T_d$ is the latent head of evaporation and h_v^0 and $C_{p,V}$ are the enthalpy of formation and specific heat of the evaporated fuel vapor at constant pressure, respectively. Drag of droplets is empirically corrected by the f_1 correlation function and f_2 is an analytical evaporative heat transfer correction function. The Nusselt, Sherwood, Prandtl, Schmidt numbers and temperature of the carrier gas are respectively denoted by Nu , Sh , Pr , Sc_G and T_G . Finally, B_M is the mass transfer number, calculated using the non-equilibrium surface vapor function [26]. Equations (2.26)-(2.29) yield the position, X_i , velocity, V_i , temperature, T_d and mass, m_d of a single droplet at different times.

The effects of droplets on the carrier gas mass, momentum, energy and species mass fractions are expressed with several source/sink terms included in Eq. (2.1) through vector $S_o = (S_m, S_{u1}, S_{u2}, S_{u3}, S_e, S_m)$. These terms model the two-way

coupling between the Lagrangian droplets and the Eulerian field. The mass source term, S_m represents the mass contribution of droplets due to evaporation. The momentum source term, S_{u_i} represents the momentum transfer between two phases due to drag force. The heat source term, S_e represents the exchange of the internal and kinetic energy by the convective heat transfer and particle drag. The droplet source/sink terms are evaluated by volumetric averaging and interpolation of the Lagrangian droplet variables with geometrical weighting of w_α within a computational cell with volume δV as:

$$S_m = - \sum_{\alpha \in \delta V} \left(\frac{w_\alpha}{\delta V} [\dot{m}_d]_\alpha \right), \quad (2.30)$$

$$S_{u_i} = - \sum_{\alpha \in \delta V} \left(\frac{w_\alpha}{\delta V} [F_i + \dot{m}_d V_i]_\alpha \right), \quad (2.31)$$

$$S_e = - \sum_{\alpha \in \delta V} \left(\frac{w_\alpha}{\delta V} [V_i F_i + Q_d + \dot{m}_d (\frac{V_i V_i}{2} + h_{v,s})]_\alpha \right). \quad (2.32)$$

In Eq. (2.32), $h_{v,s} = h_v^0 + C_{p,V} T_d$ is the evaporated vapor enthalpy at droplet surface. The source term defined in Eq. (2.32) is for the total internal energy equation (Eq. 2.1)). The source term for the enthalpy equation is:

$$S_h = S_e - V_i S_{u_i} + \frac{V_i V_i}{2} S_m. \quad (2.33)$$

2.2 Numerical solution procedure

In the modeled scalar FMDF equation (Eq. (2.25)), the carrier-gas velocity and pressure fields and spray source terms are not known and should be obtained by other means. Here in the hybrid LES/FMDF method, the filtered velocity and pressure are obtained by solving Eq. (2.1) with the "conventional" finite difference (FD) methods. Also, Lagrangian fuel droplet equations have to be solved with the filtered velocity and temperature from the FD solution. Spray source terms are obtained over the FD

grid points by local interpolation and averaging. With the known velocity and pressure fields and spray terms, the modeled FMDF equation can be solved by the well developed Lagrangian Monte Carlo (MC) procedure [27]. In this procedure, each MC particle undergoes motion in physical space due to filtered velocity and molecular and subgrid diffusivities. Effectively, the particle motion represents the spatial transport of the FMDF and is modeled by the following stochastic differential equation (SDE) [28]:

$$dX_i^+ = \left[\langle U_i \rangle_L + \frac{1}{\langle \rho \rangle_l} \frac{\partial(\Gamma + \Gamma_t)}{\partial x_i} \right] dt + \left[\sqrt{\frac{2(\Gamma + \Gamma_t)}{\langle \rho \rangle_l}} \right] dW_i(t), \quad (2.34)$$

where W_i denotes the Wiener process [29]. The compositional value of each particle is changed due to mixing, reaction, viscous dissipation and pressure variations in time and space. The change in composition is described by the following SDEs:

$$\begin{aligned} d\phi_\alpha^+ = & - \Omega_m(\phi_\alpha^+ - \langle \phi_\alpha \rangle_L) dt \\ & + [S_\alpha^R(\phi^+) + \tilde{S}_\alpha^{cmp} + \frac{\langle S_\alpha^{spy} \rangle_l}{\langle \rho \rangle_l} - \frac{\phi_\alpha^+ \langle S_m \rangle_l}{\langle \rho \rangle_l}] dt \quad \alpha \equiv 1, \dots, N_{s+1}. \end{aligned} \quad (2.35)$$

When combined, the diffusion processes described by Eqs. (2.34) and (2.35) have a corresponding Fokker-Planck equation which is identical to the FMDF transport equation (Eq. (2.25)). During the computation, to avoid expensive direct interaction between MC particles and spray droplets, spray terms in the FMDF equation are weighted averaged from FD grid points to the MC particle locations.

To manage the number of MC particles and the to reduce computational cost, a procedure involving the use of nonuniform weights is also considered. This procedure allows a smaller number of particles in regions where a low degree of variability is expected. Conversely, in regions of high variability, a larger number of particles is allowed. The variable weighting for particles allow the particle number density to stay above certain minimum number [27]. To calculate the Favre-filtered values of

any variable at a given point, MC particles are weighted averaged over a box of size Δ_E centered at the point of interest [19]. It has been shown [19, 27] that the sum of weights within the ensemble averaging domain, Δ_E , is related to the filtered fluid density as:

$$\langle \rho \rangle_l \approx \frac{\Delta m}{V_E} \sum_{n \in \Delta_E} w^{(n)}, \quad (2.36)$$

where V_E is the volume of the domain and Δm is the mass of a MC particle with a unit weight. For spray simulation, particle weights should be modified due to added mass to the carrier gas by droplet evaporation. In this case, the particle weight should be changed as $w^{(n)} = w^{(n)} + \frac{V_E}{\Delta m} \langle S_m \rangle_l dt$. The Favre-filtered value of any function of scalars like $Q(\phi)$ is obtained from the following weighted averaging operation:

$$\langle Q \rangle_L \approx \frac{\sum_{n \in \Delta_E} w^{(n)} Q(\phi)}{\sum_{n \in \Delta_E} w^{(n)}}. \quad (2.37)$$

Using Eq. (2.37), one can calculate the fluid density from the MC particles as:

$$\langle \rho \rangle_l \approx \left(\frac{\sum_{n \in \Delta_E} w^{(n)} (RT^{(n)} / \langle p \rangle_l)}{\sum_{n \in \Delta_E} w^{(n)}} \right)^{-1}. \quad (2.38)$$

The calculated filtered density from the MC particles should be the same as the filtered fluid density obtained from Eq. (2.1), and the weighted particle number density calculated by Eq. (2.36).

To include the compressibility in the FMDF formulation, the total derivative of filtered pressure, as computed by the filtered Eulerian carrier-gas equations are interpolated and added to the corresponding MC particles. Artificial viscosity causes the primitive variables to become smooth across the discontinuities. However, the computed derivatives of these variables may still be noisy, causing the FMDF values to become inaccurate and unphysical. To solve this problem, a flux limiter scheme

may be used. The main idea behind the flux limiter schemes is to limit the spatial derivatives of flow variables to realizable values. Here, van Leer's one-parameter family of the minmod limiters [30] is used for the calculation of spatial derivative of the filtered pressure:

$$\frac{\partial \bar{p}}{\partial x_i} = \text{minmod} \left(\theta \frac{\bar{p}_i - \bar{p}_{i-1}}{\Delta x}, \frac{\bar{p}_{i+1} - \bar{p}_{i-1}}{2\Delta x}, \theta \frac{\bar{p}_{i+1} - \bar{p}_i}{\Delta x} \right), \quad (2.39)$$

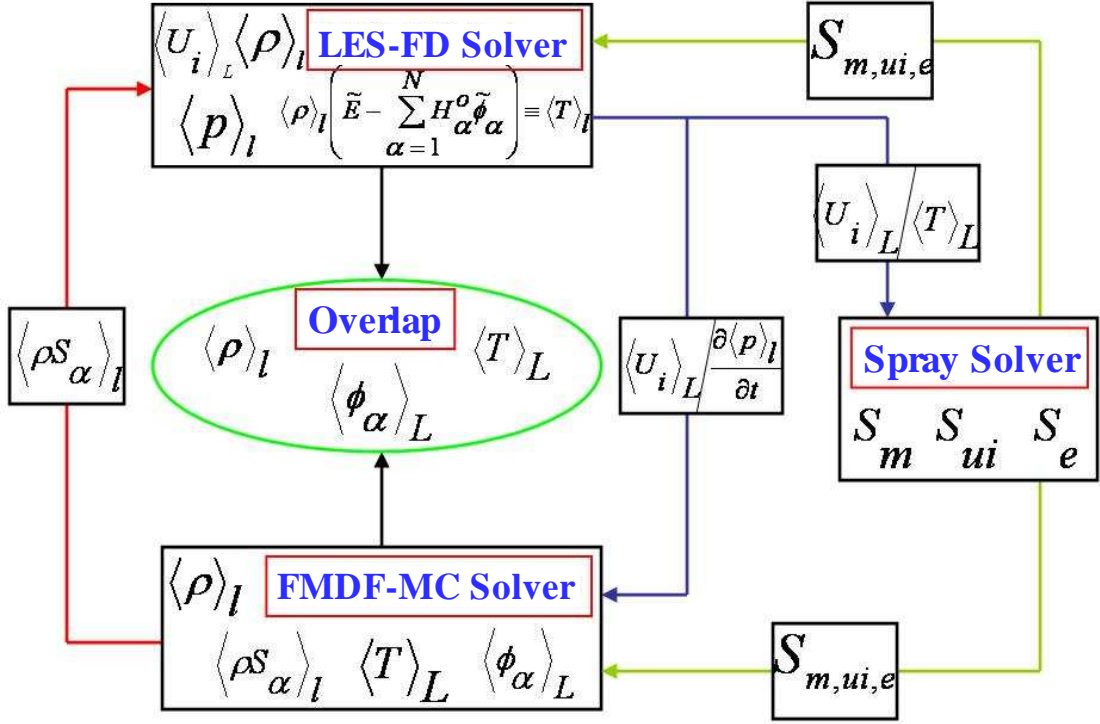
where $\theta \in [1, 2]$ and the multivariable minmod function is defined as:

$$\text{minmod}(a_1, a_2, \dots) = \begin{cases} \min_j[a_j] & \text{if } a_j > 0 \quad \forall j \\ \max_j[a_j] & \text{if } a_j < 0 \quad \forall j \\ 0 & \text{otherwise} \end{cases}.$$

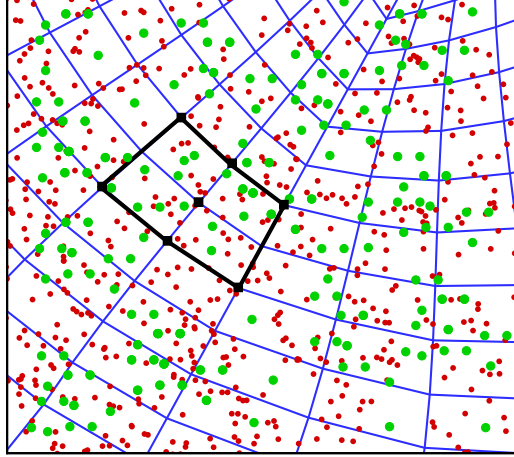
In the original version of this limiter [30], the minmod value of derivatives are calculated with a second order central, a first order forward and a first order backward differencing. In this work, instead of a second order central differencing scheme, the fourth order compact differencing is employed. In addition to the pressure, the spatial derivatives of turbulent diffusion coefficient Γ_t , as required in Eq. (2.34), are calculated by the Van-Leer limiter to avoid unphysical particle movements across the shock.

Figure 2.1(a) shows some of the main features of our hybrid two-phase compressible scalar LES/FMDF methodology. For the solution of filtered Eulerian carrier gas equations (Eq. (2.1)) any conventional numerical method may be used. The discretization procedure for this equation in this work is based on the fourth order compact FD scheme [12] and the third order low storage Runge-Kutta method. The FD equations are solved with "standard" closures for the SGS stress and scalar flux terms. For moving boundary case, at the beginning of every time step, grids are moved to their new locations (using new piston/valve locations as inputs), and

then, grids speed vector, Jacobian and the metrics values are calculated based on the new grid locations. Computations for multi-block grids are performed on parallel machines using MPI method. Lagrangian spray equations are solved via numerical methods similar to that used for the FMDF [31] and coupling terms are then calculated by volumetric averaging of their values in each cell and interpolated to the FD grid points. The SDEs are solved with the MC procedure. The filtered velocity and the derivatives of filtered pressure and velocity are computed over the FD grid points and then interpolated from the FD grid points to the MC particle locations. As it was mentioned before, the spray coupling terms in the FMDF equation are calculated by averaging over droplets and by feeding the FD data to the MC particles. Figure 2.1(b) shows a segment of FD grid networks, some of the MC particles and spray droplets and a sample ensemble domain used for particle averaging. In the present hybrid methodology, the filtered values of variables like temperature may be calculated from both LES-FD and FMDF-MC parts. This provides a unique opportunity for the assessment of FD and MC methods. Consistency of MC and FD data implies numerical accuracy of both methods. Mathematically, LES-FD and FMDF-MC results are identical. For establishing consistency of FD and MC methods in reacting flows, the chemical source term, which is closed in the FMDF-MC formulation is calculated from MC particles and used in the FD equations when needed. This is only possible in the hybrid LES/FMDF method.



(a)



(b)

Figure 2.1: For interpretation of the references to color in this and all other figures, the reader is referred to the electronic version of this dissertation. (a) Elements of hybrid two-phase LES/FMDF methodology. (b) A two-dimensional view of a portion of the LES/FMDF computational domain; solid black thick lines show a sample ensemble domain, FD cells are specified by the blue lines, the solid smaller circles are sample MC particles, and the solid larger circles are sample liquid droplets.

Chapter 3

Compressible Scalar FMDF for LES of High speed Turbulent Flows

3.1 Introduction

The performance of combustors in air-breathing propulsion systems is dependent on the complicated and often coupled effects of various factors such as the input/output operating flow conditions, the geometry, the fuel spray and the fuel chemistry. Normally, it is very difficult to predict the flow field in the combustors for various operating conditions and it is extremely costly and time consuming to develop and test a new or an improved combustion/propulsion system solely by experiment. On the other hand, high fidelity computational models, such as those developed based on the large-eddy simulation (LES) concept, are relatively inexpensive and can provide detailed time-dependent spatial data. Despite their great potentials, LES models have some limitations and are not fully accurate for several reasons [32, 33, 34, 35, 36]. The main reason is that the subgrid-scale (SGS) correlations have to be modeled explicitly or implicitly, since the simulating flows have resolutions larger than the smallest turbulent scales. The modeling of SGS correlations is significantly more difficult in

turbulent reacting flows particularly when the flow is compressible. This is not just due to the additional non-linearity of chemical source or sink terms, but also due to the intricate complexities of turbulence-reaction interactions [37], and the presence of shock/detonation waves at small scales. Several books and reviews are available for the various SGS closures currently in use [32, 33, 34, 35, 38, 39, 40, 41, 42, 43].

Some of the most promising models for LES of turbulent reacting flows are those developed based on the solution of the SGS probability density function (PDF) [18, 19, 44, 45, 46, 42, 43]. In this approach, the joint statistics of turbulent variables at subgrid level are obtained by solving the transport equation for the single-point joint SGS PDFs of these variables. The PDF equations are directly derived from the original instantaneous, unfiltered (DNS) equations. All terms involving single-point statistics appear in a closed form in the PDF equation, regardless of how complicated and nonlinear they are. This is one of the main advantages of the PDF method. The other advantage is that higher order statistical information are naturally included in the model. However, the single-point PDF equations are not completely closed, and some form of modeling for multi-point correlations are needed.

Jaberi et al. [19] developed a PDF model for LES based on the scalar filtered mass density function (FMDF), which is essentially the mass weighted filtered value of the fine-grained densities of energy and species mass fractions. In the scalar FMDF transport equation, all chemical source or sink terms are closed, making the FMDF very attractive for turbulent combustion simulations. However, the SGS convection and mixing terms in the scalar FMDF formulation needs to be modeled. Gicquel et al. [47] developed the velocity filtered density function in which the SGS convection is in a closed form. This approach was further extended to velocity-scalar [48, 49, 50, 51] and frequency-velocity-scalar FMDF [52]. The FMDF model has been used with a variety of reaction models. For example, Yaldizli et al. [53] employed the scalar FMDF for partially-premixed methane jet flames with the flamelet and

finite-rate methane-air kinetics models. A novel irregular Monte Carlo portioning procedure that facilitates efficient implementation of kinetics in the FMDF simulations is developed by Yilmaz et al. [54] and is used for a methane flame. Several applications of the FMDF model to practical problems have also been reported. Afshari et al. [4] used the scalar FMDF to simulate a premixed propane-air flame in an axisymmetric dump combustor. More recently, the scalar FMDF model is extended to multiphase combustion in realistic configurations. The new multiphase LES/FMDF methodology is implemented through an efficient Lagrangian-Eulerian-Lagrangian mathematical/computational methodology [55, 56, 31, 57], and has been applied to complex flows such as those involved in a direct-injection spark-ignition engine [57].

In the previous applications of the LES/FMDF, the effect of pressure on the scalar FMDF or the velocity-scalar FMDF was not considered. This effect could be ignored at low Mach numbers or constant pressure flows and combustion. However, it should be included in the LES/FMDF for high speed subsonic or supersonic flows. In this work, the scalar FMDF is extended to compressible flows. This is accomplished by adding a source term, obtained from the filtered velocity and pressure fields, to the FMDF equation. Three different subsonic and supersonic flows are simulated with the new compressible scalar FMDF model and its efficient numerical method. The first simulated flow involves the compression of a gas in a simple piston-cylinder assembly, called the rapid compression machine (RCM). The second flow is that in a three-dimensional (3D) shock tube, and the third flow is a co-axial helium-air jet. For the last flow, the velocity and scalar fields, as computed by the LES/FMDF with different SGS stress models, are compared with the experiment. The results below show that the pressure variations and compressibility effects are important in all these flows. They also show that the new compressible scalar FMDF model is able to capture the main features of these flows with a reasonable accuracy.

3.2 Results

To test the new compressible scalar FMDF model, the scalar mixing and heat transfer in three different flows are considered. As shown below, the compressibility effect is important in all three flows.

3.2.1 Rapid compression machine

The first flow configuration is an isotropic turbulent flow going through compression in a simple piston-cylinder assembly, called the rapid compression machine (RCM). The goal of RCM simulation is to study the pressure effect on the FMDF. The experimental set-up for the Michigan State University (MSU) RCM [58] is shown in Fig. 4.1(a). The MSU RCM is somewhat similar to that considered in Ref. [59]. The geometry is axisymmetric and consists of a simple closed cylinder and a flat piston. The compression ratio in the RCM is around 21. To avoid singularity at centerline, a rectangular H-H ($250 \times 13 \times 13$) block was employed at the center, coupled with an O-H ($250 \times 45 \times 42$) grid outside. Figure 4.1(b) shows the 3D and 2D views of the grid. The geometrical parameters and piston movement are similar to those used in MSU RCM experiment, even though the exact shape of the piston is different. During the flow compression, adaptive grid compression is used, while the number of grids is not changed. At the beginning of compression, it is assumed that the initial temperature in the cylinder is 300 K and the pressure is atmospheric. The walls are assumed to be adiabatic. To include the pressure effect in the FMDF, the derivative of filtered pressure ($"D\langle p \rangle_l / Dt"$), as computed from the FD data are interpolated and added to the corresponding MC particles. Consistency of the predicted temperatures obtained by the Lagrangian MC method, with those calculated by the FD solution of carrier-gas equations over Eulerian grids is dependent on the inclusion of $"D\langle p \rangle_l / Dt"$ in the FMDF equation. This is clearly demonstrated in Fig. 3.2(a), where the spa-

tial variations of the gas temperature along the cylinder centerline at different piston locations (locations (1) to (5) in Fig. 3.2(b)) or different times are shown. In this figure, solid lines, square symbols, and dotted lines with delta symbols represent FD, MC with " $D\langle p\rangle_l/Dt$ ", and MC without " $D\langle p\rangle_l/Dt$ " results, respectively. A comparison between MC results obtained with and without " $D\langle p\rangle_l/Dt$ ", indicate the critical role of pressure in the FMDF equation during the compression in the RCM. There seems to be a good consistency between the FD and MC results when " $D\langle p\rangle_l/Dt$ " is included in the FMDF equation. It should be mentioned that, since the flow in the RCM is low Mach number, the term " $\langle u_i\rangle_L \partial \langle p\rangle_l / \partial x_i$ " in the enthalpy equation is small and can be ignored, i.e. $D\langle p\rangle_l/Dt \approx \partial \langle p\rangle_l / \partial t$.

3.2.2 Shock tube

The second flow considered in this chapter is that in a shock tube. We have simulated this flow with the LES/FMDF model using a 3D rectangular H-H ($190 \times 32 \times 32$) grid, but compared the results with the 1D inviscid analytical solution. Wall boundary condition is used for the first and last points in the axial direction, but the flow is assumed to be periodic in other directions. The initial condition is based on Sod's shock tube solution [60] with initial pressure ratio of $p_h/p_l = 10$ and density ratio of $\rho_h/\rho_l = 8$. For the FMDF simulation, MC particles are randomly distributed in the computational domain based on Sod's solution at initial time. In order to assess the performance of the artificial viscosity, two sets of simulations are performed with and without artificial viscosity. In Figs. 3.3(a) and (b), the pressure and velocity as predicted by the compact differencing without artificial viscosity at $t = 0.2$ are compared with those obtained by the compact differencing with artificial viscosity. Analytical solution for the 1-D inviscid shock tube problem are also shown. The numerical oscillations in flow variables are shown to decrease when the artificial viscosity is added.

Figure 3.4 shows the FMDF-MC temperature for different pressure models and its comparison with the LES-FD temperature and the analytical solution. In this figure, the dash-dotted line with the diamond symbols represents the FMDF results without " $D\bar{p}/Dt$ ". Without the pressure term, MC particles can not correctly predict the temperature in the vicinity of the shock wave, the contact surface and expansion waves. The FMDF results with " $\partial \langle p \rangle_l / \partial t$ " are closer to the analytical results and shows a better consistency with those obtained by the FD in Fig. 3.4. However, a good consistency between LES-FD and FMDF-MC may not be achieved with just " $\partial \langle p \rangle_l / \partial t$ " term and " $\langle u_i \rangle_L \partial \langle p \rangle_l / \partial x_i$ " term is also important at high Mach number flows. This is demonstrated in Fig. 3.4, where it is shown that the MC results are fully consistent with the FD results when " $D \langle p \rangle_l / Dt$ " term, calculated with the limiter, is added to the MC particles. Without the limiter, the spatial derivative of pressure has some unphysical oscillations, which lead to the under-prediction of MC temperature.

Figure 3.5 shows the weighted MC particle number density for the cases with 6, 24 and 48 initial particles per cell in comparison to LES-FD predicted densities. The filtered density obtained from FMDF-MC data are also shown. As mentioned before, the filtered fluid density calculated from the MC particles via Eq. (2.38) and the weighted particle number density calculated by Eq. (2.36) should be equal to the filtered density calculated by the FD. Oscillatory results for the weighted MC particle number density are expected, as they are obtained by averaging of Lagrangian particles' weight within each cell. However, by increasing the initial number of MC particles, the oscillations decrease and the predicted weighted particle number density converges to the filtered fluid density. The results In Figs. 3.5(a)-(c) confirm the correct transport of MC particles even in the presence of a strong shock wave. In Fig. 3.5(d), the filtered density calculated from the MC particles is compared with those obtained from FD data and the analytical solution. For the FMDF calculations, only 6 MC particle per cell is employed, yet the computed FMDF-MC densities compare

very well with the analytical and LES-FD densities. The oscillations in the weighted particle number density have little effect on the filtered variables calculated from the MC particles. In fact, we found the FMDF-MC predictions of the filtered density to be always consistent with the LES-FD predictions for all tested particle/flow conditions at all times.

3.2.3 Co-axial helium-air jet

The third flow configuration considered in this chapter is a supersonic co-axial helium-air jet (Fig. 3.6(a)). The geometry is axisymmetric and consists of a central and an outer concentric annular nozzle passages. The thickness of the central nozzle at the outlet is 0.5 mm. This flow has been studied experimentally and has been simulated with the RANS turbulence models [61, 62]. LES of this flow on a Cartesian grid is also reported [63]. In this work, we use the high order FD model with a 6-block axisymmetric grid and the compressible FMDF model to simulate this flow. Figure 3.6(b) show the 3D and 2D views of the grid. Similar to the grid used for the RCM simulation, the co-annular grid has a rectangular H-H block in the center for avoiding singularity. Respectively, for the nozzles and inner jet flow section about 5×10^5 and 1.5×10^6 FD grid points are employed. The LES/FMDF calculations were performed with the Smagorinsky and MKEV SGS models. The gas mass fraction at the central-nozzle inlet is 0.7039 for the helium (He) and 0.2961 for the oxygen (O_2). The total pressure and density are 628.3 kPa and 1.334 kg/m^3 , respectively. The co-flow at inlet is air with the total pressure and density of 580.0 kPa and 6.735 kg/m^3 , respectively.

Figure 3.7(a) show the instantaneous 3D iso-levels of vorticity magnitude in the entire computational domain as predicted by the LES/FMDF with the MKEV model. The instantaneous 2D contours of vorticity magnitude downstream of nozzles is shown in Fig. 3.7(b). After going through transition, the flow obviously become turbulent

and 3D. High vorticity values are observed in the mixing layer between the jets and in the layer between outer jet and free stream. Figures 3.8(a) and (b) show the instantaneous 2D contours of the scalar in the central flow region as predicted by the Smagorinsky and MKEV models. The predicted mixing layer thickness, based on 99% of $He - O_2$ mole fraction for two SGS models are shown and compared with the experimental data in Fig. 3.8(c). Evidently, mixing layer grows faster with the MKEV model, which is expected. The MKEV results are in good agreement with the experimental data, but the Smagorinsky model fails to predict the correct mixing layer growth. Comparison of time-averaged axial velocity at different locations from the central nozzle with the experimental data in Fig. 3.9, again indicates that the MKEV model is able to predict the experimental data well. However, the predicted (root mean square) rms values of axial velocity in Fig. 3.10 show some deviation from the experiment for both models, even though the MKEV model predictions are much closer to the experimental data. The differences in rms values can be attributed to insufficient grid resolution at the edge of separated plate or to the SGS models.

For the co-annular jet, the scalar statistics are calculated by the FMDF-MC and LES-FD. The pressure term with van Leer limiter and the viscous dissipation term are added to the FMDF equation. Contours of instantaneous filtered temperature as obtained from the FD and MC data are shown in Figs. 3.11(a) and (b), respectively. The scalar contours are shown in Figs. 3.11(c) and (d). Qualitatively, LES-FD and FMDF-FD predictions are consistent in this supersonic problem indicating the reliability of compressible FMDF model for high speed flows. The scatter plots of filtered temperature and scalar as obtained from FD and MC data are presented in Figs. 3.12(a) and (b). There seems to be a high level of correlation between the LES-FD and FMDF-MC results. In order to assess the pressure effect on the FMDF, the local values of temperature predicted by the FMDF-MC without the term " $D \langle p \rangle_l / Dt$ " are compared with those of LES-FD in Fig. 3.12(c). At low temperature regions, the

correlation coefficient is $R = 0.74$ when the " $D \langle p \rangle_l / Dt$ " term is ignored. However, the correlation coefficient increases to $R = 0.97$ by adding the " $D \langle p \rangle_l / Dt$ " term to the FMDF equation. This shows the significance of the pressure term in the shock region. For the supersonic jet problem, the spatial pressure term " $\langle u_i \rangle_L \partial \langle p \rangle_l / \partial x_i$ " is important and should be included in the FMDF equation. Figure 3.13(a) show the time-averaged contours of the pressure term (" $\langle u_i \rangle_L \partial \langle p \rangle_l / \partial x_i$ ") in a 2D plane. Weak and strong shock waves are clearly present in the central nozzle exit region. Nevertheless, the LES predictions are in agreement with the experimental data [61, 62]. Poor correlation of LES-FD and FMDF-MC data in this region of the flow (Fig. 3.12(c)), when " $D \langle p \rangle_l / Dt$ " term is not included in the FMDF, is due to significance of " $\langle u_i \rangle_L \partial \langle p \rangle_l / \partial x_i$ " term in shock region. This is explicitly shown in Fig. 3.13(b), where the scatter plots of temperature, calculated by the FMDF-MC with and without " $D \langle p \rangle_l / Dt$ " term, are compared with those of LES-FD for different " $\langle u_i \rangle_L \partial \langle p \rangle_l / \partial x_i$ " values. The LES-FD temperatures (square symbols) are consistent with the FMDF-MC temperatures when " $D \langle p \rangle_l / Dt$ " is included in the FMDF formulation. In the regions where the values of " $\langle u_i \rangle_L \partial \langle p \rangle_l / \partial x_i$ " are noticeable, the LES-FD and FMDF-MC predictions deviate significantly when " $D \langle p \rangle_l / Dt$ " term is removed from the FMDF equation.

Time-averaged contour plots of $He - O_2$ mass fraction as predicted by the LES-FD and FMDF-MC models are shown in Figs. 3.14(a) and (b) to be also consistent. Furthermore, Fig. 3.14(c) also show that the scalar mass fraction is predicted very differently with the Smagorinsky and MKEV models. Similar to that shown in Figs. 3.9 and 3.10 for the mean and rms of axial velocity, the Smagorinsky model cannot capture the scalar evolution in this flow, but the MKEV predictions are in good agreement with the experimental data. Figure 3.14 also confirm that the FMDF-MC and LES-FD results are consistent with each other at different times throughout the simulation. This is very important as it shows that the numerical solution of FD

and MC parts of the hybrid LES/FMDF model are both accurate. Time-averaged values of temperature in Fig. 3.15 like those shown for the $He - O_2$ mass fraction in Fig. 3.14(c) show that the LES-FD and FMDF-MC predictions are consistent. The computed rms of resolved $He - O_2$ mass fraction and temperature fields by the FMDF-MC and LES-FD in Fig. 3.16(a) and (b) are also in good agreement with each other; further indicating the accuracy and the reliability of the LES/FMDF model for supersonic turbulent flows.

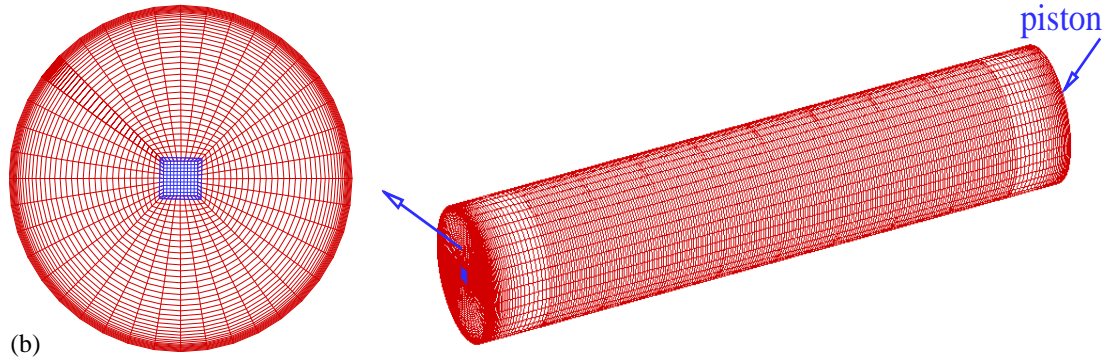
3.3 Conclusions

The scalar filtered mass density function (FMDF) model is further developed and extended for large-eddy simulations (LES) of compressible turbulent flows by including the effect of pressure in the FMDF transport equation. The new compressible scalar FMDF model is applied to three subsonic and supersonic problems: an isotropic turbulent flow going through compression in a piston-cylinder assembly, a three-dimensional shock tube, and a co-axial supersonic helium-air jet. For the piston cylinder assembly and shock tube, the consistency of finite-difference (FD) and Monte Carlo (MC) parts of the hybrid LES/FMDF model is established by adding the total derivative of pressure to the FMDF equation. For the co-axial helium-air jet, LES with the MKEV SGS model was able to predict the experimental values of the velocity and scalar at different locations. The FMDF-MC predictions for the scalar mass fraction and temperature are also shown to be consistent with those of LES-FD in this flow, further indicating the reliability and applicability of the compressible LES/FMDF model to high speed turbulent reacting flows. The compressible scalar FMDF model is only applied to non-reacting flows in this chapter. Reacting results will be presented in future works. To develop a more accurate SGS PDF model for LES of high speed turbulent reacting flows, a more complete formulation

of the FMDF based on the joint velocity-frequency-energy-pressure-scalar FMDF has to be considered. However, the scalar FMDF model is computationally much less demanding and is applicable to practical combustion systems.



(a)



(b)

Figure 3.1: (a) Experimental set-up of the rapid compression machine (RCM) [58]. (b) 3-dimensional and 2-dimensional views of the 2-block grid used for the RCM simulation.

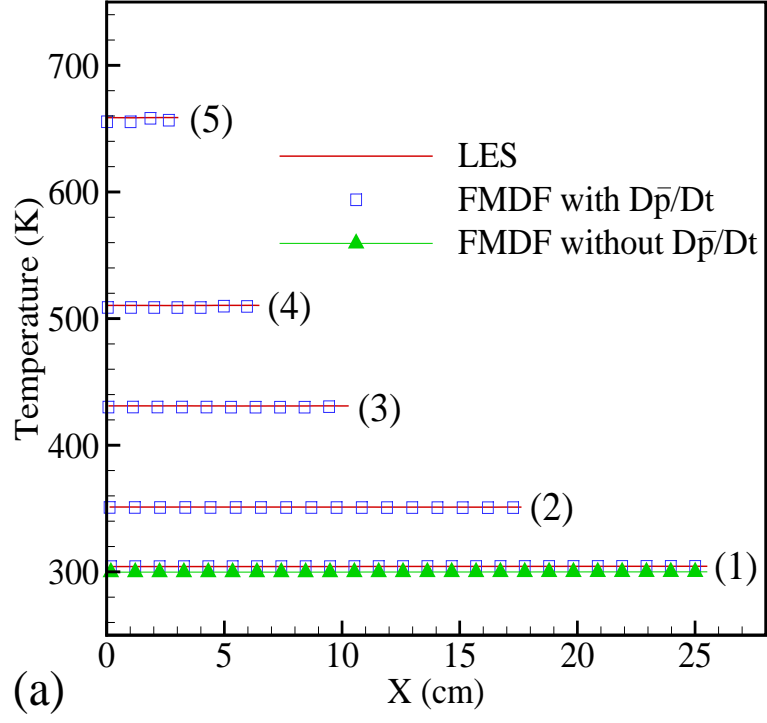


Figure 3.2: (a) Temperatures obtained from the finite difference (FD) and Monte Carlo (MC) data at different piston locations during the compression in the rapid compression machine. (b) Different piston locations during the compression.

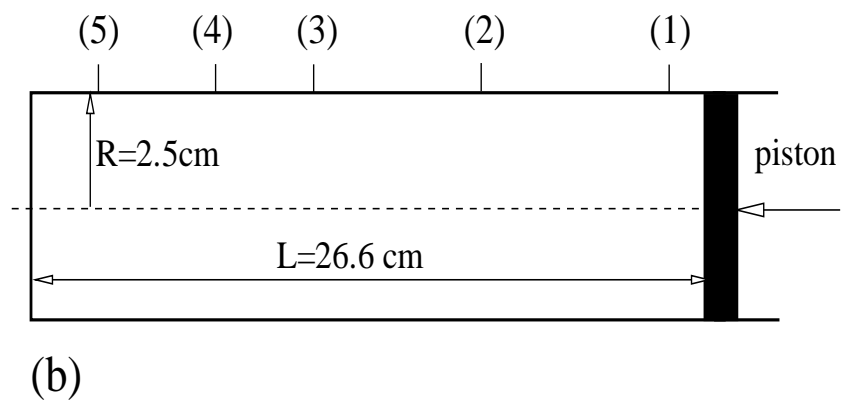


Figure 3.2 continued.

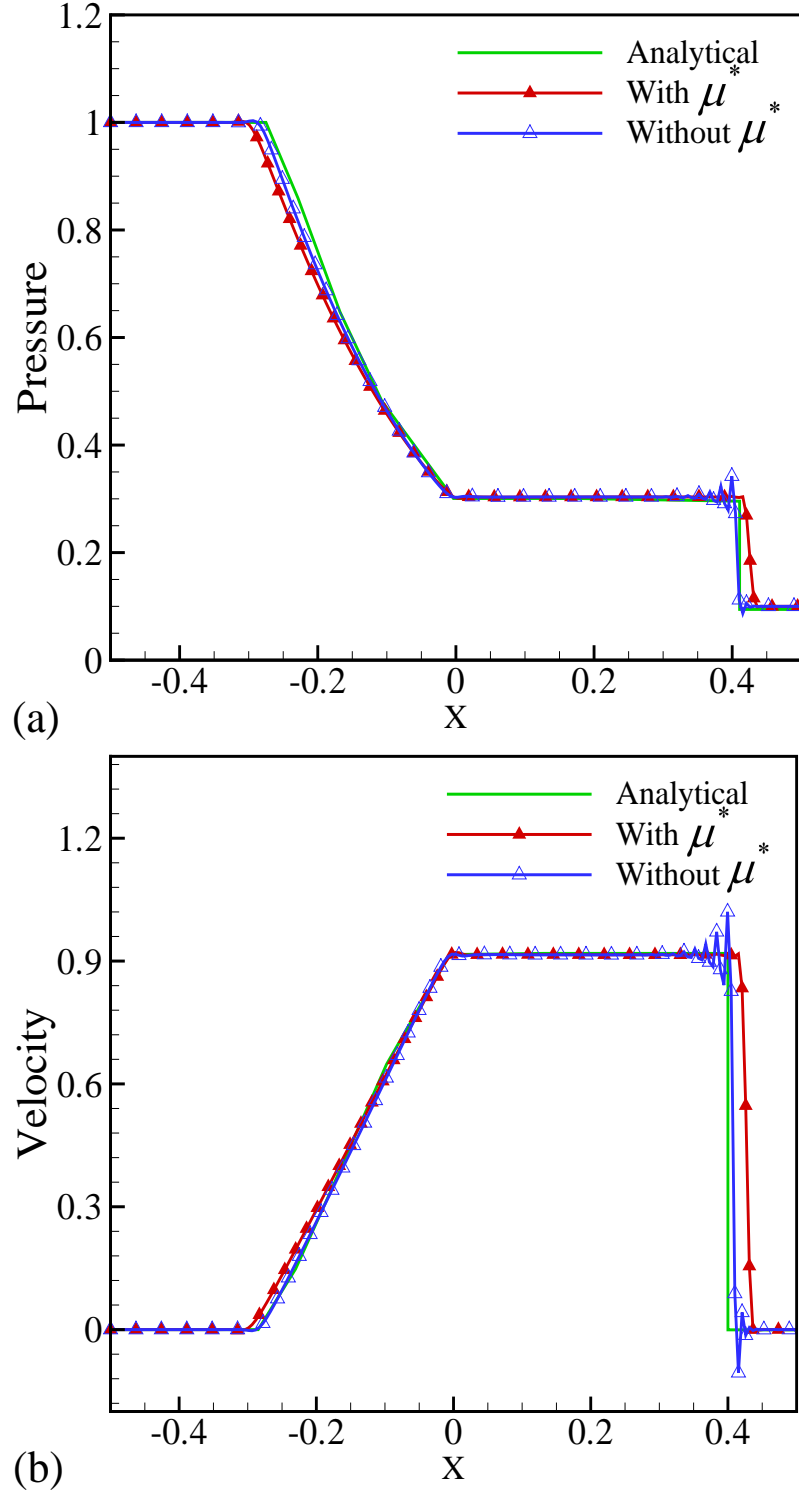


Figure 3.3: Comparison of (a) pressures and (b) velocities obtained by the FD with artificial viscosity (solid lines with solid triangular symbols) and without artificial viscosity (solid lines with hollow triangular symbols) with the analytical solutions (solid lines no symbol) for Sod's shock tube problem.

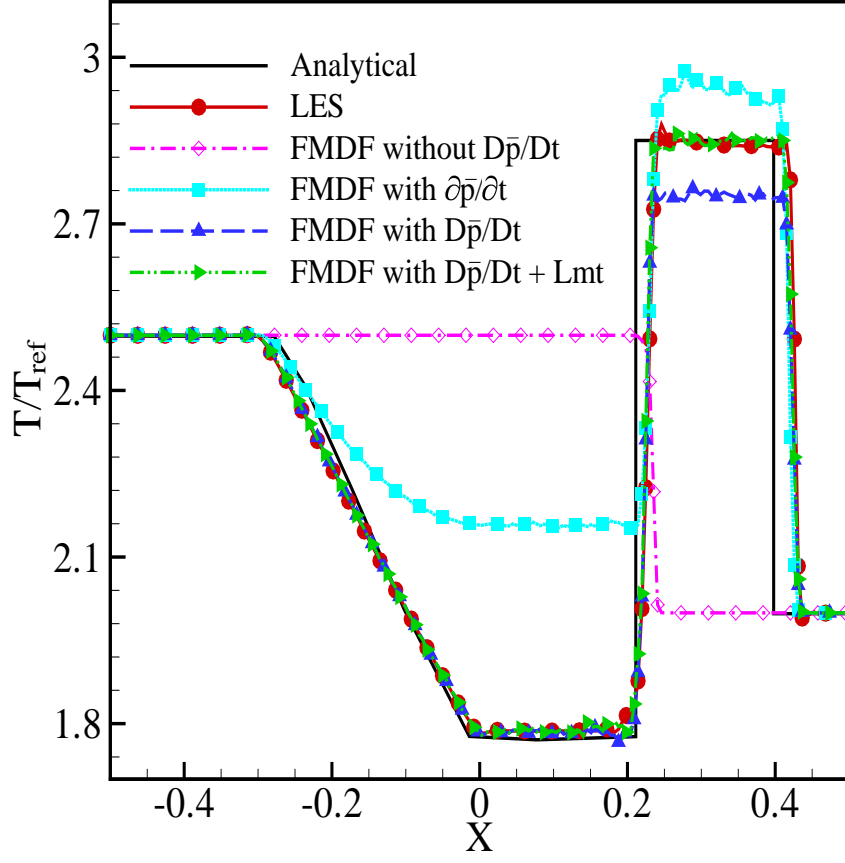


Figure 3.4: Comparison of temperatures, obtained by the FD, MC without $'D\bar{p}/Dt'$, MC with $'\partial\bar{p}/\partial t'$, MC with limiter on $'D\bar{p}/Dt'$ for the Sod shock tube problem.

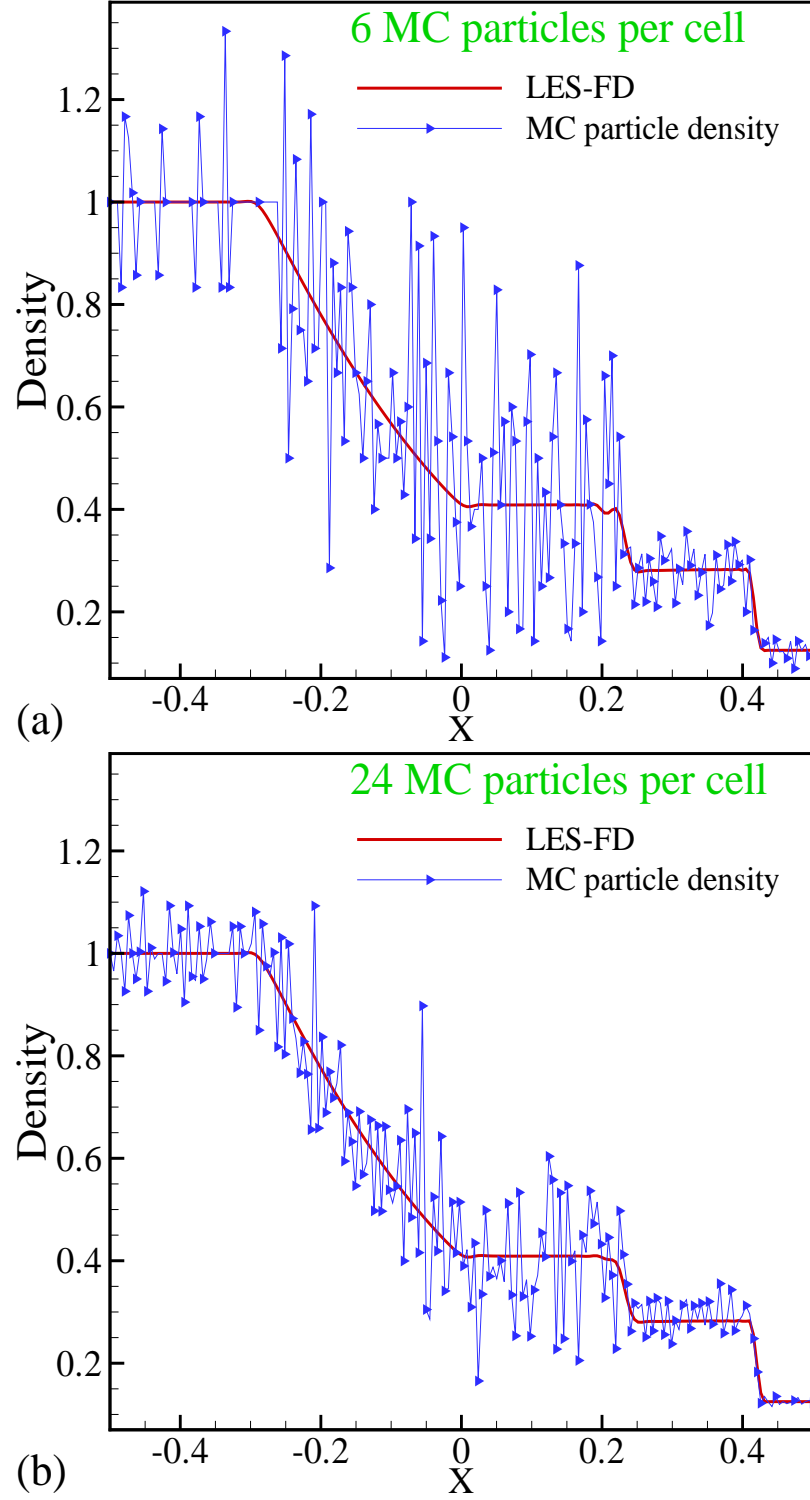


Figure 3.5: Comparison of LES-FD filtered densities with the MC particle weighted number density calculated by Eq. (2.36) with (a) 6, (b) 24 and (c) 48 MC particles per cell. (d) Comparison of LES density with MC density calculated by Eq. (2.38).

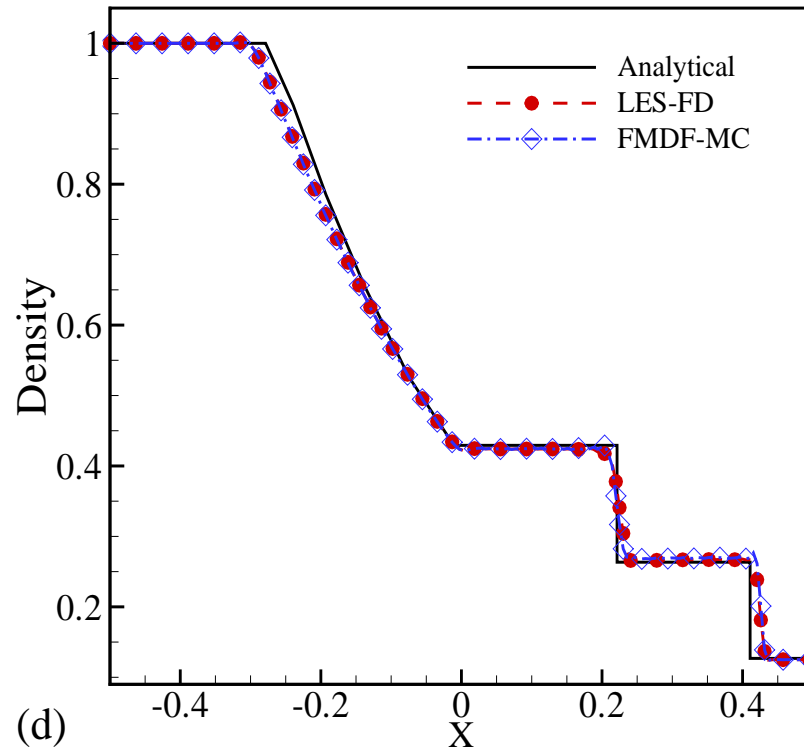
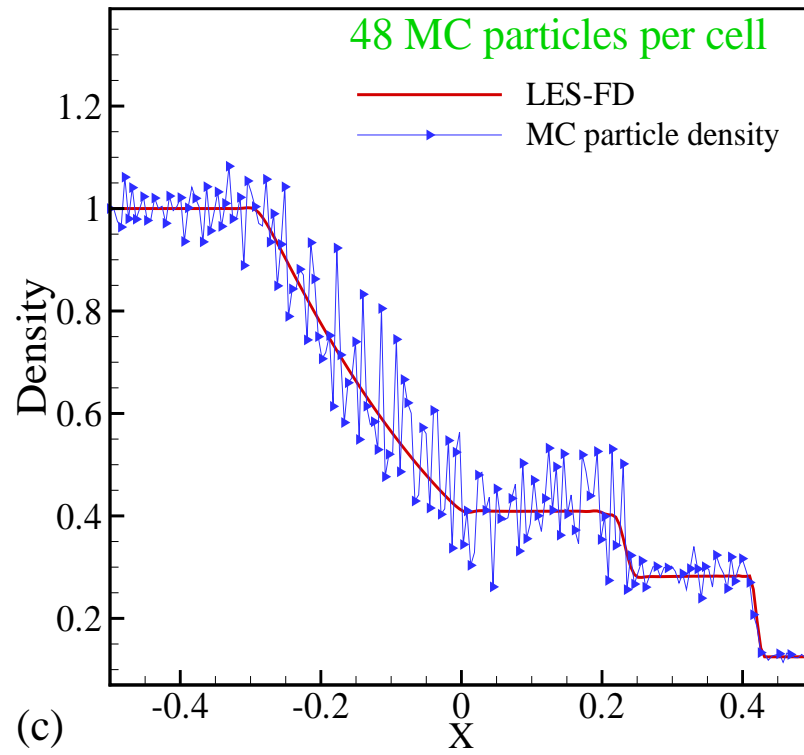


Figure 3.5 continued.

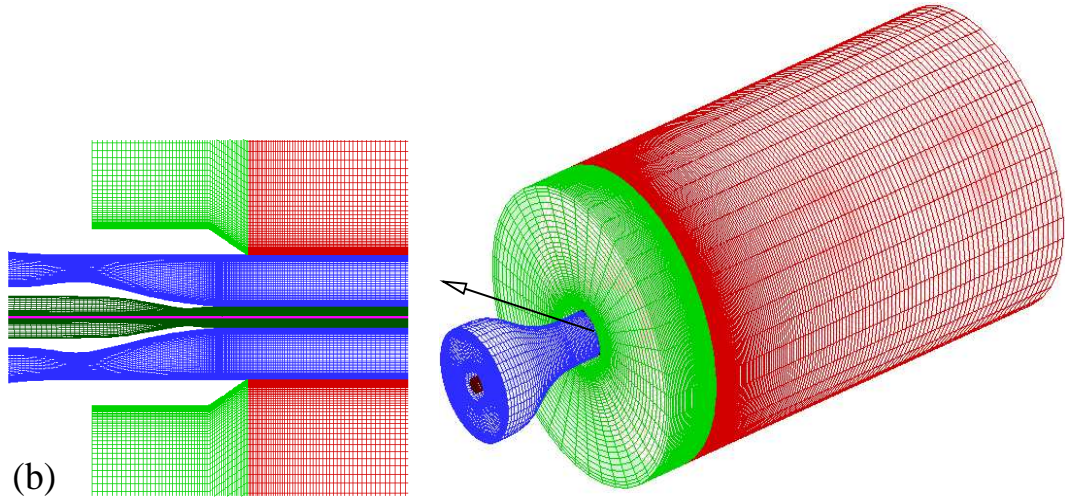
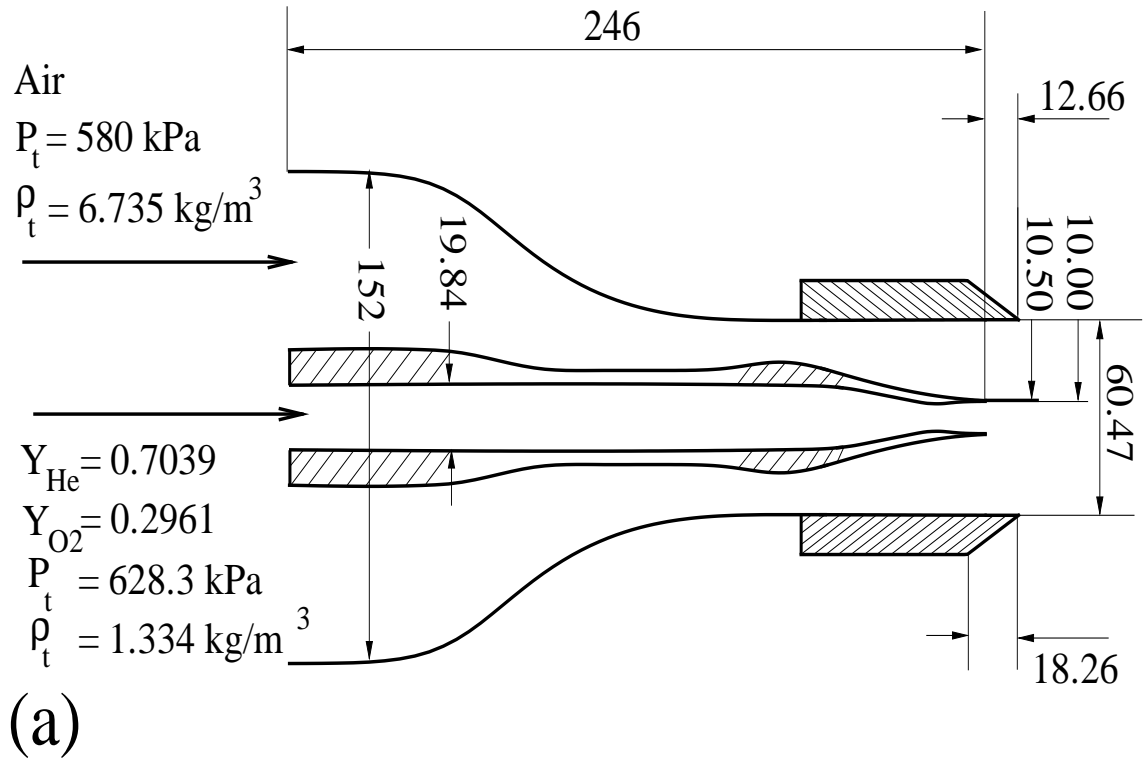


Figure 3.6: (a) Geometrical details of the supersonic co-annular jet (Dimensions given in mm), and (b) three-dimensional and two-dimensional views of the 6-block grid.

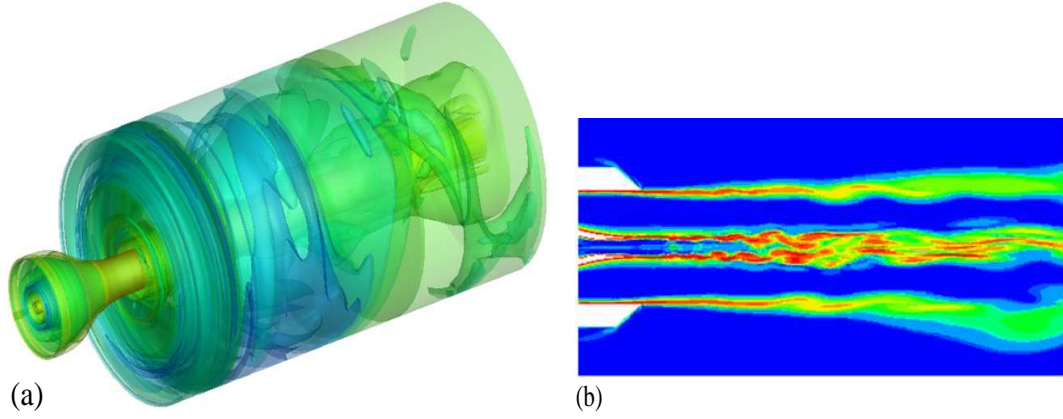


Figure 3.7: Instantaneous (a) three-dimensional and (b) two-dimensional contour plots of vorticity for the supersonic co-annular jet.

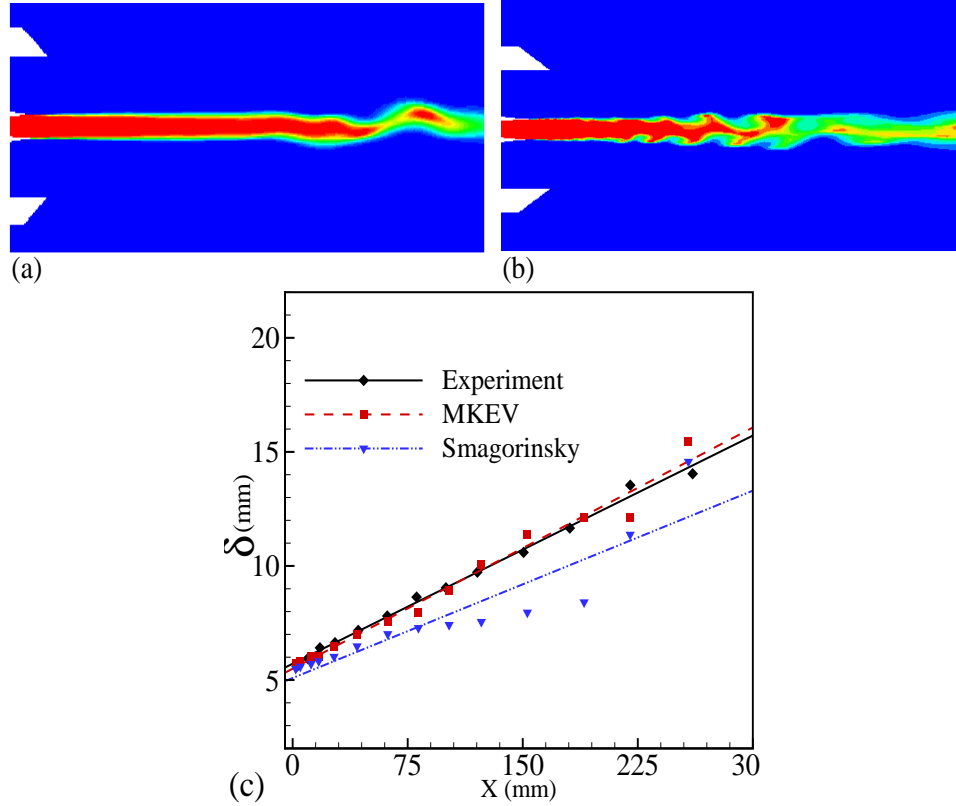


Figure 3.8: Instantaneous contours of the scalar at central region of the flow, the downstream of nozzles as predicted by the (a) Smagorinsky and (b) MKEV models. (c) Comparison of the mixing layer thickness predicted by the MKEV model (dashed line with the square symbols) and the Smagorinsky model (dashed double dot line with the triangle symbols) with the experimental data (solid line with diamond symbols).

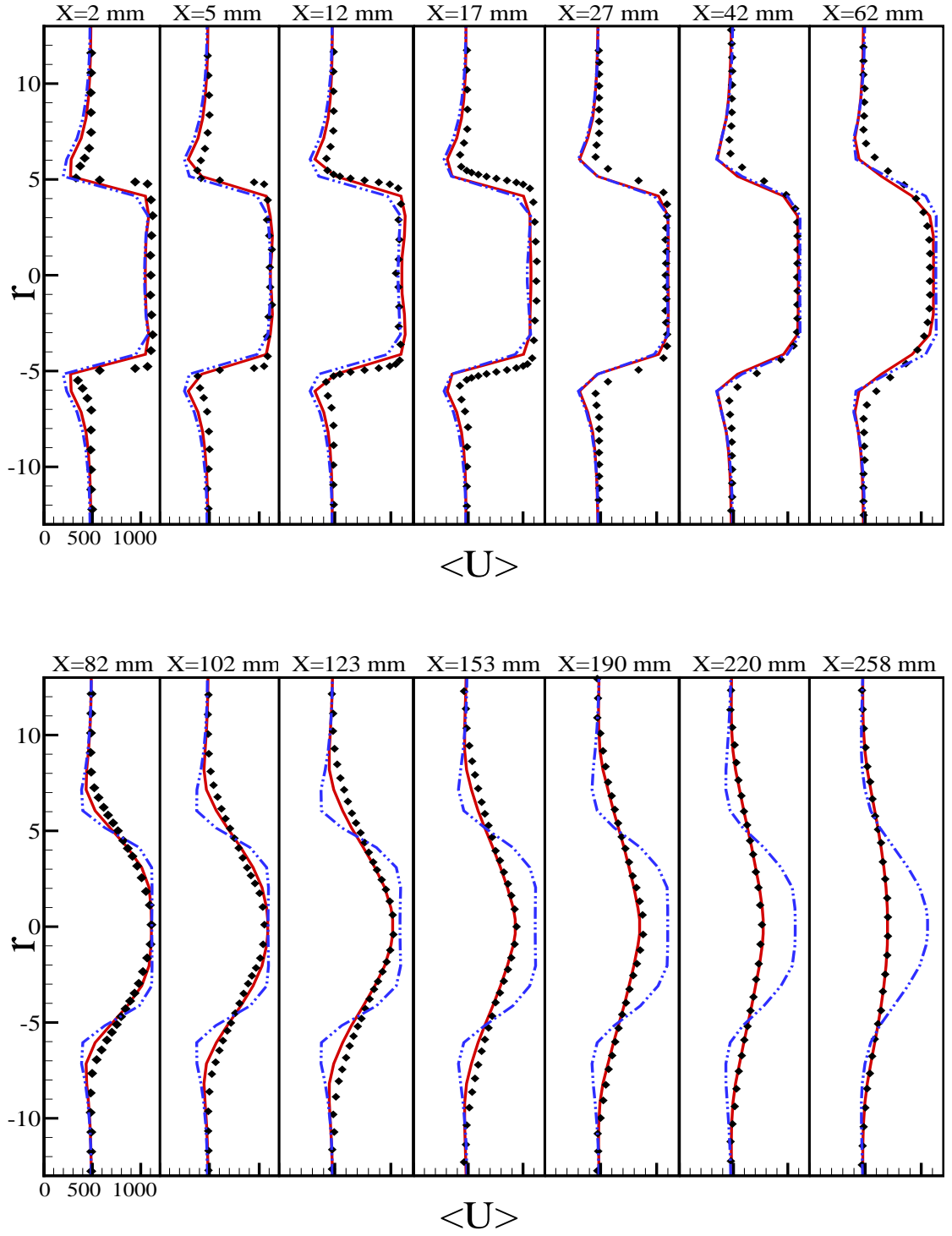


Figure 3.9: Comparison of time-averaged axial velocity as predicted by the MKEV model (solid lines) and the Smagorinsky model (dashed double dot lines) with the experimental data (symbols) at different radial (r) and axial (X) locations.

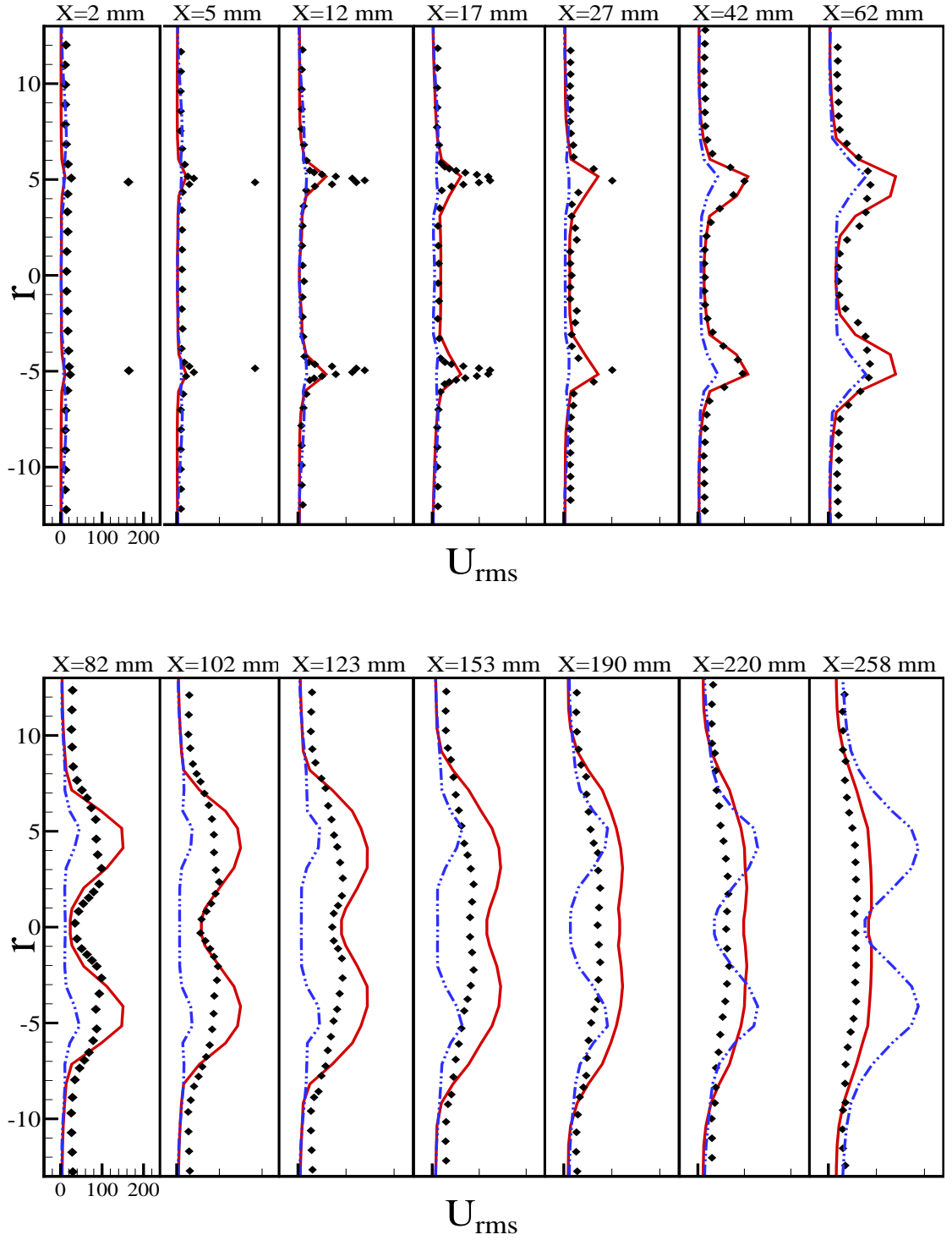


Figure 3.10: Comparison of the root mean square values of axial velocity, predicted by the MKEV (solid lines) and the Smagorinsky model (dashed double dot lines), with the experimental data (symbols).

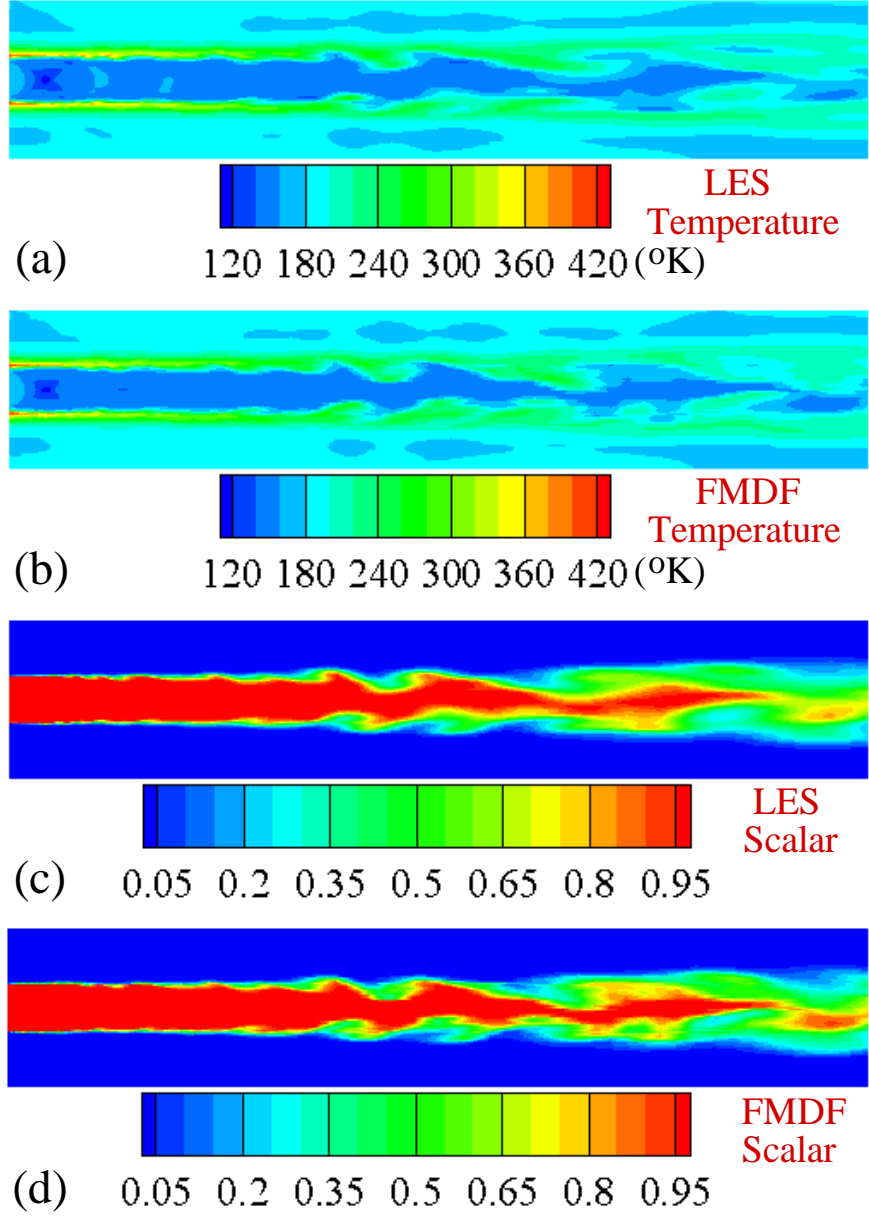


Figure 3.11: Instantaneous two-dimensional contour plots of filtered temperature predicted by the (a) LES-FD, (b) FMDF-MC, and instantaneous contour plots of the scalar mass fraction predicted by the (c) LES-FD, (d) FMDF-MC.

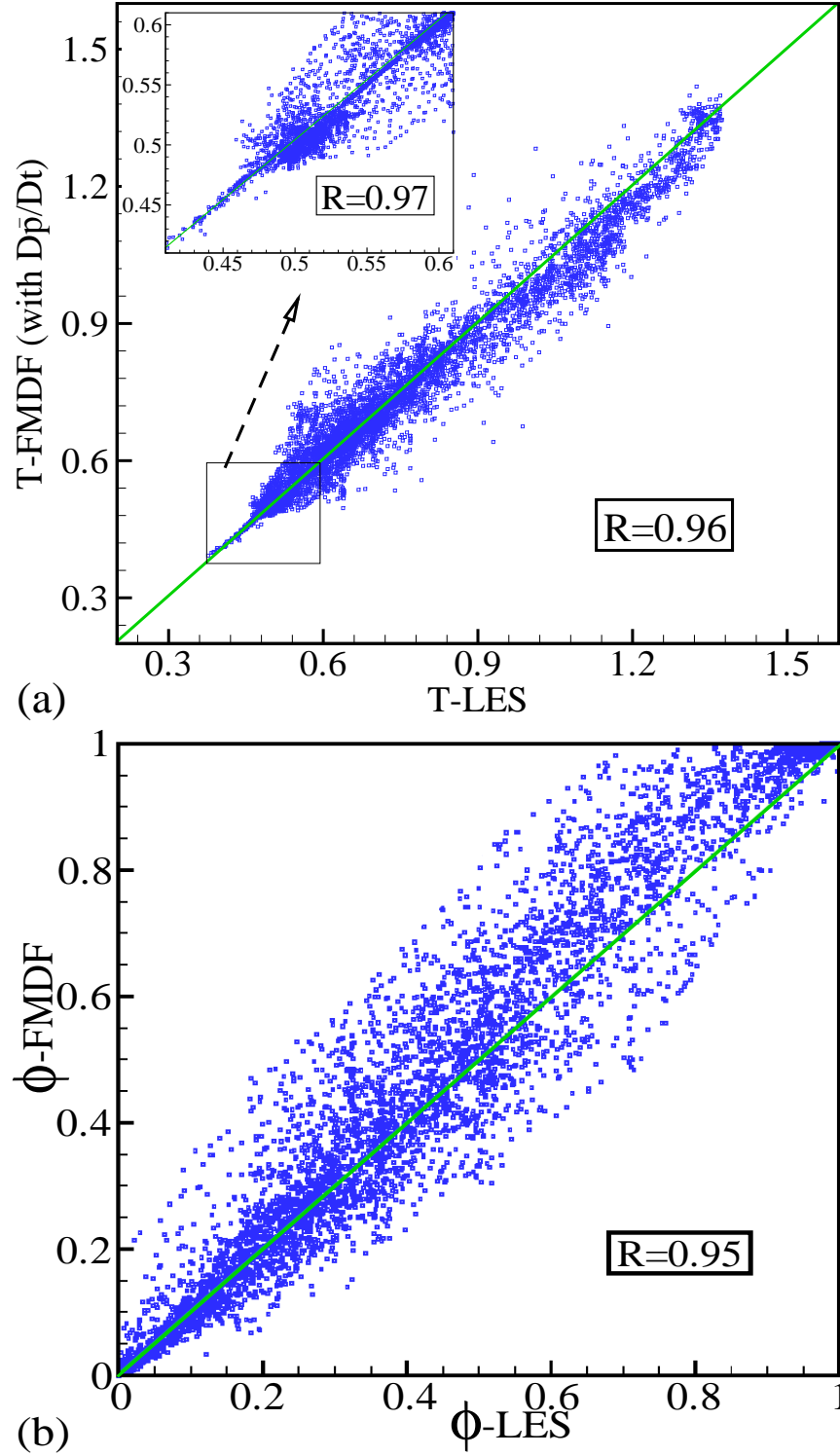


Figure 3.12: (a) Scatter plots of the temperature predicted by LES-FD and FMDF-MC with " $D\langle p \rangle_l/Dt$ ". (b) Scatter plots of scalar mass fraction predicted by LES-FD and FMDF-MC. (c) Scatter plots of the temperature, predicted by LES-FD and FMDF-MC without " $D\langle p \rangle_l/Dt$ ". The solid lines are the 45° lines. "R" denotes the correlation coefficient.

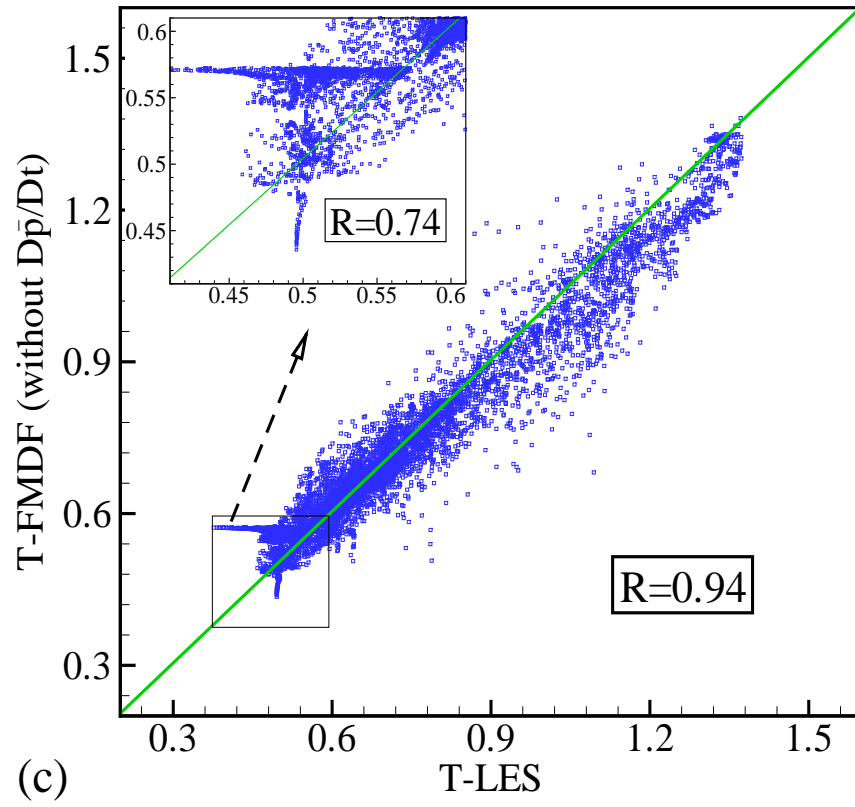


Figure 3.12 continued.

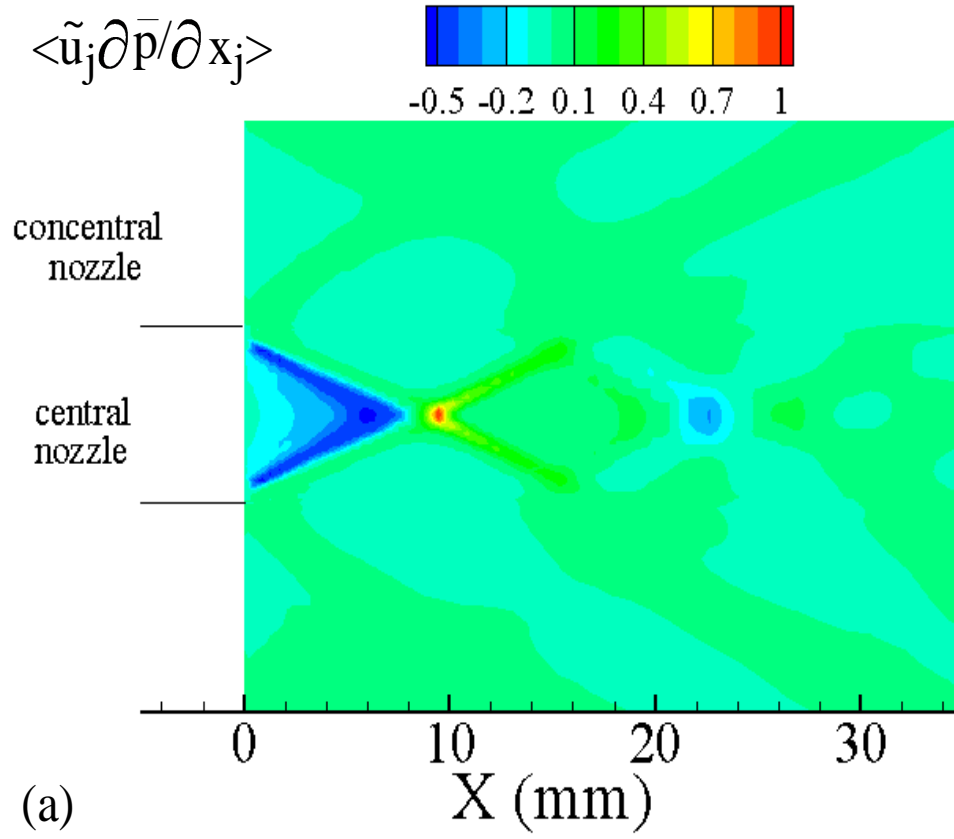


Figure 3.13: (a) Time-averaged contours of " $\langle u_j \rangle_L \partial \langle p \rangle_l / \partial x_j$ " term downstream of the nozzles. (b) Scatter plots of the temperature versus " $\langle u_j \rangle_L \partial \langle p \rangle_l / \partial x_j$ " term.

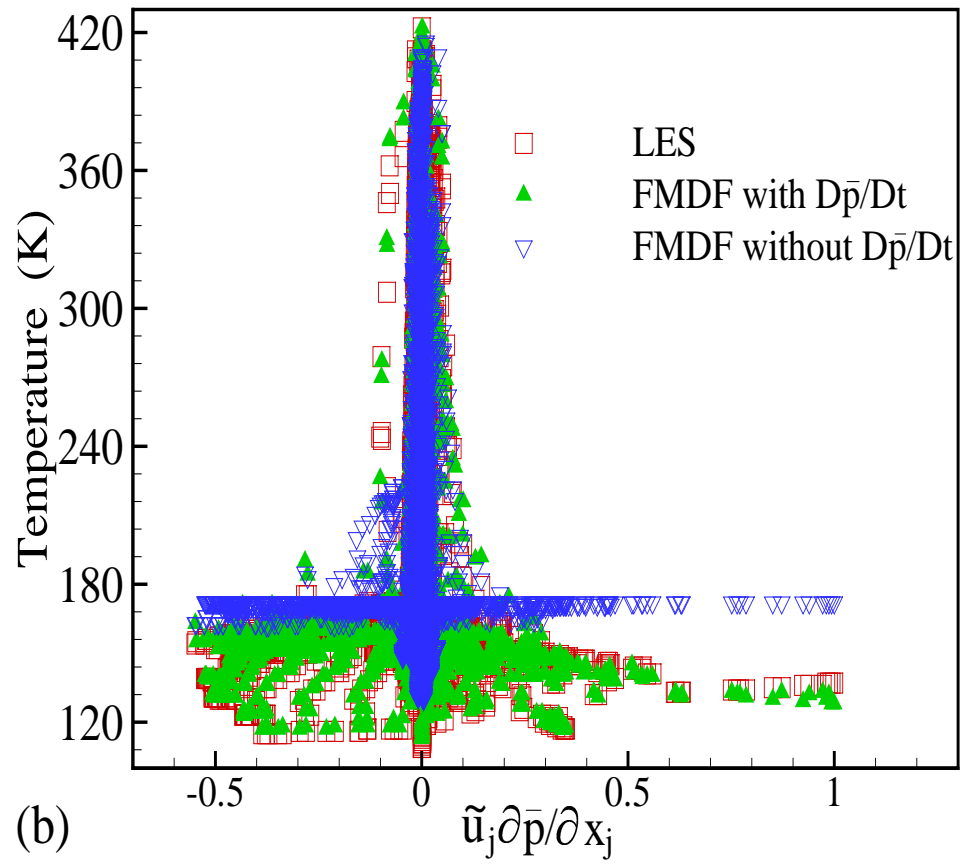


Figure 3.13 continued.

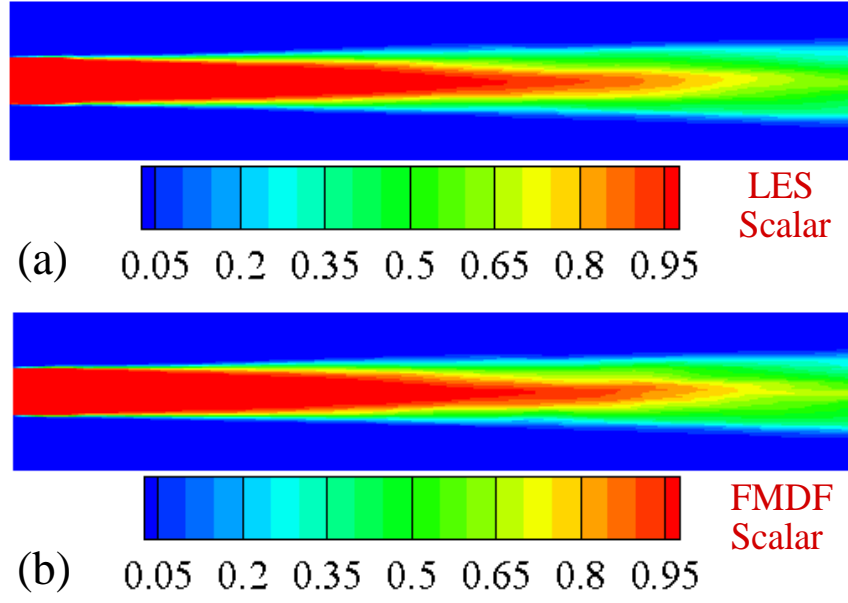


Figure 3.14: Time-averaged contours of $He - O_2$ mass fraction predicted by (a) LES-FD, (b) FMDF-MC. (c) Comparison of the time-averaged $He - O_2$ mass fraction, obtained with the LES-FD and MKEV model (solid lines), LES-FD and Smagorinsky model (dashed dot lines) and FMDF-MC model (dashed dot lines with hollow symbols) with the experimental data (solid symbols).

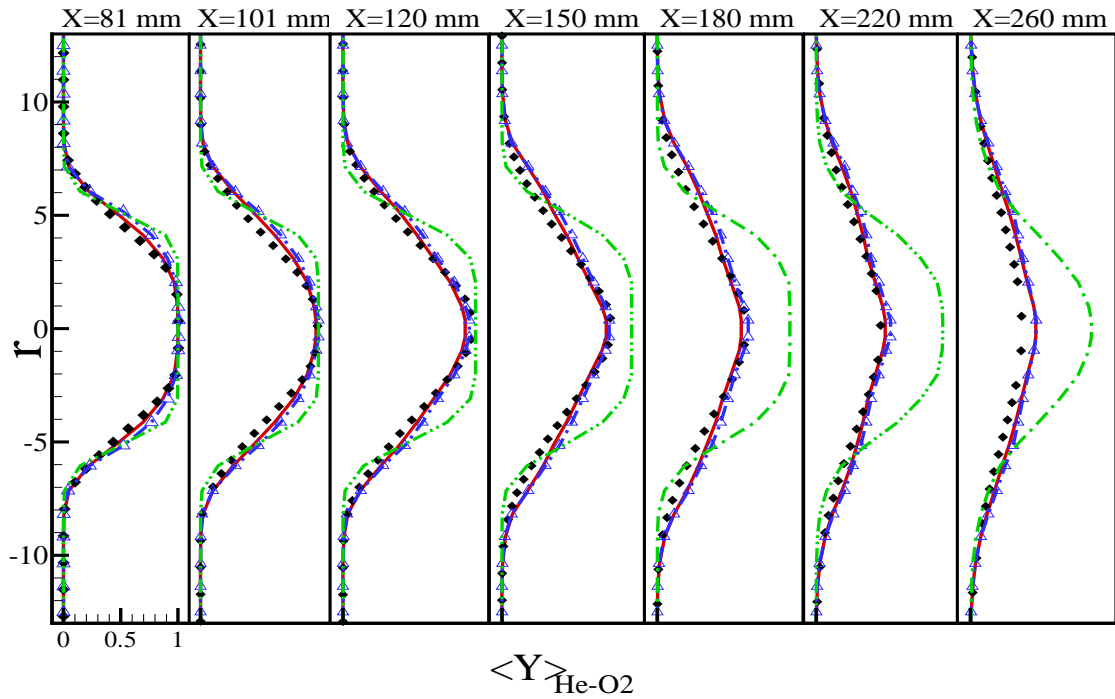
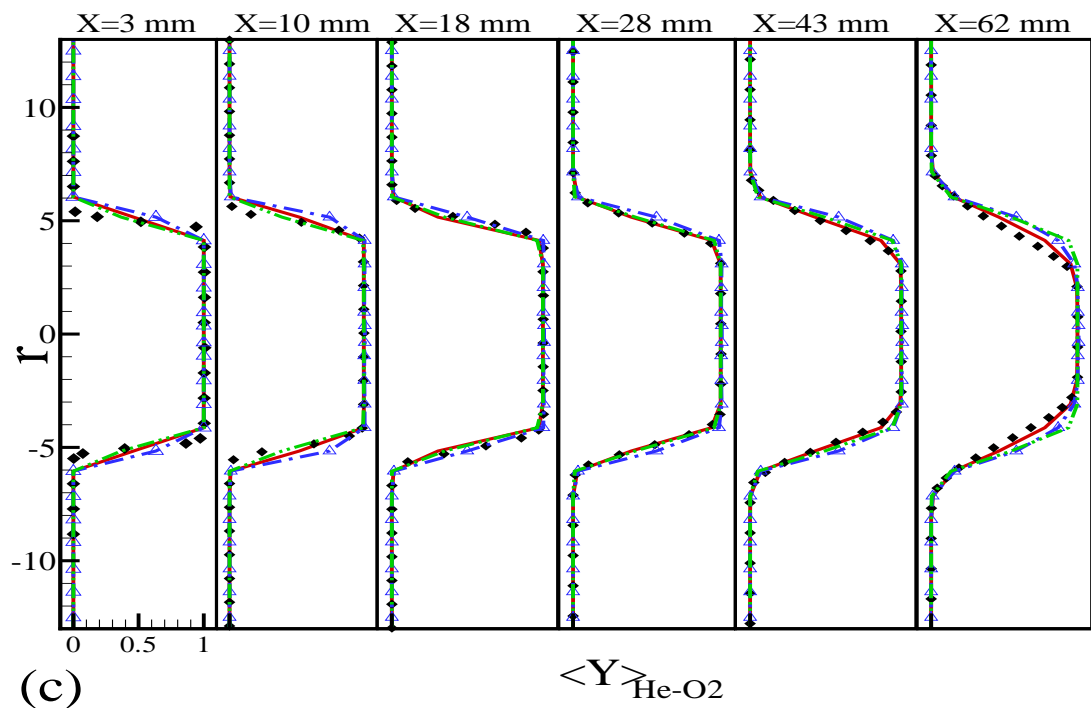


Figure 3.14 continued.

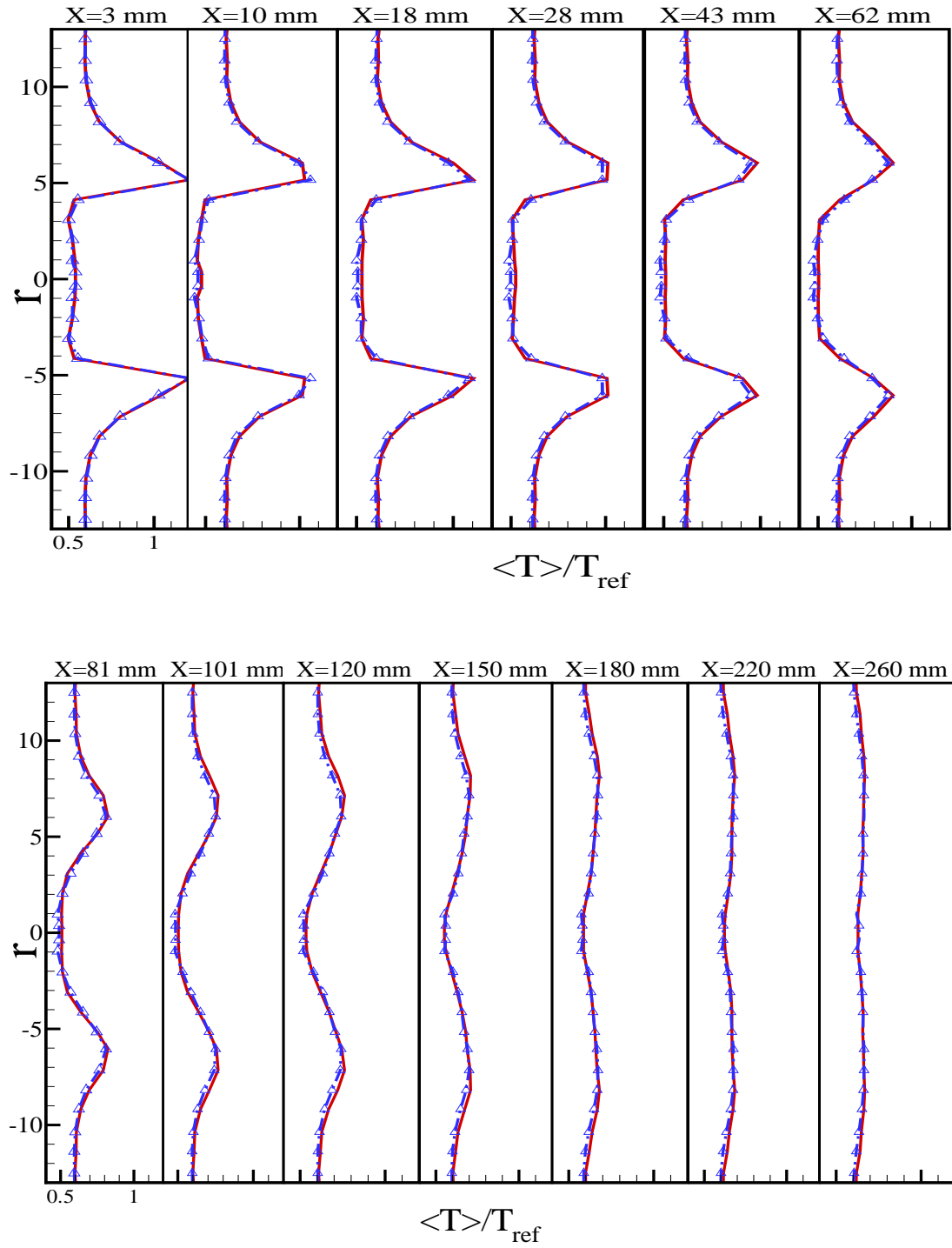


Figure 3.15: Time-averaged values of the filtered temperature predicted by the LES-FD (solid lines) and the FMDF-MC (dashed dot lines with hollow symbols). $T_{ref} = 300$.

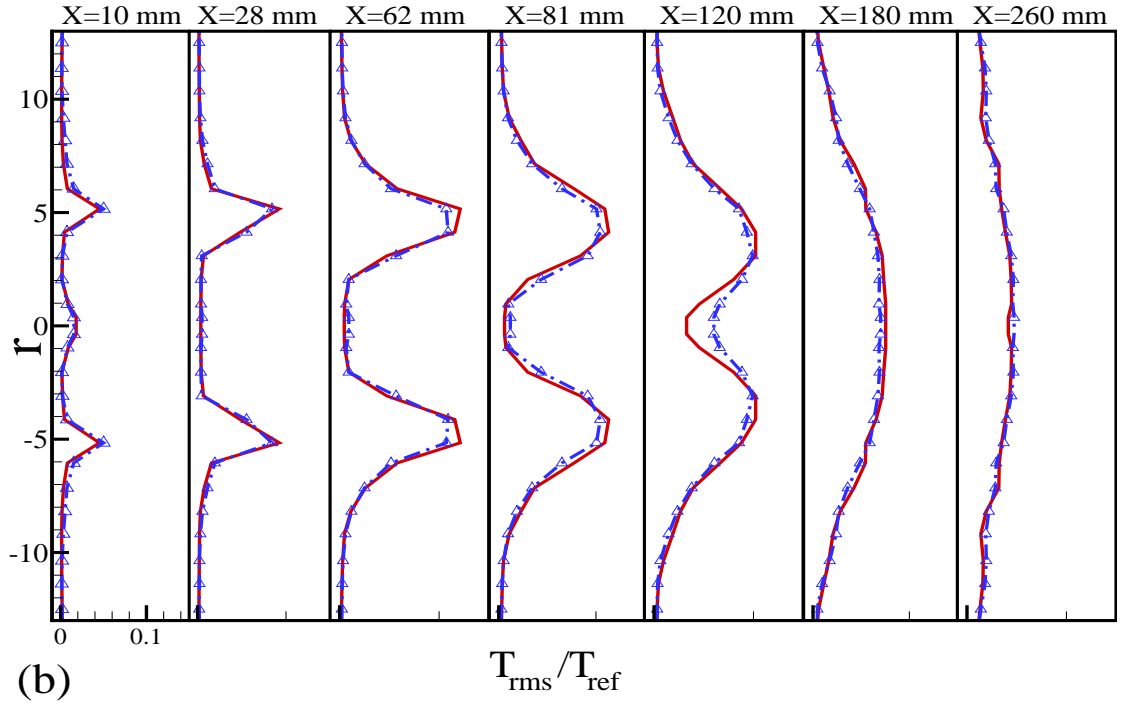
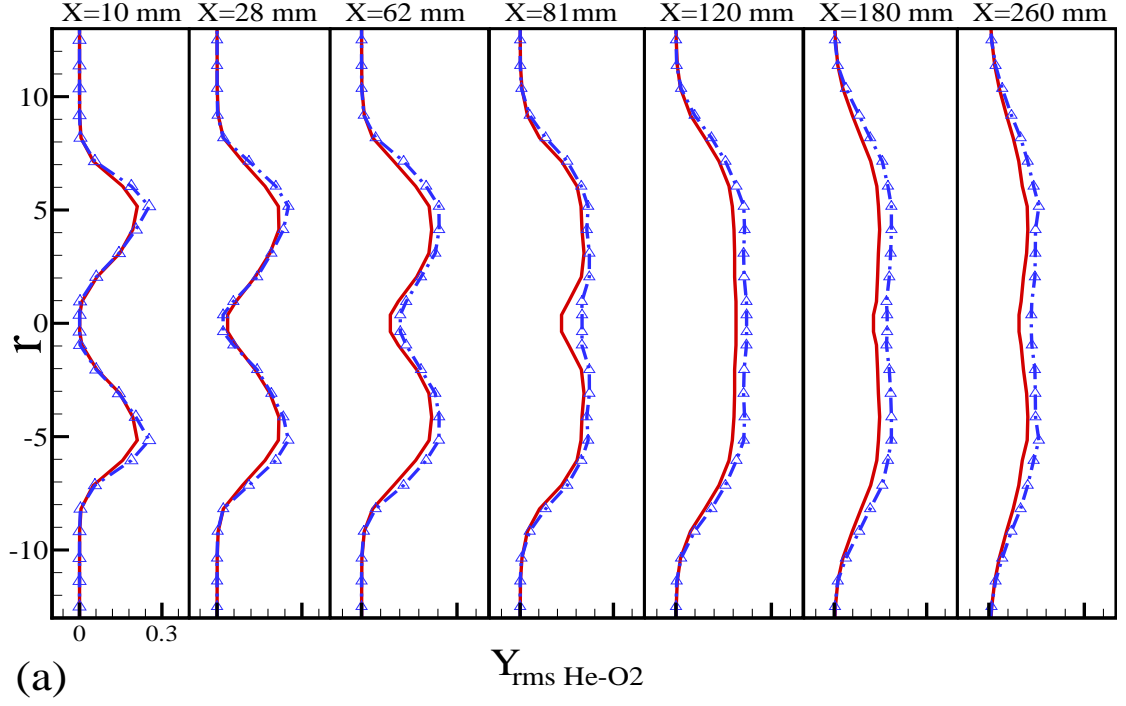


Figure 3.16: Root mean square values of the filtered (a) scalar mass fraction and (b) temperature predicted by the LES-FD (solid lines) and the FMDf-MC (dashed dot lines with hollow symbols). $T_{\text{ref}} = 300$.

Chapter 4

LES of fluid flow and combustion in RCMs

4.1 Introduction

Rapid compression machine (RCM) is a piston cylinder assembly that is used for fundamental studying of combustion and chemical kinetics of various fuels at different temperatures and pressures. Ideally, the flow in the RCM will be fully homogeneous, mimicking zero-dimensional condition for combustion. However, it has been shown in the past that the in-cylinder flow in the RCMs is not uniform and the fluid dynamics and heat transfer affect the combustion [64, 65, 66]. Numerical study of in-cylinder flows in the RCMs is somewhat limited. Majority of previous studies are based on 2-dimensional (2D) axisymmetric mathematical models with laminar flow conditions or Reynolds averaged Navier-Stokes (RANS) turbulence models. Griffiths et al. [64] used KIVA-II with standard $k - \epsilon$ turbulence model and detailed chemistry to simulate the in-cylinder flow in an RCM using 2D axisymmetric grid. Lee et al. [65] used KIVA-III to calculate the velocity and temperature for both crevice and flat piston in an RCM. They showed (theoretically and numerically) that the creation of roll-up vortex in

front of the piston can be eliminated by using a crevice piston. Numerical studies of flow in a twin piston RCM is reported by Wurmel et al. [67]. They used STAR-CD software and employed a 2D axisymmetric grid for a flat and crevice pistons. In their calculations, crevice piston parameters such as volume, location and geometry of the channel connecting the crevice and the cylinder were optimized to generate more homogeneous flow. Mittal et al. [59] used STAR-CD to simulate the fluid flow and heat transfer in their RCM with both flat and crevice piston. They found that the numerical predictions via standard $k-\epsilon$ turbulence models to be not comparable with the experimental data. However, the numerical results without turbulence model are found to be acceptable. In other works, Mittal et al. [68, 69], used FLUENT and CHEMKIN to study the hydrogen ignition and two-stage ignition in their RCM.

There are some studies on the application of large-eddy simulation (LES) to the flow in internal combustion engines [71, 70, 72, 73, 74, 75, 76, 77, 78, 79, 80, 81, 57]. High fidelity computational models based on the LES concept, are relatively inexpensive and can provide detailed time-dependent spatial data for in-cylinder flows. However, complete 3D LES of in-cylinder flow, spray and combustion in realistic RCMs have not been reported. In this work, the fluid flow, the spray and the combustion in an RCM are simulated at different conditions with high-order two-phase compressible LES scalar filtered mass density function (FMDF) model. FMDF is one of the most promising models for LES of turbulent reacting flows which is developed based on the solution of the subgrid scale (SGS) probability density functions (PDF) of energy and species mass fractions [18, 19, 44, 45, 42, 43]. In this approach, the joint statistics of turbulent variables at subgrid level are obtained by solving the transport equation for the single-point joint SGS PDFs of these variables. One of the main advantage of the PDF method is that the single-point statistics appear in a closed form. The other advantage is that higher order statistical information are naturally available from the model. However, single-point PDF equations are not completely closed, and some

form of modeling for multi-point correlations are needed. Jaber et al. [19] developed a PDF model for LES based on the scalar FMDF. Again, in the scalar FMDF transport equation, all chemical source or sink terms are closed, making the FMDF very attractive for turbulent combustion simulations. Several applications of scalar FMDF are recently reported [46, 4, 53, 54, 82]. FMDF for velocity [47], velocity-scalar [48, 49, 50, 51], and frequency-velocity-scalar FMDF [52] are also developed. More recently, the scalar FMDF model is extended to multiphase combustion in realistic configurations. The new multiphase LES/FMDF methodology is implemented through an efficient Lagrangian-Eulerian-Lagrangian mathematical/computational methodology [57, 55, 56, 31]. Most of two-phase LES models are developed for non-reacting turbulent flows; the application of LES models to turbulent flows involving droplet evaporation and combustion is somewhat limited [55, 83, 84, 85, 86, 87, 88, 89].

In this study, the flow, the spray and the combustion in RCM are simulated with our new high-order two-phase compressible scalar LES/FMDF model. The main objectives are to develop/evaluate high-order consistent LES/FMDF models for RCMs and to use them for better understanding of the flow field in these machines. For non-reacting flows, LES/FMDF of the in-cylinder flow under two conditions are simulated. The first condition involves the fluid flow and heat transfer in an RCM with flat piston. The effect of temperature and heat transfer on the in-cylinder flow is studied. In addition to the flat piston, a crevice piston is considered and the effect of piston geometry on the flow in the cylinder is studied. Reacting flows, with and without spray are simulated with the LES/FMDF and consistency and accuracy of the model is established by comparing the FD with the MC ones.

4.2 Results

Non-reacting and reacting flows, with and without spray, in two RCM configurations are simulated in this chapter. For non-reacting flows, both flat and crevice pistons are considered. The simulation of the reacting flows, with and without spray in the RCM are conducted with the crevice piston. The results obtained by LES/FMDF for non-reacting and reacting flows with and without spray are presented below in three different sections.

4.2.1 Non-reacting flows

Recently, an RCM is built (Fig. 4.1(a)) at Michigan State University (MSU) in the Energy and Automotive Research Laboratory [58]. The MSU RCM is somewhat similar to that considered in Ref. [59]. The geometry is axisymmetric and consists of a simple closed cylinder and a crevice (or a flat) piston. In order to have a uniform temperature distribution in the cylinder, the crevice piston head is used. The stroke and bore of MSUs RCM is 25.4 and 5 cm, respectively and the compression time is about 30 milliseconds. Here, for the simulation of RCM with LES, we use a 4-block grid system. To avoid singularity at centerline, a rectangular H-H ($250 \times 13 \times 13$) block is employed at the center, coupled with an O-H ($250 \times 45 \times 42$) grid outside. For the crevice section, two blocks ($21 \times 5 \times 42$ and $80 \times 16 \times 42$) coupled with the in-cylinder grids are employed. Figure 4.1(a) and (b) show the 3D view of the entire grid and 2D view of the cylinder and the crevice section of the piston. The geometrical parameters and piston movement are similar to those used in MSU RCM experiment. During the flow compression, adaptive grid compression is used, while the number of grids is not changed. Compression begins with a specific initial temperature and pressure. In a previous work [82], simulation of RCM with adiabatic walls was conducted and consistency of LES-FD and FMDF-MC results was established by including the

pressure effect on the FMDF. It was shown that the consistency of the predicted temperatures obtained by the Lagrangian MC method, with those calculated by the FD solution of carrier-gas equations over Eulerian grids is dependent on the inclusion of " $D\langle p \rangle_l / Dt$ " in the FMDF equation. In this work, extensive large-eddy simulations of flows, spray and combustion in the RCM with heat transfer effects are conducted. An important issue in RCMs is to have a uniform temperature distribution at the end of compression. In order to study the effect of piston shape on the temperature field inside the cylinder two types of pistons are considered: I) flat piston, II) crevice piston. To study the effect of heat transfer, the walls are assumed to be isothermic equal to initial gas temperature. In order to implement the isothermic condition in the MC calculations, the FD temperature values in the boundary cells are interpolated to the MC particles located in corresponding cells. For these MC particles, the FMDF energy equation is eliminated, however, particles are still allowed to move according to Eq. (2.34). To include the pressure effect, the total derivative of pressure Dp/Dt , as computed by the filtered Eulerian carrier-gas equations are interpolated and added to the corresponding MC particles in the FMDF similar to that we do in our adiabatic simulations [82].

Two simulations with flat and crevice pistons under conditions used in real experiments [59] are performed. Piston movement and compression time are also identical to the experiment. In the flat piston simulation, the grids which cover the crevice section of piston (green and blue blocks in Fig. 4.1) are excluded from the computation. The working fluid is pure Nitrogen with initial temperature and pressure of 297 K and 0.93 bar, respectively. The compression ratio for the flat piston is 21. In the crevice piston simulation, all grids in Fig. 4.1 are included in the computation. The working fluid, is again pure Nitrogen and the temperature is 297 K, but the pressure is slightly higher at 1.16 bar. The compression ratio for the case with crevice piston is around 17.147. The main purpose of these simulations is to study the effect of piston crevice

in the in-cylinder fluid flow during the compression. Establishing the consistency of the LES-FD and FMDF-MC is also considered. The "time=-30 ms" represents the beginning of compression and "time=0" is the time for the end of compression. 3D iso-levels of temperature at "time=-5ms" for the flat and crevice piston simulations are shown in Fig. 4.2(a) and (b), respectively. For the flat piston case, a large 3D vortical flow structure is generated in front of the piston, which is consistent with experiment. However, this vortical flow does not exist in the crevice piston case.

To better understand study the in-cylinder flow and heat transfer during the compression for the flat piston case, 2D contours of temperature as predicted by the LES-FD and FMDF-MC at different times are shown in Fig. 4.3. With the acceleration of the piston, the boundary layer grows on the walls of cylinder. The radial component of the fluid velocity in the boundary layer at the corner of the piston and the cylinder wall transfer colder fluid in the vicinity of the piston to the cylinder and generates a circulation in the temperature field. By further movement of piston, this circulation zone is moved towards the cylinder center line. The contour plots of the temperature, 15 milliseconds before the termination of compression (Fig. 4.3(a)) clearly show the movement of the generated vortex towards the center of the cylinder. As piston moves further, the generated vortex moves close to the cylinder axis and stay there until the compression ends. Figure 4.3(b) shows the temperature field 5 milliseconds before the end of compression. At the end of compression the circulating flow makes the core of the cylinder colder, while a warmer region forms between the cold flow in the central region and the cold flow near the cylinder wall. This temperature distribution is shown in Figs. 4.3(b) and (c). After termination of compression the temperature starts to be more homogeneous as shown in Fig. 4.3(d). It is clear that the flow and the fluid temperature in the cylinder is not uniform for the case with flat piston. Also the FMDF-MC results with compressibility effect included and with the isothermic wall condition are shown to be consistent with the LES-FD

results.

Similar to the flat piston case, the 2D contours of temperature for the crevice case, as predicted by the LES-FD and FMDF-MC at different times are shown in Fig. 4.4. Acceleration of the piston pushes the in-cylinder perturbations away from piston head toward the cylinder head while the boundary layer formed in the corner of piston and cylinder wall moves into the nozzle-shape crevice. This affects the generation and growth of the boundary layer on the wall of cylinder. Clearly, the radial component of the fluid velocity in the boundary layer at the corner of piston head and cylinder wall in the case with crevice piston is not as large as that in the case with flat piston. Weaker radial velocity generates weaker temperature circulation and more uniform temperature distribution. Figure 4.4(a) shows the temperature contours 15 milliseconds before the end of compression. In comparison with the contours for the case with flat piston (Fig. 4.3(a)) the size of circulation zone is much smaller and its location is farther away from the cylinder axis when a crevice piston is used. In Figs. 4.4(b),(c) and (d) the temperature contours 5 milliseconds before the end of compression, at the end of compression and 5 milliseconds after the end of compression are shown. Again, in comparison with the temperature contours for the case with flat piston (Figs. 4.4(b),(c) and (d)), the in-cylinder flow temperature is much more uniform. Based on these results, one may conclude that with the crevice piston, more uniform temperature distribution in the cylinder may be achieved. Similar to that observed for the flat piston, the FMDF-MC results with the compressibility effect included and isothermic wall condition are shown to be consistent with the LES-FD results. In Figs. 4.5(a) and (b), the in-cylinder temperature predicted by the LES/FMDF along a radial line are compared with the experimental data provided in Ref. [59]. The LES results for the crevice piston are shown to compare well with the experimental data. However, LES results for the flat piston in the colder flow region in the middle of the cylinder is shown to be underpredicted. This can be due

to the isothermic boundaries used in the simulation. In real experiments, the flow in the boundary layer increases several degrees during the compression which is not considered in this simulation.

4.2.2 Reacting flows without spray

Singe-phase reactive flow simulation in the RCM with crevice piston, based on the experimental device built at MSU, is conducted with the LES/FMDF methodology. In this simulation, it is assumed that the initial fluid is a uniform mixture of evaporated ethanol and air with equivalence ratio of 0.5 and initial temperature and pressure of 343 K and 0.6 bar, respectively. Similar to that used in non-reacting flows, isothermal wall condition with wall temperature set to initial gas temperature is used. For simplicity and affordability, a one-step global mechanism is used for ethanol/air combustion [90]. However, more complex kinetics models may be used and will be considered in future studies. Figure 4.6 shows the predicted volume-averaged pressure during the compression and combustion periods and the comparison with the MSUs experimental data. Two pre-exponential values are used with the global chemistry mechanism. The pressure trace with the pre-exponential value given in Ref. [90] is shown with dashed-line and hollow square symbols. The ignition delay is not predicted well in comparison with the experimental data (solid line with circular symbols). However, by multiplying the pre-exponential value by "3", the predicted pressure and ignition delay are found to be in good agreement with the experimental data. These values are shown with the dash-dotted line and triangular symbols. The 2D contours of the temperature in the center plates parallel and perpendicular to the piston as predicted by the FMDF-MC during the auto-ignition of ethanol and flame propagation are shown in Fig. 4.7. Reaction starts in the higher temperature region between the cold boundary layer region and the center of the cylinder (Figs. 4.7(a) and (b)) and propagates toward the center (Fig. 4.7(c)). The prediction of

cold boundary layer and hot central flow region (Figs. 4.7(d)) is consistent with the experimental observation [64, 65, 66]. It is also found that the FMDF-MC temperature predictions are consistent with the LES-FD predictions at all times during the autoignition. In Fig. 4.8(a), LES-FD temperature values at the same locations and times shown in Fig. 4.7(d) are presented. There is a good consistency between the temperature values calculated by the LES-FD and FMDF-MC. Scatter plots of the temperature predicted by the LES-FD and FMDF-MC data (Fig. 4.8(b)) also confirm the high level of correlation between the two subcomponents of the LES-FMDF model.

4.2.3 Reacting flows with spray

Before simulating the spray and combustion in the RCM, the LES/FMDF methodology is used for studying the fuel spray droplets dispersion and evaporation and parameters affecting the fuel mixing in a stagnant environment. The numerical simulations are conducted for conditions close to those considered in experiments performed at Sandia National Laboratory [91]. In these experiments, the fuel spray evaporation and combustion in a closed combustion chamber are studied. Figure 4.9(a) and (b) show a schematic view of the experimental set up and computational domain with sample fuel droplets. The average size of the combustions chamber is 105mm. The gas temperature, density and oxygen concentration vary from 450 K to 1300 K, 3 to 60 kg/m^3 , and 0% to 21%, respectively with the help of an intake valve. The fuel injector is located in one side of the chamber, and the nozzle diameter ranges from 0.05 to 0.5 mm with the fuel injection pressures varying between 40 to 200 MPa. The effect of ambient temperature, density, injector pressure and nozzle diameter on the liquid penetration in non-reacting cases and the flame lift-off in reacting cases were studied by our LES/FMDF model. The liquid penetration depth is the maximum extent of liquid-phase spray penetration during the injection and the flame lift-off is

the axial distance from the injector to the location of high-temperature reaction zone. The numerical simulation is conducted via LES together with some models for the droplet breakup. A cubic computational domain with uniform grids ($dx=dy=dz=2$ mm, see Fig. 4.9(b)) is employed. The initial gas conditions are set based on the experimental conditions and is uniform. The fuel droplets are injected into the domain from the center point of the right face. The initial droplet velocity is calculated from the Bernoulli equation as $V = C\sqrt{\frac{2\Delta P_{inj}}{\rho_{fuel}}}$, where the coefficient C varies from 0.7 to 1.0. The initial droplet diameters are calculated by using the nozzle diameter and its area-contraction coefficient. Spray droplet break-up was performed by the hybrid Kelvin-Helmholtz (KH)/Rayleigh-Taylor (RT) model [92, 93, 94]. It is assumed that, the size of initial droplets or parent blobs are equal to the injector nozzle diameter, this rough assumption is then corrected by the KH primary break-up model. After this stage the particles undergo a secondary break-up by the RT accelerative instability model. LES results and experimental data for liquid penetration in the non-reacting cases at different ambient densities and temperatures are shown in Fig. 4.10(a). In these simulations, the fuel temperature, the injector pressure and the nozzle diameter are fixed at 436K, 138 MPa and 246 mm, respectively, consistent with the experiment. The oxygen concentration is zero. In Figure 4.10(a), the solid and dashed lines represent the (isothermal) experimental data and the LES results, respectively. Evidently, the liquid jet penetration decreases by increasing the ambient temperature or density. This decrease in penetration is significant at low temperatures or densities, but it is small at high temperatures or densities. The numerical results are shown to be consistent with the experiment. The effect of injection pressure on the liquid penetration in non-reacting cases is shown in Figure 4.10(b). In these simulations/experiments, the fuel temperature and nozzle diameter are fixed at 436K and 246 mm. Again the oxygen concentration is zero. By increasing the injection pressure, while keeping the ambient temperature and density constant, the liquid penetration is shown to remain

nearly constant. Again, the numerical results are consistent with the experiment and show very similar trends, despite some quantitative differences. Figure 4.10(c) shows the effect of injector nozzle diameter on the liquid jet penetration in non-reacting conditions. In these simulations/experiments, the fuel temperature and the injector pressure are fixed at 436K and 138 MPa, respectively and the Oxygen concentration zero. Similar to Figures 4.10(a) and 4.10(b), solid and dashed lines represent experimental and numerical data. Unlike the results obtained for varying injector pressure, by increasing the injector diameter, while keeping the ambient temperature and density constant, the liquid jet penetration increases. However, the rate of change in the penetration depth is much higher at low temperatures or densities as opposed to that in high temperatures or densities. Again, the numerical results are consistent with the experiment and show very similar trends, despite some small quantitative differences.

The effect of initial gas temperature on the flame lift-off in reacting cases is shown in Fig. 4.10(d). In the simulations/experiment shown in this figure, the fuel temperature, the injector pressure and the nozzle diameter are fixed at 373K, 150 MPa and 100 mm. In The initial oxygen concentration is 21%. Figure 4.10(d) shows that by increasing the initial ambient gas temperature, the flame lift-off decreases. This is expected as combustion becomes more effective when reactants temperature increase. Again, the experimental and numerical results are consistent.

The injection of fuel at the end of compression stroke in the MSU's RCM is performed at different compression ratios. For the compression ratio of 17.147, the injector is located in the mid-distance between the piston and the cylinder head. We have simulated reacting and non-reacting flows with spray inside the RCM with the LES/FMDF for four different spray conditions similar to the ones used in Sandia experiments. The initial temperature and pressure are 423 K and 1.38 bar, respectively. Using these initial conditions and crevice piston, the final temperature and

density in central region of the cylinder reaches to $950 \pm 30K$ and $13.8 \pm 1.0Kg/m^3$. There are some differences in the thermodynamic conditions in comparison to the experiment. In the experiments, the stagnant temperature and density are $1000K$ and $14.8Kg/m^3$. Figure 4.11 shows the 2D contour of the gas temperature before the injection in two center line plates. The gas temperature in the central region of the cylinder is almost uniform. Four experimental flow conditions, (refer to as case 1-4 in Table 4.1), are simulated. The first three cases are all non-reacting. Figure 4.12 shows the 3D iso-levels and 2D contours of the temperature inside the RCM together with the injected fuel droplets for case 1. In the Sandia experiment [91], injection continues for about 2 msec. We use similar injection features in our RCM simulation.

Table 4.1: Four spray experimental conditions used in the RCM. For all cases, gas phase temperature and density are $1000K$ and $14.8Kg/m^3$, respectively.

Case #	Nozzle Dia. μm	Fuel Type	Fuel Temp. K	O_2 %	penetration		lift-off	
					Exp.	LES	Exp.	LES
1	246	n-Hexadecane	436	0	31.6	31.3	-	
2	100	n-Hexadecane	436	0	13.4	14.4	-	
3	100	n-Heptane	373	0	9.2	9.3	-	
4	100	n-Heptane	373	21	-		12.2	17.0

The 2D contours of the evaporated fuel mass fraction and temperature as predicted by the LES-FD and FMDF-MC for the cases 1, 2, 3 and 4 are shown in Figs. 4.13(a), (b), (c) and (d), respectively. The liquid droplets with the values of penetration and flame lift-off are also shown in comparison with the experiment. In cases 1 and 2, two different injector diameters of 246 and $100 \mu m$ are used with other injection and thermodynamic conditions to be identical. Similar to the Sandia's experiment in stagnant environment, the liquid penetration decreases as the injector diameter decreases. The predicted liquid penetrations for cases 1 and 2 are 30.3 and 13.1 mm, which are close to the experimental values (31.6 and 13.4). In case 3, n-Heptane is injected in the cylinder with different injection pressures and fuel temperatures. The shorter

penetration length, compared to case 2, is predicted well with the LES/FMDF. For the cases 1, 2 and 3, the LES-FD and FMDF-MC results for the deficit in the gas temperature and the evaporated fuel mass fraction are also shown to be consistent (Figs. 4.13(a), (b) and (c)). The reacting spray is simulated with conditions used in case 3 with 21% oxygen. The 2D contours of LES-FD and FMDF-MC temperatures and the fuel mass fraction plus spray droplets are shown in Fig. 4.13(d). The calculated flame lift-off is about 12.2 mm, which is lower than the experimental value of 17 mm. The underprediction can be due to simple chemical kinetics model or some differences in the initial conditions. However, the predicted LES-FD and FMDF-MC flame temperatures and fuel mass fractions remain consistent. The scatter plots of temperature, obtained from LES-FD and FMDF-MC data before and after the reaction, for the case 4 in Fig. 4.14 also show high level of correlation between the LES-FD and FMDF-MC values.

4.3 Conclusions

Large-eddy simulations (LES) of the reacting and non-reacting turbulent flows in a rapid compression machine (RCM) with and without spray are performed with high-order numerical schemes. Spray and combustion simulations are conducted with recently developed probability density function based two-phase subgrid combustion model, termed filtered mass density function (FMDF) and its hybrid finite difference-Monte Carlo (FD-MC) method. Fluid flow and heat transfer in the cylinder are studied with a flat and a crevice piston. The isothermal condition in the MC calculations is achieved by interpolating the FD temperature values in the boundary cells to the MC particles located in corresponding cells and eliminating the FMDF energy equations. To include the pressure effect, the calculated total derivative of pressure " Dp/Dt " by the filtered Eulerian carrier-gas equations are interpolated and added to

the corresponding MC particles. It is found that LES-FD and FMDF-MC predicted values of temperature are consistent during the compression and combustion. Also, it is shown that the in-cylinder temperature values are more uniform when the crevice piston is used. The two-phase LES/FMDF methodology is also used to study the fuel spray characteristics and parameters affecting the fuel mixing in a stagnant environment and inside the RCM. The non-reacting results indicate that by increasing the initial ambient gas temperature and density the liquid jet penetration decreases. However, by increasing the injector nozzle diameter the penetration depth becomes longer. The injector pressure does not seem to have a significant effect on the penetration length. For the reacting sprays, it is shown that by increasing the gas phase temperature the flame lift-off decreases. For both non-reacting and reacting cases, the numerical results for liquid penetration and flame lift-off are shown to be in good agreement with experimental data. Some under-prediction in the flame lift-off can be attributed to the one-step global chemical kinetics mechanism or initial conditions. For the all spray simulations in the RCM, the temperature and evaporated fuel mass fraction statistics calculated from the FD and MC components of the hybrid solver are in good agreement with each other. Consistency of the predicted values by the two model shows the accuracy and reliability of the hybrid two-phase compressible LES/FMDF methodology.

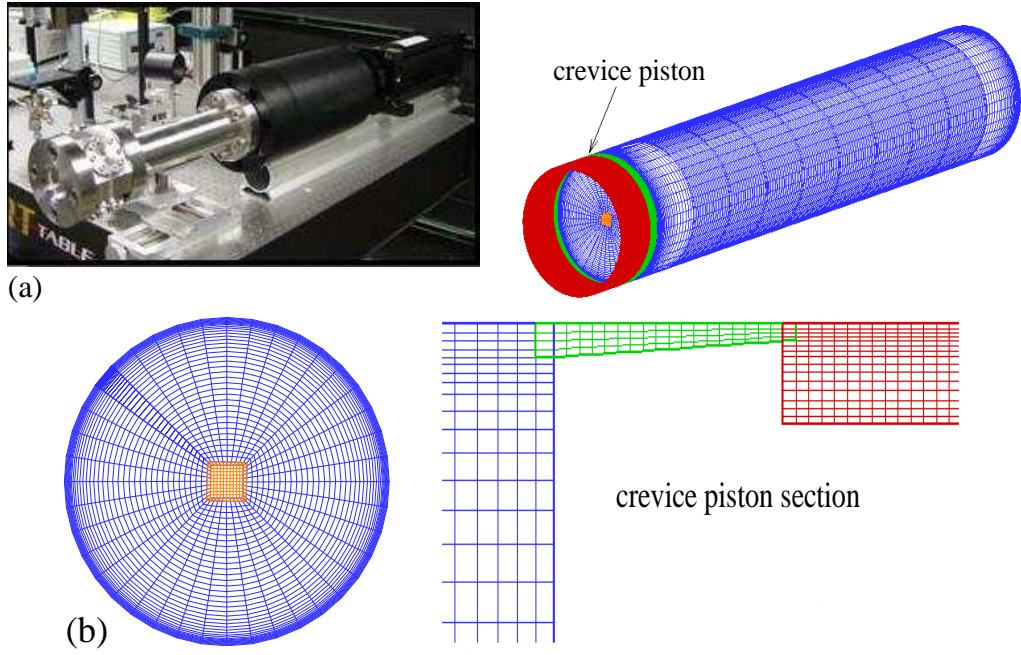


Figure 4.1: (a) Experimental set-up of the rapid compression machine (RCM) [58] and 3-dimensional view of the 4-block grid used for the RCM simulation. (b) 2-dimensional views of the grids employed in the cylinder part and crevice section.

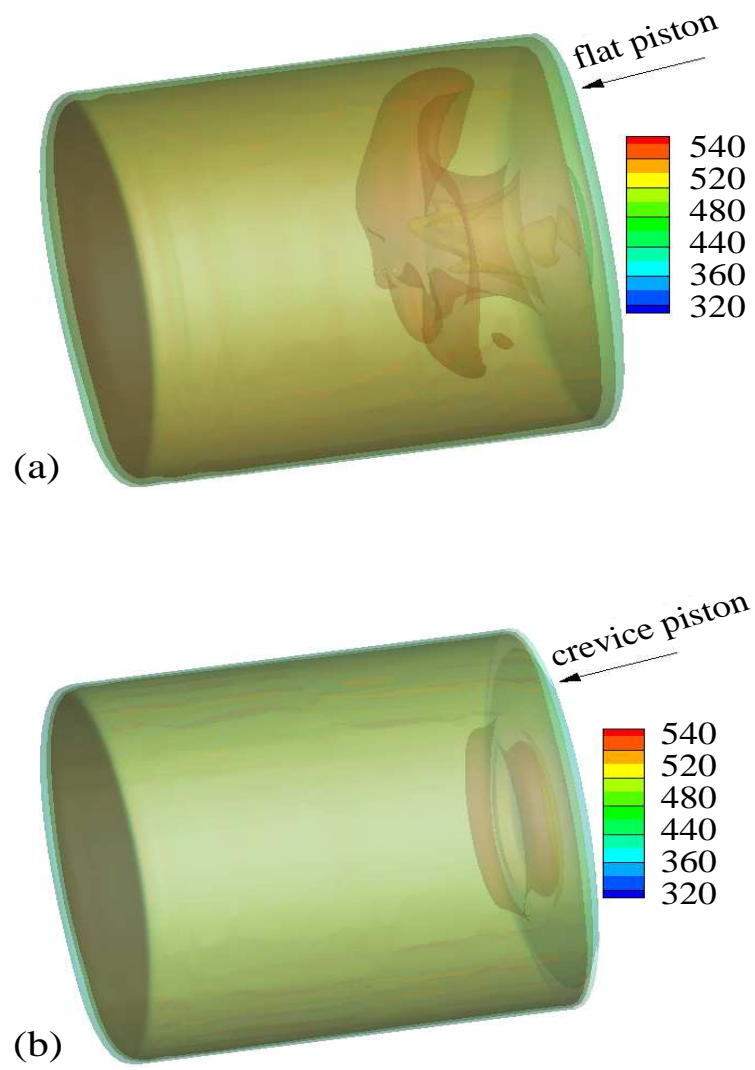


Figure 4.2: Iso-levels of temperature at -5 msec. for (a) flat and (b) crevice piston.

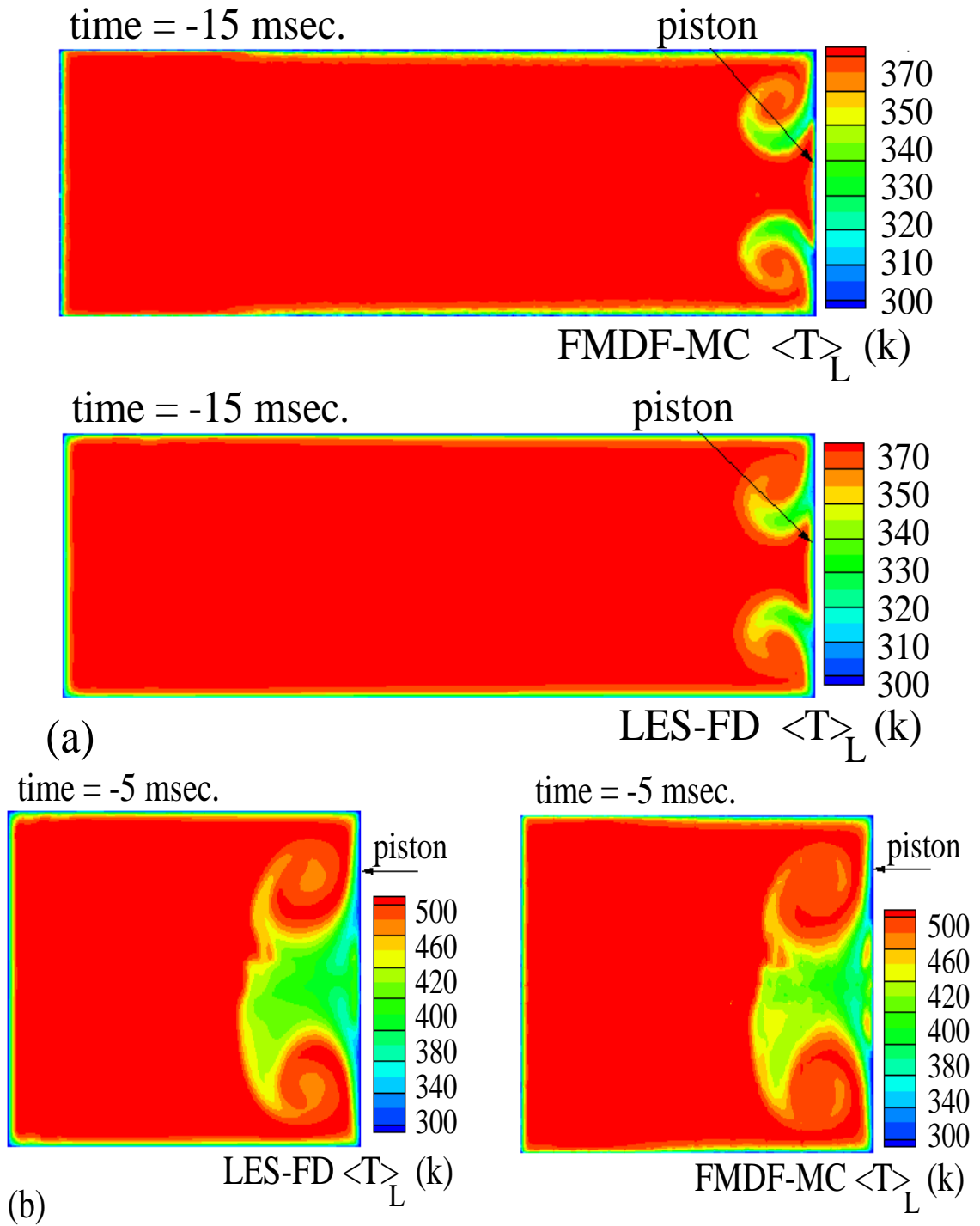


Figure 4.3: 2D temperature contour plots, at (a) -15, (b) -5, (c) 0 and (d) +5 milliseconds for the flat piston as predicted by the LES-FD and FMDF-MC.

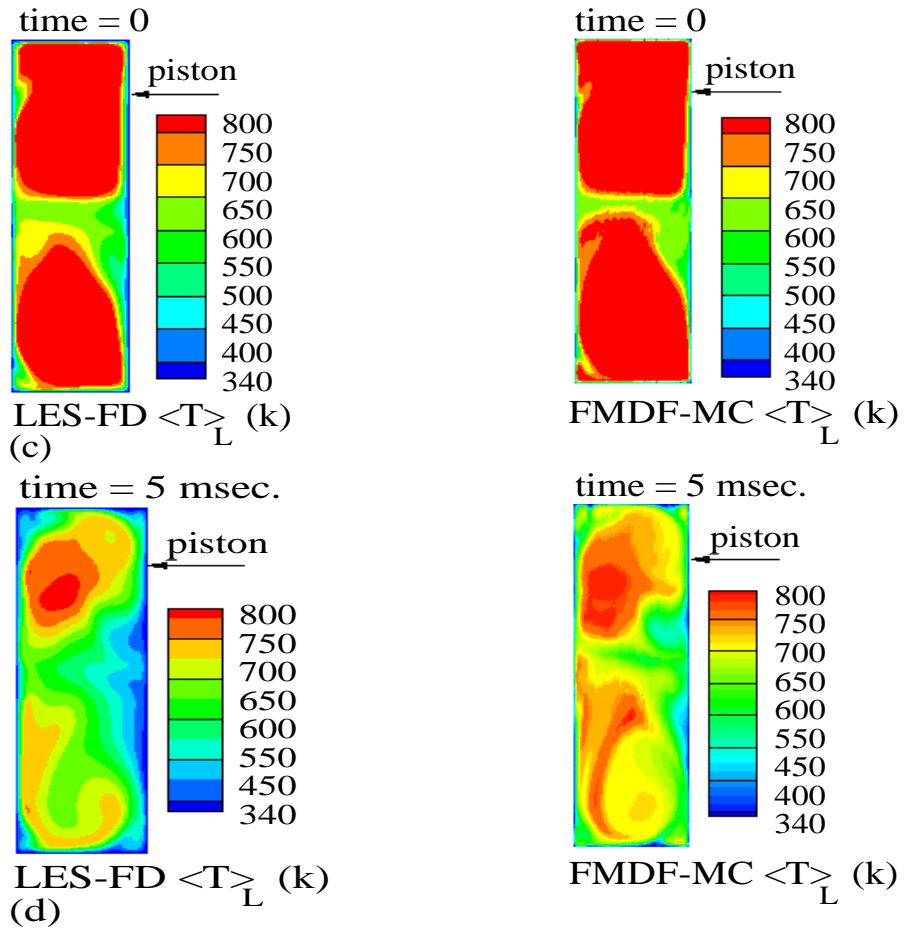


Figure 4.3 continued.

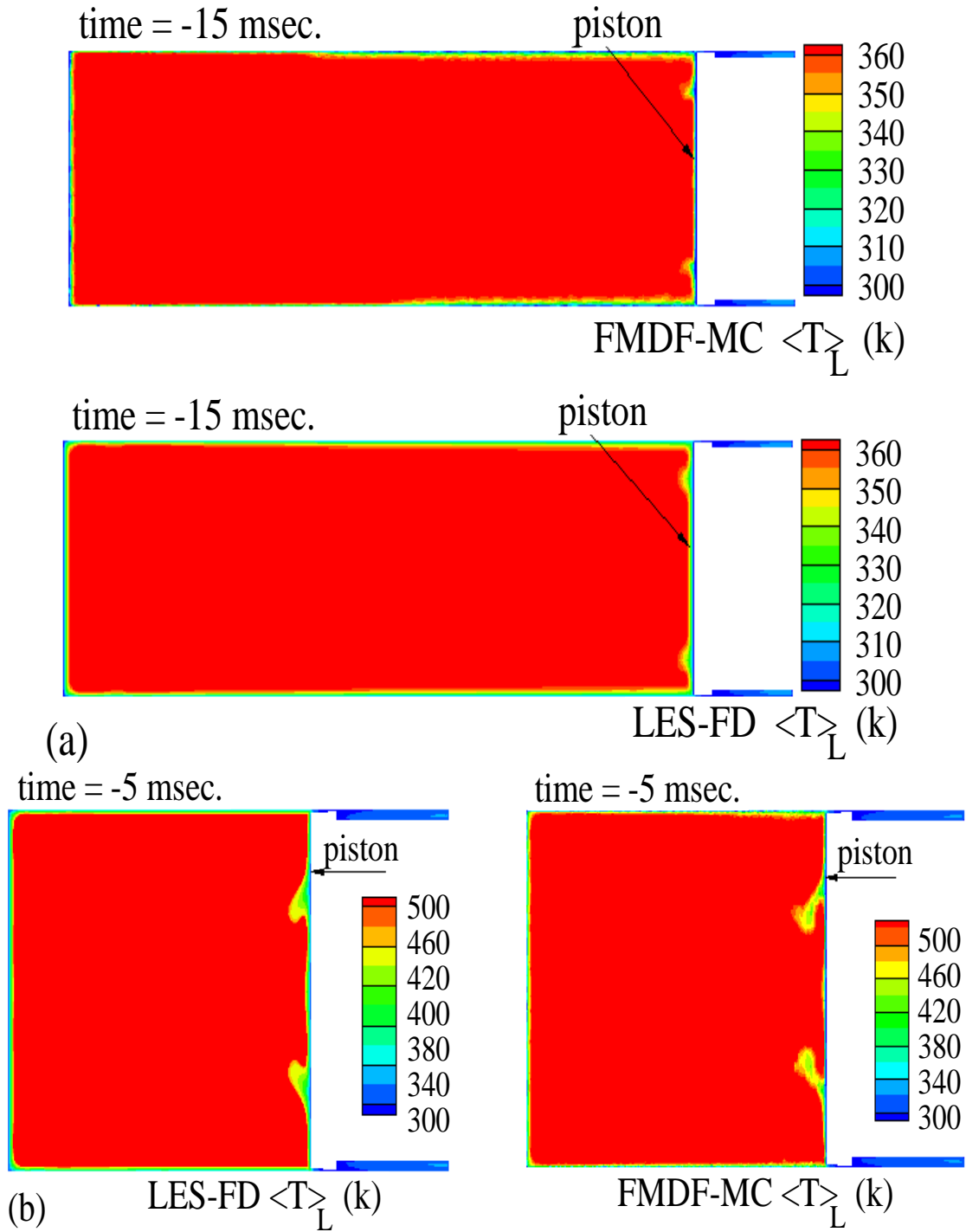
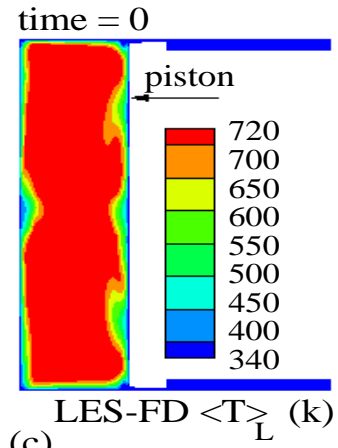
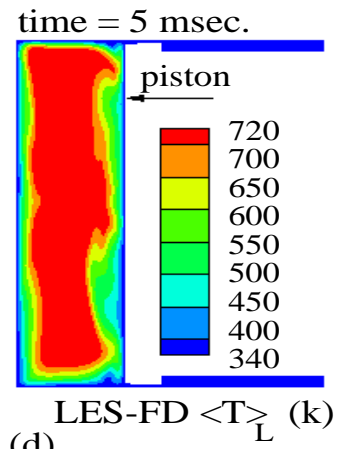


Figure 4.4: 2D temperature contour plots, at (a) -15, (b) -5, (c) 0 and (d) +5 milliseconds for the crevice piston as predicted by the LES-FD and FMDF-MC.



(c)



(d)

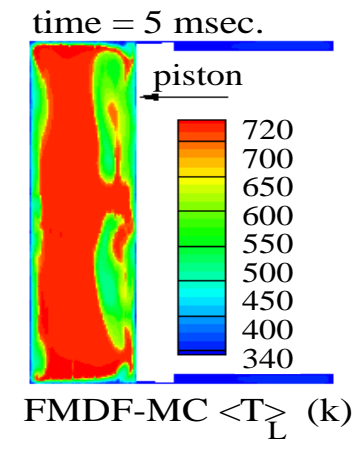
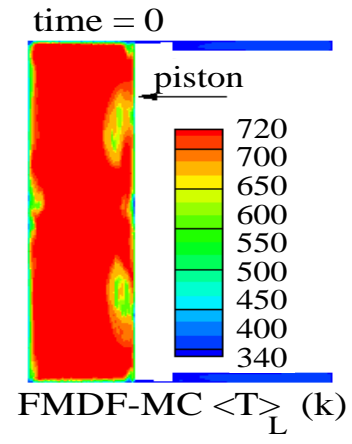


Figure 4.4 continued.

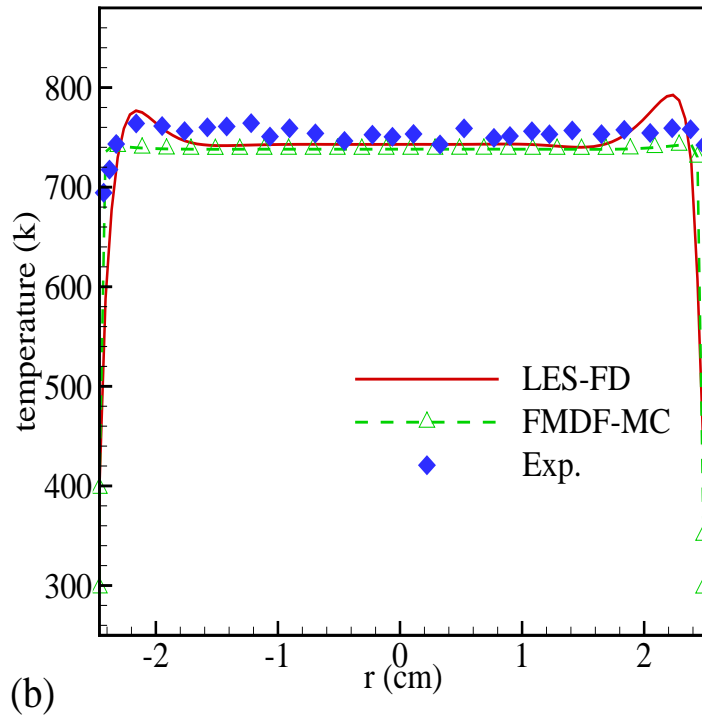
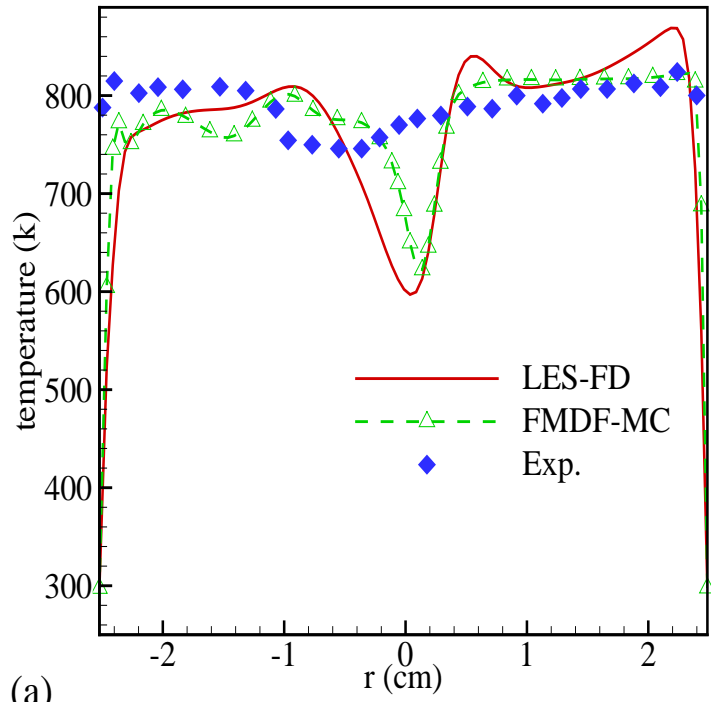


Figure 4.5: Predicted temperature values along a radial line in the central plane and comparison with the experimental data for (a) flat and (b) crevice piston.

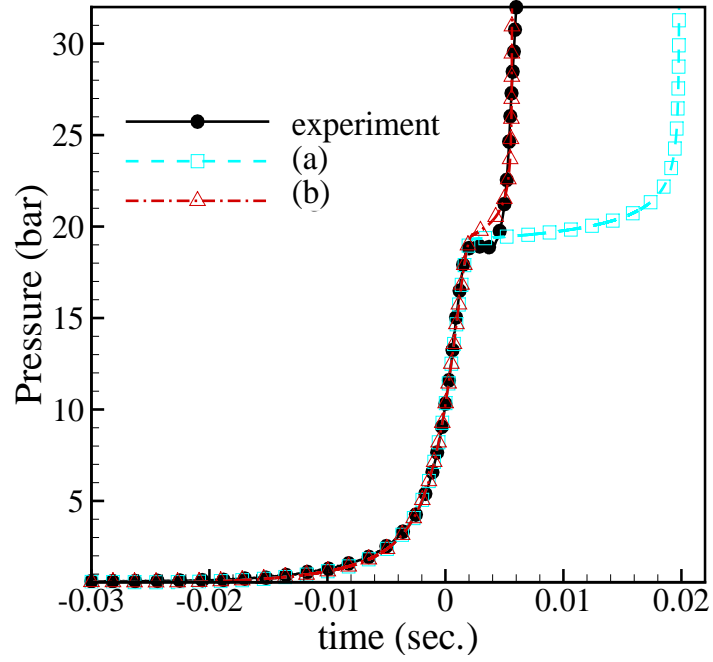


Figure 4.6: Predicted Volume averaged pressure during compression and combustion for two cases of (a) and (b) and compared with the experimental data. (a): simulation with the pre-exponential value provided in Ref. [90] and (b): with pre-exponential value 3 times larger than (a).

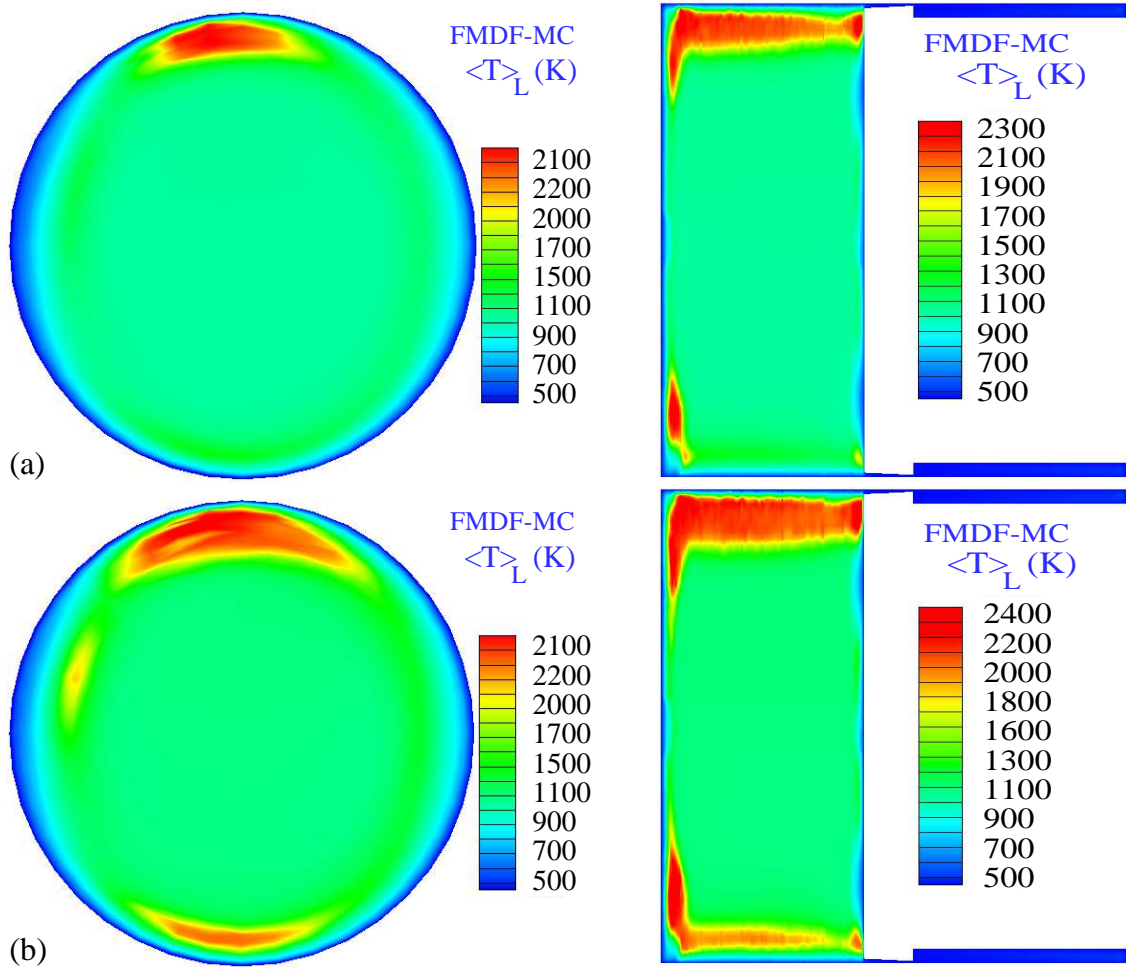


Figure 4.7: 2D contours of FMDF-MC temperature in two planes parallel and perpendicular to the piston during the autoignition and the flame propagation of ethanol for the crevice piston.

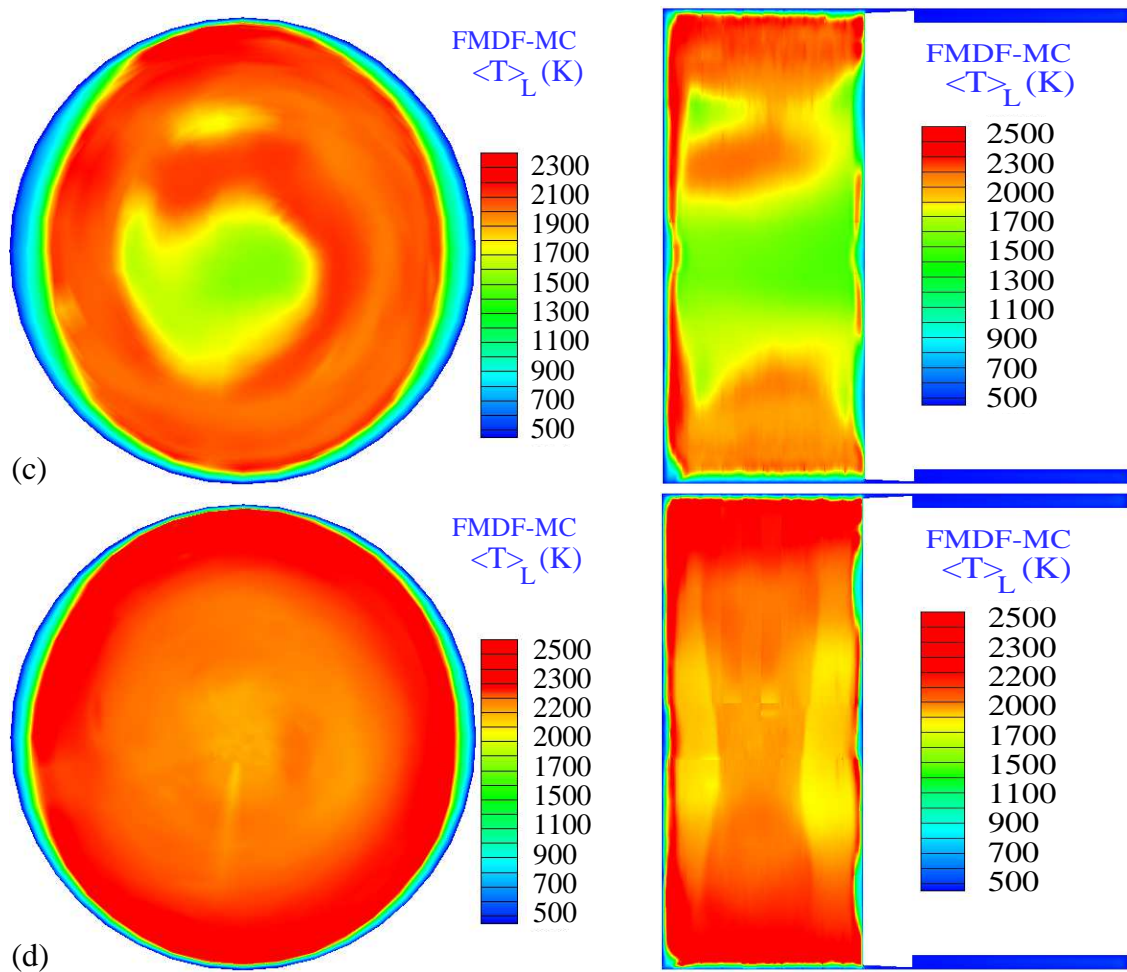


Figure 4.7 continued.

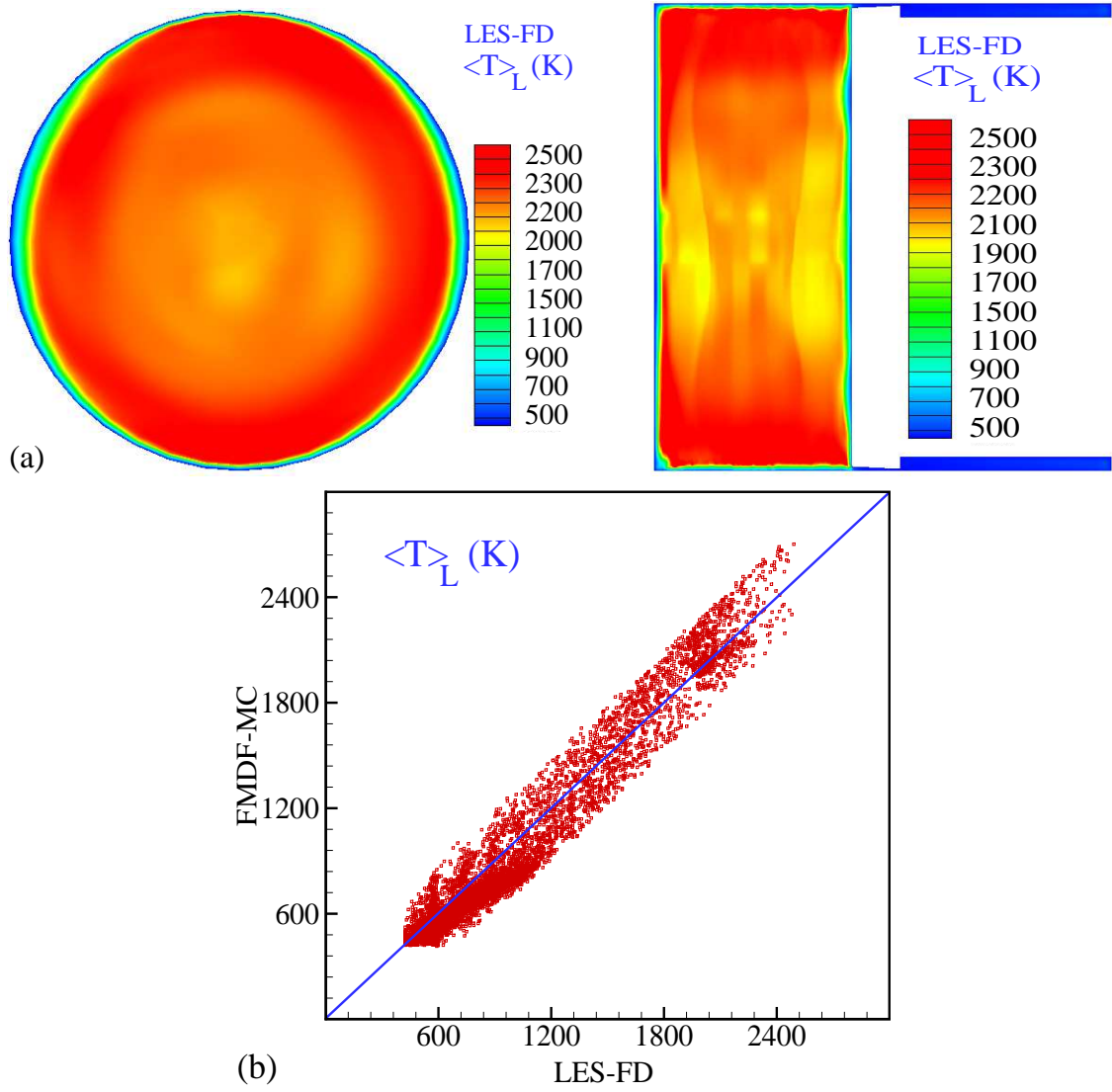


Figure 4.8: (a) 2D contours of LES-FD temperature at same time shown in Fig. 4.7(d). (b) Scatter plots of LES-FD and FMDF-MC temperatures.

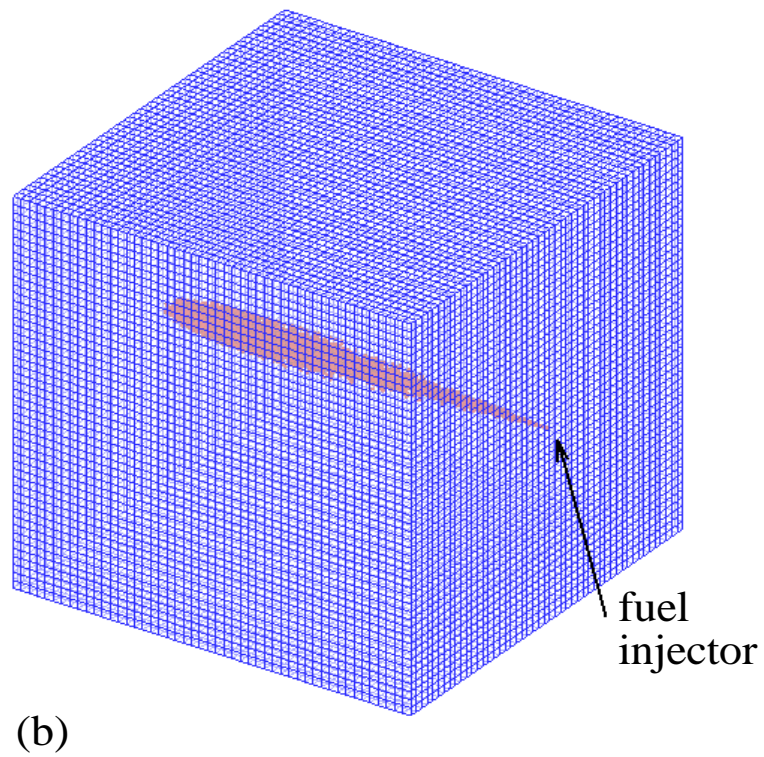
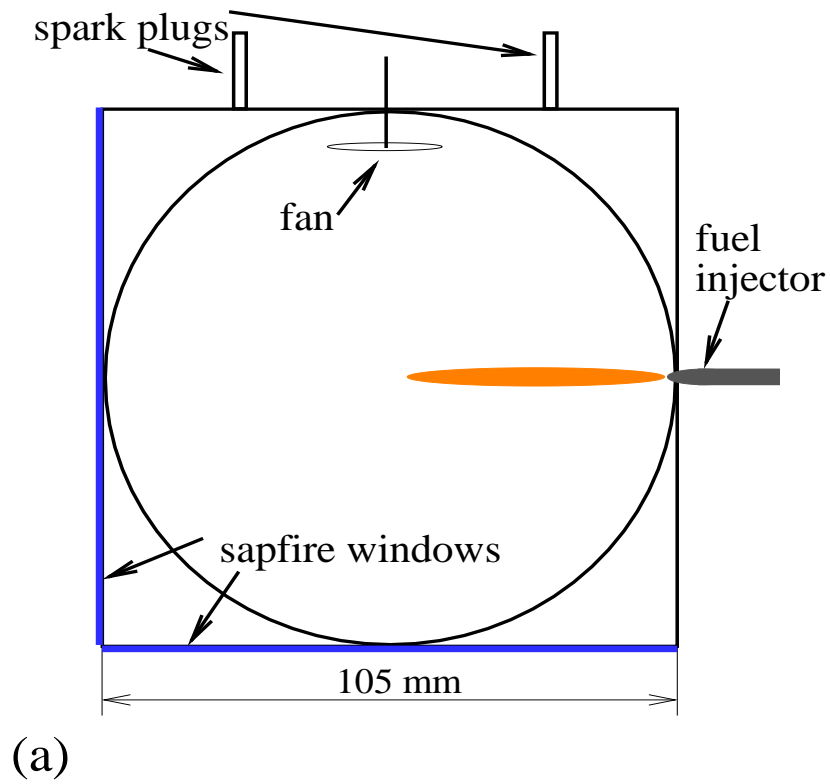


Figure 4.9: (a) Schematic cross section of the Sandia combustion vessel, (b) 3D view of computational domain and fuel particles.

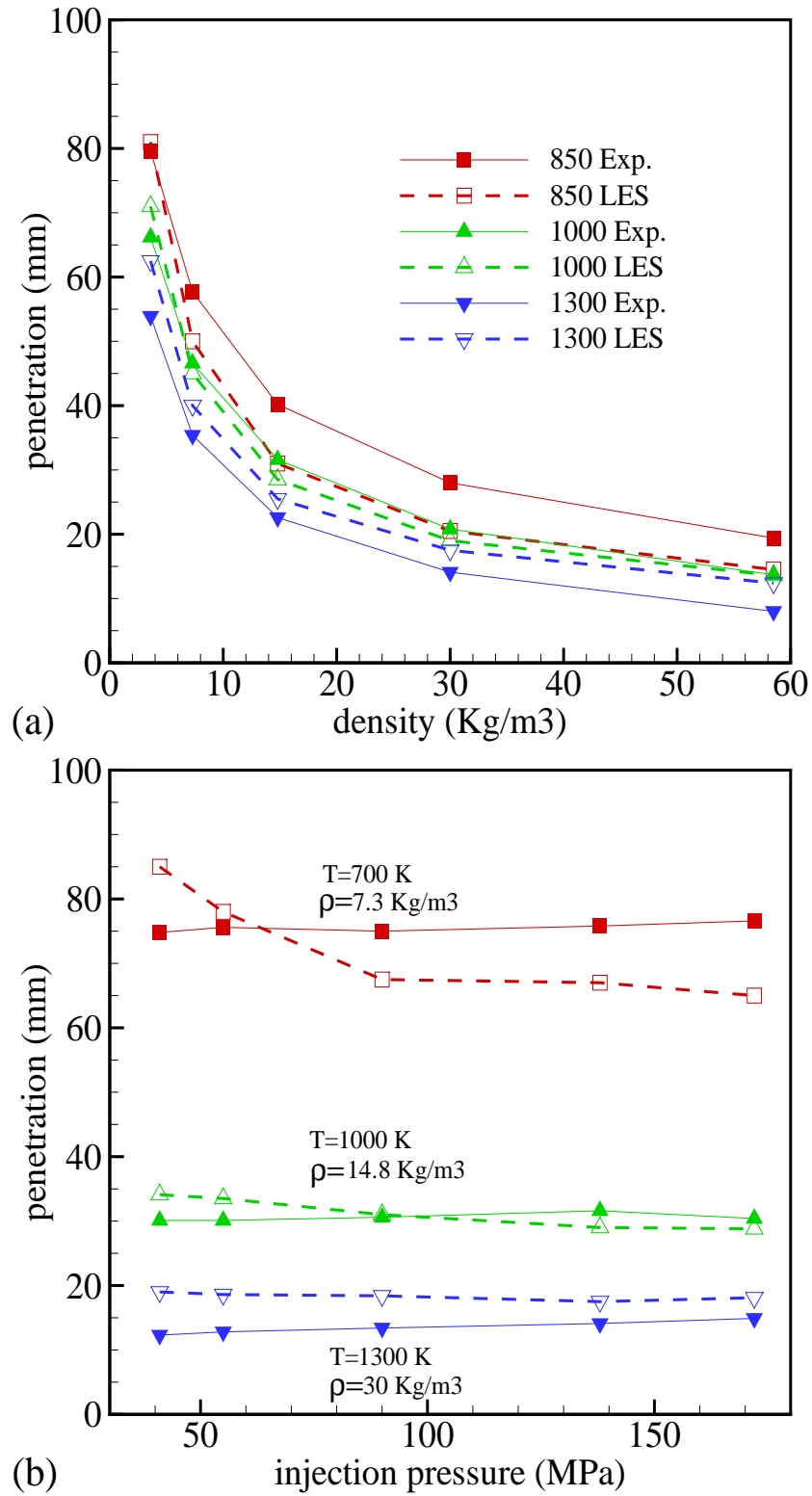


Figure 4.10: Liquid penetration depth at different (a) ambient gas densities or temperatures, (b) injection pressures and (c) injection diameters. (d) Flame lift-off at different ambient temperatures.

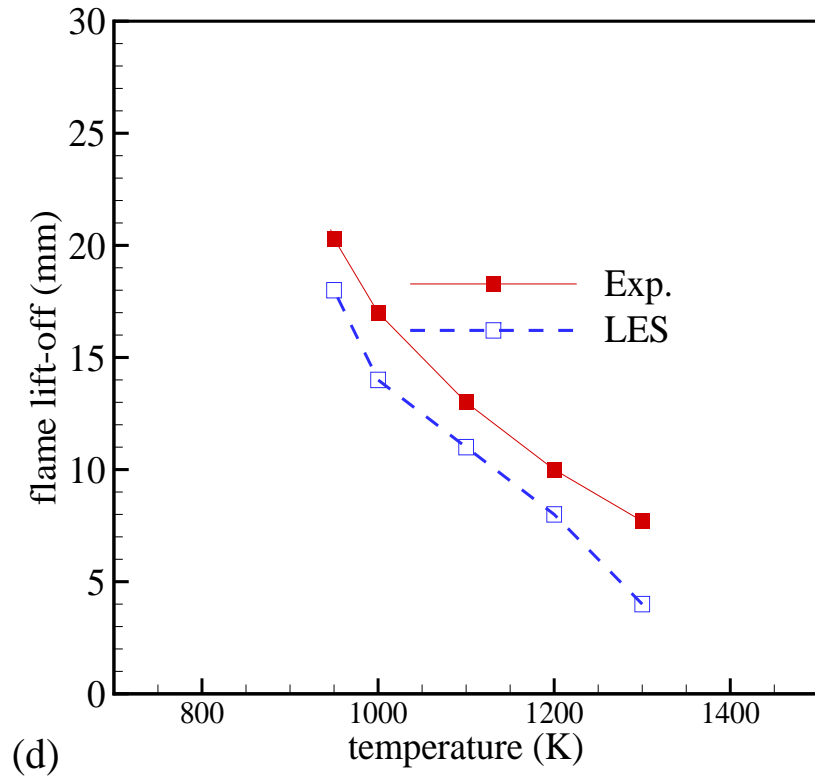
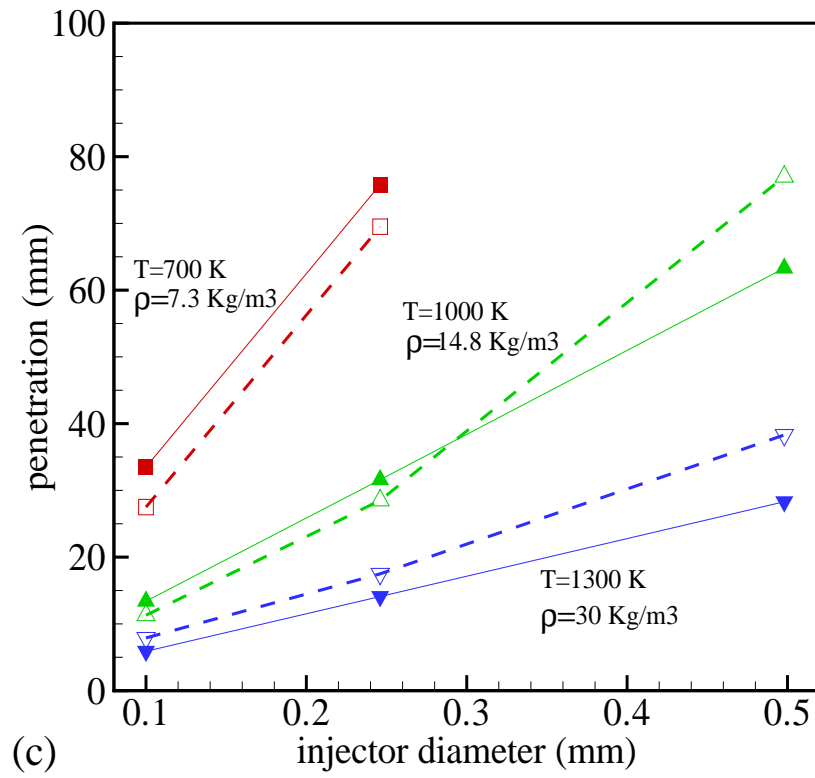


Figure 4.10 continued.

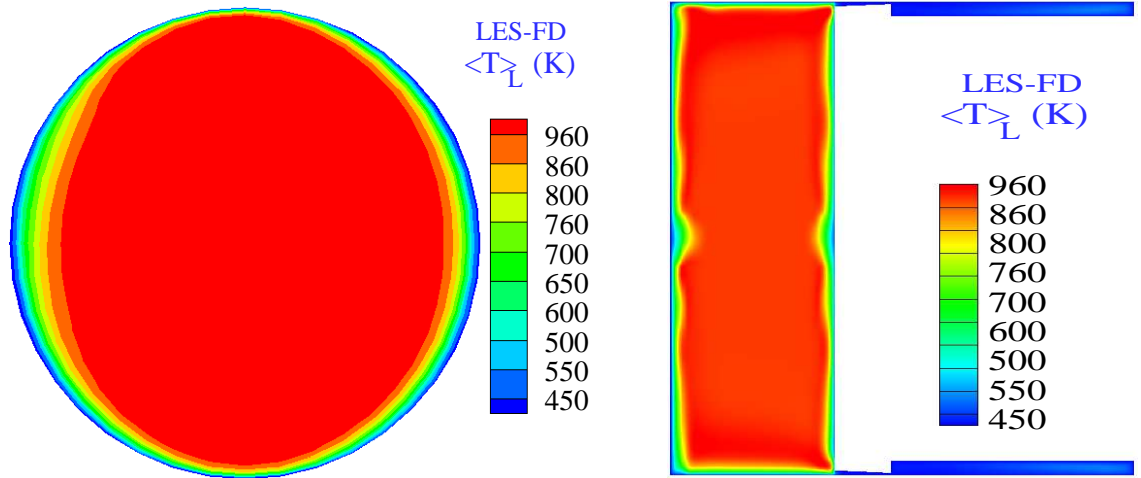


Figure 4.11: 2D contours plots of temperature in two planes parallel and perpendicular to the piston at the end of compression and before the fuel injection.

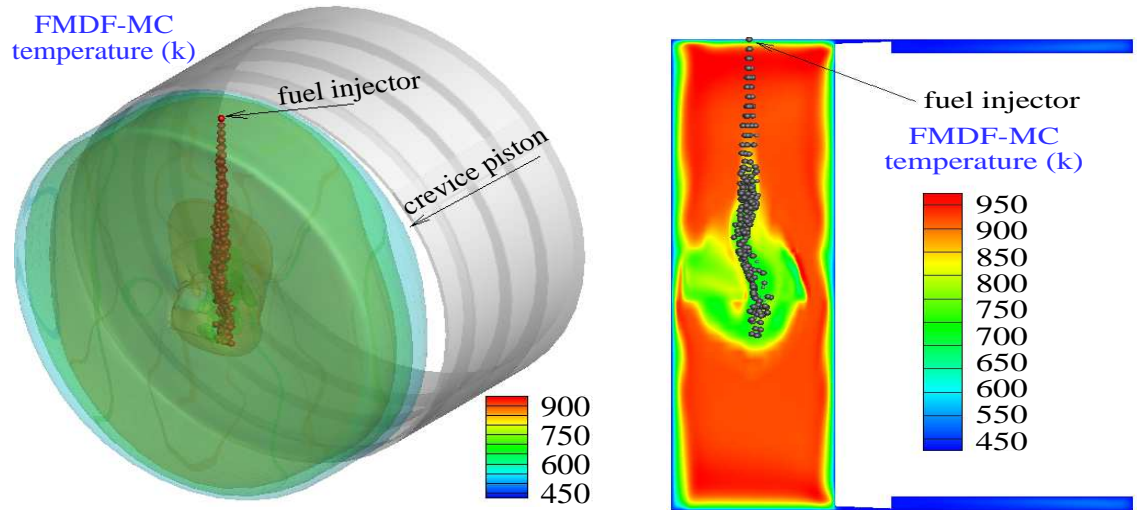


Figure 4.12: Iso-levels and contours of temperature with fuel droplets during the injection for case 1 described in Table 4.1.

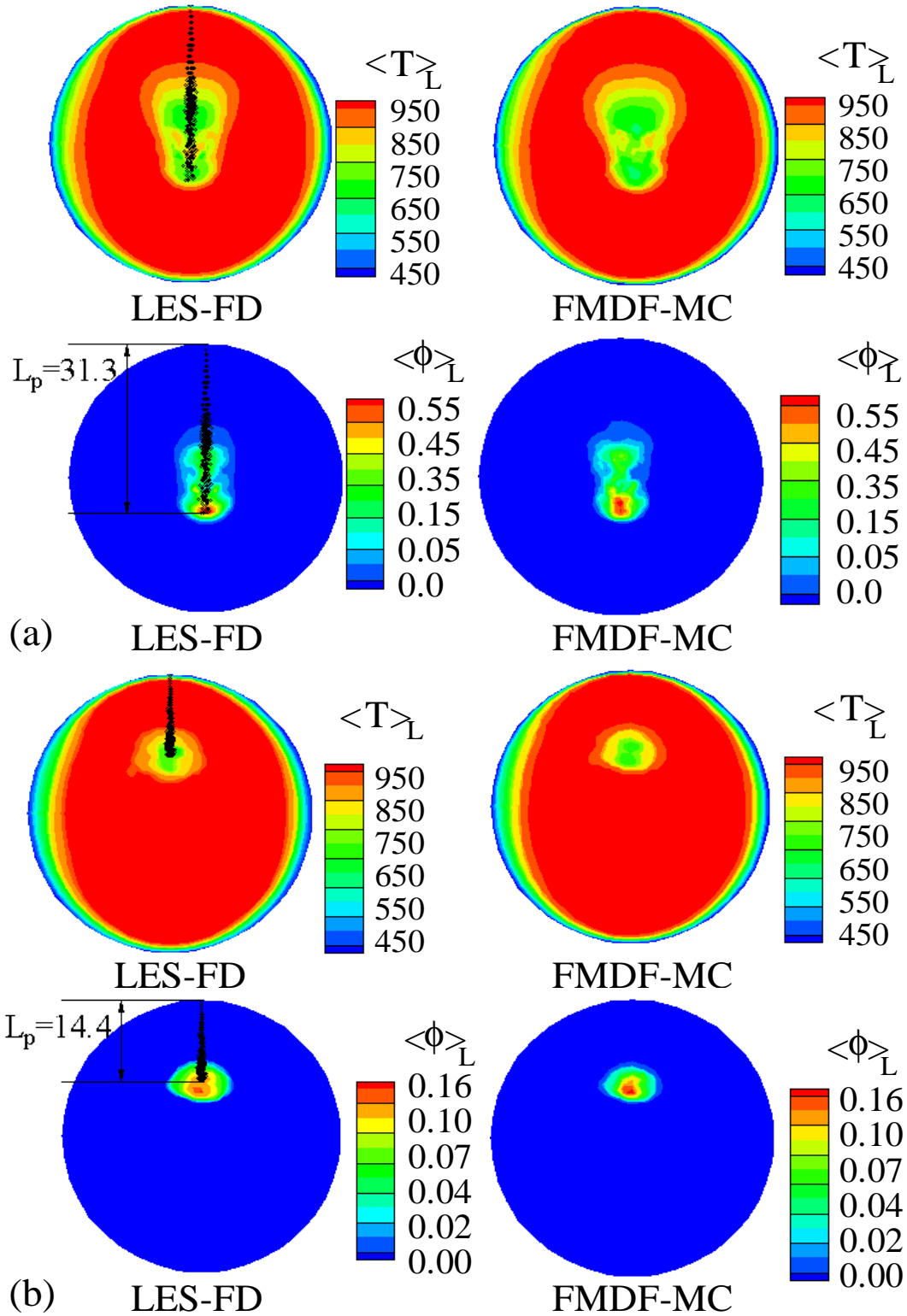


Figure 4.13: Evaporated fuel mass fraction and temperature contours as predicted by the LES-FD and FMDF-MC for (a) case 1, (b) case 2, (c) case 3 and (d) case 4 described in Table 4.1. Predicted liquid penetration and flame lift-off are also indicated.

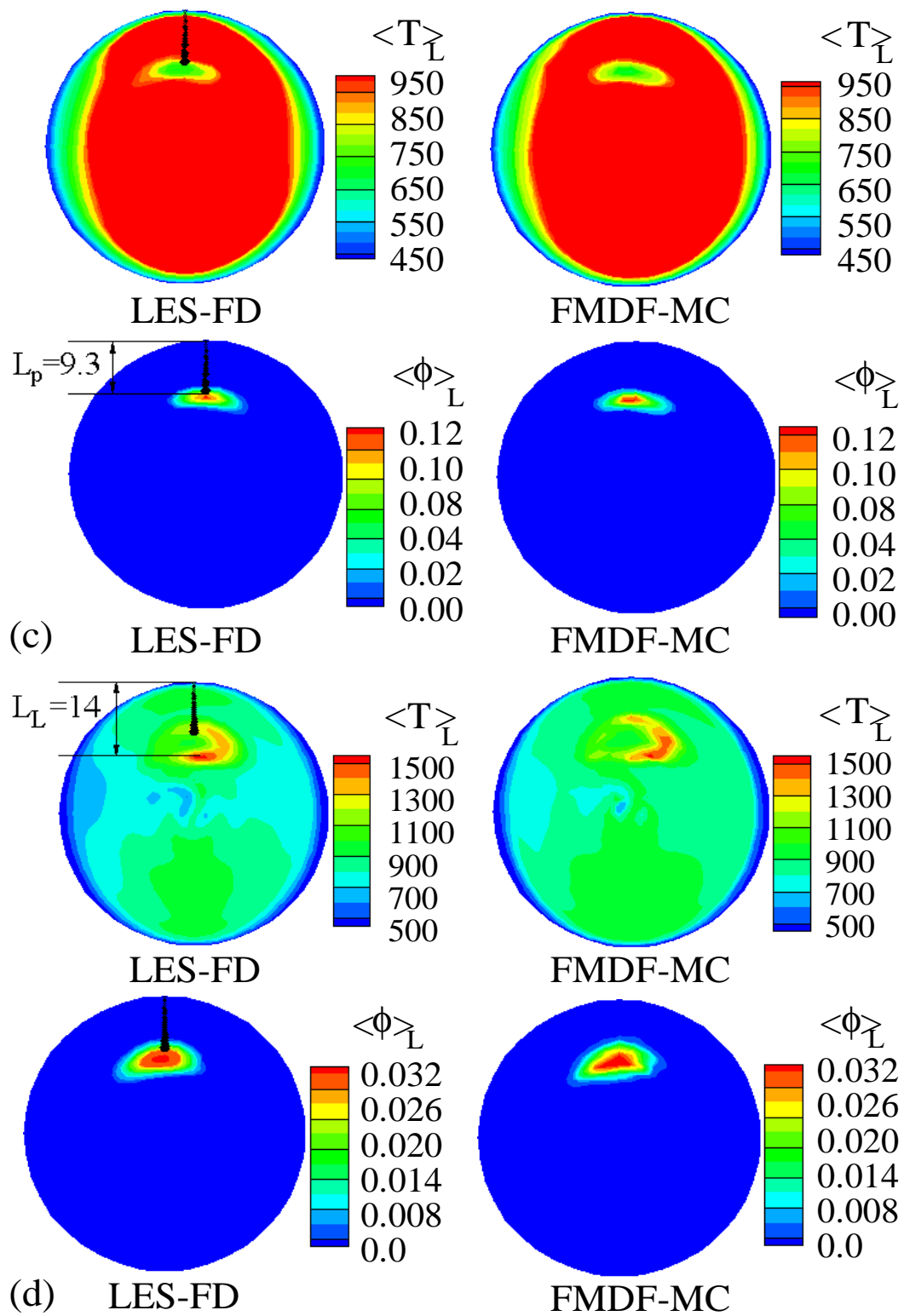
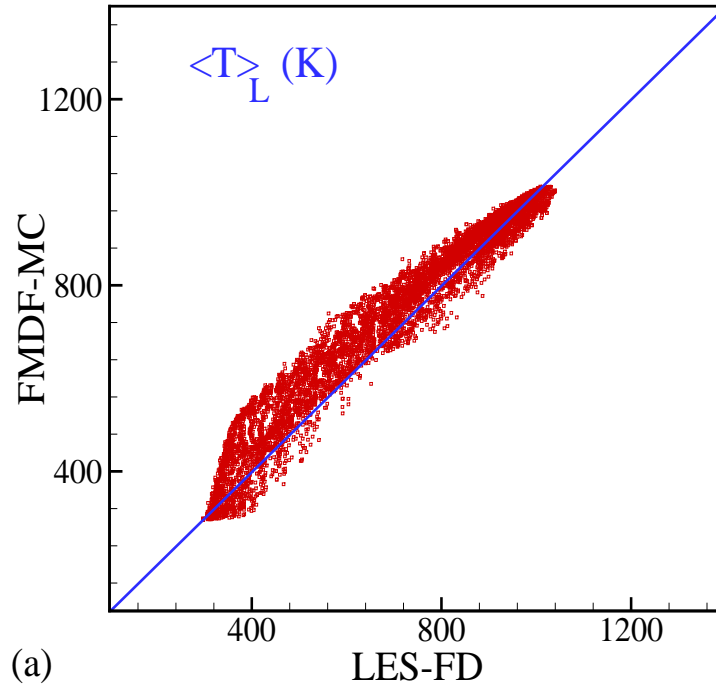
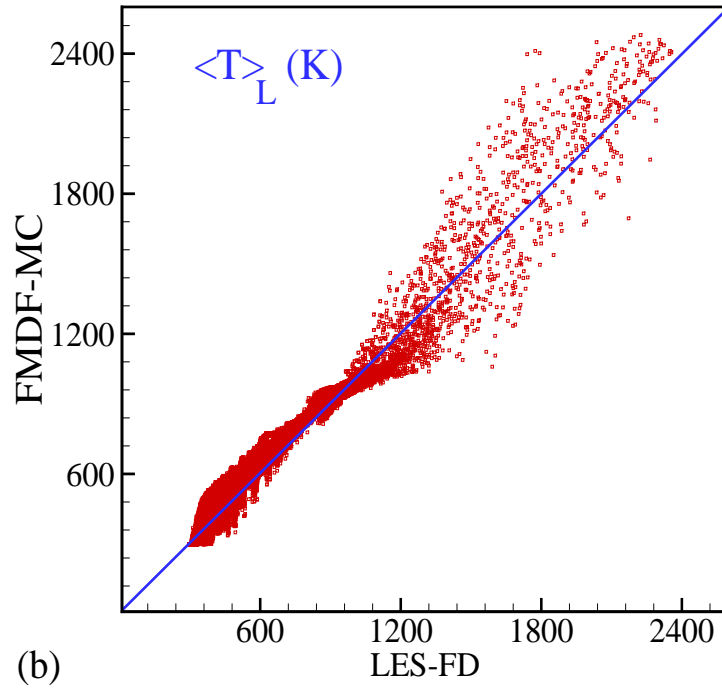


Figure 4.13 continued.



(a)



(b)

Figure 4.14: Scatter plots of LES-FD and FMDF-MC temperatures for case 4, (a) before reaction and (b) after reaction.

Chapter 5

LES of turbulent flow and spray combustion in IC engines

5.1 Introduction

Most of numerical techniques used for the in-cylinder turbulent flow simulations have traditionally been based on the Reynolds-averaged Navier-Stokes (RANS) models. RANS models calculate mean flow only and are not able to predict the CCV. They also have some limitations in predicting the highly unsteady three-dimensional fluid motions in IC engines [95]. About 30 years ago, Reynolds [96] suggested that the models based on spatial filtering is the best approach and should be used for in-cylinder flow/combustion calculations. However, it was not until 12 years after Reynolds suggestion that Naitoh et al. [97] reported the first application of large-eddy simulation (LES) to in-cylinder flows. In their simulations, Naitoh et al. used a first-order Euler scheme for time differencing, a third-order upwind scheme for convective terms, and a second-order central differencing for other terms. The computed subgrid-scale (SGS) turbulence intensity was reported to be roughly 50 per cent of the total turbulence intensity, indicating that the grid resolution was not sufficient for LES. Despite the

limitations of their simulations, Naitoh et al. were able to capture the dynamics of large coherent structures in the cylinder. Other LES of in-cylinder flows have been reported by Haworth et al. [72]. Their simulations were performed using the Node-Centered Unstructured Topology, Parallel Implicit Advection (NO-UTOPIA [98]) scheme, which is at best second-order accurate in time and space. The standard Smagorinsky model [6] was used for the SGS stress. The simulated "engine" geometry was relatively simple, composed of an axisymmetric piston-cylinder assembly with a non-moving central valve and a low piston speed of 200 rpm. Comparison was made with the Laser Doppler Anemometry (LDA) experimental data of Morse et al. [99]. In another work, Haworth [71] used LES with the boundary body force method [100] and different SGS stress models to simulate the incompressible velocity field in a two-valve Pancake-Chamber motored four stroke engine and Morse et al. experiment [99] with a 2nd order finite-difference method. Verzicco et al. [73, 70] also used the boundary body force method for LES of Morse et al. experiment [99] at different Reynolds numbers. The reported LES results are shown to be comparable to those obtained by the RANS model. The unsteady mixing of liquid spray in a direct injection engine was simulated by Sone et al. [76] with the KIVA-3V software [101] and a one-equation linear-eddy SGS model [102]. The non-reacting results obtained by the LES were found to be comparable with the experimental data. Lee et al. [75] used the same SGS stress model for LES of flow in a diesel engine. In another study by Lee et al. [103], a probability density function (PDF) combustion model and the KIVA-3V were used to simulate the combustion process in Diesel engines. It is reported that the model is able to predict the major features of Diesel combustion, including the ignition delay, premixed burn spike, and the diffusion burnout. Thobois et al. [78] performed LES of flow around a poppet valve [104] and in a real engine geometry using cell-vertex finite-volume method and Lax-Wendroff central space differencing. Dugue et al. [79] used Star-CD [105] software to study the CCV in an IC engine.

They simulated several cycles via RANS and LES, and showed that the predicted volume-averaged turbulent kinetic energy by LES increases in the first few cycles and slowly converges, but it is close to zero in RANS. Jhavar et al. [80] simulated turbulent combustion in a CAT 3351 IC engine with the KIVA-3V software, using a one-equation SGS stress model [102], and a CHEMKIN-based combustion model. Their simulations indicate that in contrast to RANS models, LES models are able to predict the CCV. LES methods has also been applied to more realistic engine [81]. For a more detailed review of some earlier IC engines simulations via LES see the review by Celik et al. [74].

In this chapter, the in-cylinder flow, spray and combustion in various engine related configurations are simulated with our new two-phase compressible scalar filtered mass density function (FMDF) model. The FMDF is a promising SGS model for LES of turbulent combustion [18, 19, 44, 45, 42, 43]. however, it has not been applied yet to complex flows of the type seen in IC engines. FMDF denotes the single-point joint SGS PDF of turbulent variables. Therefore, all processes represented by single-point terms in the FMDF formulations appear in a closed form in this formulation. However, the FMDF transport equation is not closed, and some form of modeling for multi-point correlations is still required. Jaber et al. [19] developed a SGS PDF model for LES based on the scalar FMDF, which is essentially the mass weighted filtered value of the fine-grained densities of energy and species mass fractions. In the scalar FMDF transport equation, all chemical (source or sink) terms are closed, making the FMDF very attractive for turbulent combustion simulations. Several applications of scalar FMDF are recently reported [46, 4, 53, 54, 82]. FMDF for velocity [47], velocity-scalar [48, 49, 50, 51], and frequency-velocity-scalar FMDF [52] are also developed. More recently, the scalar FMDF model is extended to compressible flows [82] and to multiphase combustion in realistic configurations. The new multiphase LES/FMDF methodology is implemented through an efficient Lagrangian-Eulerian-

Lagrangian mathematical/computational methodology [55, 56, 31, 57]. Most of two-phase LES models are developed for non-reacting turbulent flows; the application of LES models to turbulent flows involving droplet evaporation and combustion is somewhat limited [55, 83, 84, 85, 86, 87, 88, 89]. In this study, the turbulent flow, spray and combustion in three different configurations, all related to IC engines are simulated with our new high-order two-phase compressible scalar LES/FMDF model. This is the first time that the FMDF model is applied to such a complicated problem. The main objectives are to develop/evaluate high-order consistent LES/FMDF models for turbulent mixing and combustion in IC engines and to use them for better understanding of flow in these engines. Large-eddy simulations of turbulent flows in three different configurations are considered. The first one involves the flow around a poppet valve in an axisymmetric sudden expansion [104]. This is a simple problem used for understanding of the flow around and behind intake valves in IC engines. The second configuration is that of Morse et al. [99], consisting of a fixed open valve and a slowly moving flat piston. The last configuration is the most complex one, describing the in-cylinder flow in a 3-valve direct-injection spark-ignition (DISI) laboratory engine, built at Michigan State University.

5.2 Results

As indicated in the introduction, non-reacting and reacting flows, with and without spray, in three IC engine related geometries are simulated in this chapter: (1) the flow around a fixed valve, (2) the flow in a simple piston-cylinder assembly with fixed open valve, and (3) the flow, spray and combustion in a three-valve DISI engine. The results obtained by LES for non-reacting flows and LES/FMDF for reacting flows are presented below in two different sections.

5.2.1 Non-reacting flows

Among the three non-reacting flows considered in this section, the flow around a fixed valve is the simplest one. It does not involve any moving component. The second flow is a piston-cylinder assembly with fixed open valve and moving piston and is more complicated than the first one due to the presence of a moving piston. However, it is still much simpler than the flow in a realistic IC engine. The last flow considered mimicked some of the features of in-cylinder flow in DISI engines.

5.2.1.1 Sudden expansion with a poppet valve

During the intake stroke in a typical IC engine operation, large-scale vortical fluid motions are normally developed behind the intake valves. These motions have significant effect on mixing and combustion in the cylinder at later times of engine operation. The ability of LES and SGS models to capture the vortical fluid motions behind the valve is assessed here by simulating the non-reacting flow in a sudden expansion geometry with a fixed poppet valve [104] (Fig. 5.1(a)). The mass flow rate is kept constant at 0.05 kg/s and the Reynolds number is 30,000. Fig. 5.1(b) shows the 3-dimensional (3D) and 2-dimensional (2D) views of the 5-block grid system used for simulating this flow with our high order LES code. To avoid singularity at the centerline, a rectangular H-H block was employed at the center, coupled with an O-H grid outside. The 3D and 2D contour plots of vorticity and streamlines for this flow are shown in Fig. 5.2(a) and (b), respectively. The results in this figure confirm the generation of large-scale vortical fluid motions behind the valve and in the corner of the cylinder head and cylinder wall. As "fluid particles" accelerates around the valve and enters the cylinder, they get divided into three parts. The part that reaches the wall is partly reflected away from the valve toward the outlet boundary and is partly returned back to the region behind the valve, generating a wake-like flow structure. Finally a fraction of the flow recirculates back toward the cylinder head corner region.

To make a quantitative comparison with the experimental data, the mean axial velocity and the root mean square (rms) values of the axial velocity at two locations (20 and 70 mm) from the cylinder head are calculated from the LES data and are compared with the experimental data in Figs. 5.3(a) and (b). The mean velocity is calculated by time-averaging of the filtered velocity for about 0.03 second. Figure 5.3(a) shows that the mean axial velocity, as obtained with the dynamic SGS Smagorinsky model is in good agreement with the experimental data. The rms of axial velocity calculated with a similar phase-averaging method also compares reasonably well with the LDA laboratory data in the middle of the cylinder and behind the poppet valve as shown in Fig. 5.3(b) (see the results from $r/R=0$ to $r/R=0.5$). The discrepancy between the experimental and numerical results in the region close to the cylinder wall (from $r/R=0.5$ to $r/R=1.0$) can be attributed to the wall model or to the inlet flow condition. The predicted mean and rms values with constant coefficient Smagorinsky model ($C_d = 0.1$) seem to be more "diffused" in comparison with the experimental data.

5.2.1.2 Piston-cylinder assembly with an intake/exhaust valve

The second non-reacting flow configuration, considered here for better understanding of the in-cylinder flow physics and validation of LES flow solver and SGS stress models, is a simple piston-cylinder assembly with a fixed open valve. The geometrical features of this idealized "engine" are shown in Fig. 5.4(a). The engine is made of a fixed intake/exhaust valve with a flat piston which moves with simple harmonic motion and low RPM of 200. The average piston speed (V_p) is 0.4 m/s and the flow Reynolds number based on the cylinder diameter and average piston speed is 2000. Using the LDA method, Morse et al. [99] measured the velocity in this engine and reported the radial profiles of the phase-averaged mean and rms of axial velocity at different locations and crank angles in the cylinder. The 3D and 2D views of the

4-block grid system employed for simulating the flow field in this engine is shown in Fig. 5.4(b). The simulated flow during the intake stroke has some similarities to that in the previous configuration, even though it is unsteady due to harmonic motion of the piston. Devesa et al. [106] conducted their LES with a specific set of non-zero initial velocity conditions to reduce the computational time. They simulated the jet-tumble interactions with this initialization. The LES calculations presented in this work were all initiated with zero velocity and constant pressure and temperature. We then allow the turbulence to be naturally generated and grown by the governing equations during the subsequent cycles. The in-cylinder flow is found to be unsteady, 3D and turbulent after the first cycle.

The instantaneous contour plots of the axial in-cylinder velocity, normalized with the mean piston speed during the first cycle are shown in Figs. 5.5(a), (b), (c) and (d) at four crank angles of 24° , 48° , 108° and 180° , respectively. By accelerating the piston downward from its initial position at top dead center (TDC), the fluid around the fixed valve accelerates and enters the cylinder like a coannular jet flow. As the accelerated flow enters the cylinder, a major portion of it moves downward toward the piston but a portion of the remaining fluid still turns back toward the cylinder head, generating a large-scale wake-like structure behind the valve. A smaller recirculating zone also appears at the upper corner of the cylinder, with the direction of rotation being the opposite of the flow behind the valve (see Fig. 5.5(a)). Later at the crank angle of 48° a vortical motion is generated close to the piston where the main jet rotates from the piston toward the cylinder wall (see Fig. 5.5(b)). Around crank angle of 80° , the small corner vortex disappears but it reappears again when the crank angle is about 108° and the intake jet flow reaches the cylinder wall. Also at this crank angle, the wake behind the valve moves toward the cylinder wall and the flow induced by the piston becomes smaller as it rotates away from the piston (see Fig. 5.5(c)). Figure 5.5(d) shows that just before the bottom dead center (BDC) the

generated large-scale motions become unstable and break down into smaller scales.

The axisymmetric geometry of the cylinder permits averaging in the azimuthal direction. The data gathered by azimuthal averaging for any piston position or specific crank angle may also be further averaged over different cycles, excluding the first cycle, to get the ensemble or phase-averaged mean and rms values of the velocity. Figure 5.6 shows the azimuthal-averaged values of the filtered axial velocity and its rms for six subsequent cycles at crank angle of 36° and at the location 10 mm from the cylinder head. This figure displays the CCV of the in-cylinder flow variables. The radial profiles of the mean axial velocity and the rms of axial velocity calculated by azimuthal-averaging and phase-averaging of the data at crank angle of 36° and at locations of 10, 20 and 30 mm from the cylinder head are shown in Fig. 5.7. The reported mean axial velocities, computed with both static and dynamic Smagorinsky model, are shown to be in agreement with the experimental data. However, the dynamic model is shown to predict the rms values better than the static model. The predicted mean and rms values of the axial velocity at crank angle of 144° and different locations (Fig. 5.8) are in good agreement with the experimental data. This indicates that LES is able to capture the spatial variations of the axial velocity within the cylinder at different crank angles.

5.2.1.3 Three-valve DISI engine

The two flow configurations described in the previous sections have some geometrical and flow features of realistic engines and are considered here for validation of LES model and its complex moving mesh technique. The results of these two flows clearly indicate that the LES is applicable to flows in more complex and more realistic "engines".

In this section, we consider the non-reacting in-cylinder flow in a single-cylinder 3-valve direct-injection spark-ignition (DISI) optically accessible engine, which is built

by our experimental group at the Michigan State University (see Fig. 5.9 for schematic views of the engine). In order to improve the fuel-air mixing during the intake stroke and to facilitate discharge of burnt gases, the engine is made with two intake valves and one bigger exhaust valve, with valves being tilted with respect to the piston. The maximum valve lifts for the intake and exhaust valves are 11 and 12 mm, respectively. The engine is simulated with LES for a constant RPM of 2500 and mean piston speed of 12.5 m/s. To have a high quality grid for the moving piston, complicated cylinder head and moving valves, a complex 9-block grid system is generated out of 32 initial blocks (Fig. 5.10). In addition to these blocks, there are three blocks covering each of the three intake/exhaust valves and the corresponding manifold sections. Each valve has a separate block for moving in/out of the cylinder. By adding the valve and manifold grids to the cylinder grids, a total of 18-block grid is generated. As valves move up and down, their corresponding grids move with different velocities than the surrounding grids in the cylinder, which move with the piston speed. Therefore, the grids that cover the overlap regions between the moving blocks can no longer be kept aligned and some interpolation for transferring the data between the blocks is needed. The flow field inside the cylinder, around the valves and in the port sections are simulated by our LES model using the 18-block grid system. Several cycle are simulated on 18 CPUs with an efficient parallel algorithm. The grid resolution and time stepping are selected to resolve the large-scale length and time scales in LES [79, 107, 108].

Figures 5.11(a), (b) and (c) show the volume-averaged temperature, vorticity and SGS turbulent viscosity predicted by LES with the constant coefficient Smagorinsky model ($C_d = 0.17$) at different crank angles. Experimental observations do not indicate considerable CCV in the thermodynamic variables, but the CCV in the velocity field is significant. Consistent with the experimental observations, the LES results indicate insignificant CCV in the averaged temperature but the CCV in the vorticity

and SGS turbulent viscosity are shown to be significant. During the intake stroke, as the incoming air accelerates around the valves, the volume-averaged values of the vorticity and SGS turbulent viscosity increase and reach to their maximum values at mid-intake stroke, and then decrease as piston decelerates, but the volume-averaged temperature remains nearly constant. During the compression stroke, the average temperature increases and reaches to its maximum value at TDC as expected, while the vorticity and SGS turbulent viscosity continue to decrease with significant CCV. At the beginning of the expansion stroke, the initial acceleration of piston causes a slight increase in the vorticity and SGS turbulent viscosity, but the gas temperature starts to decrease. With the opening of the exhaust valve 90 degree after the TDC, the vorticity and SGS turbulent viscosity both increase.

The rms values of the temperature and velocity components at different crank angles are shown in Fig. 5.12(a). They are calculated by averaging over six cycles, ignoring the first cycle. Similar to the plots shown for the average vorticity, the rms of velocity components increase during the intake stroke, reaching to their maximum values in the middle of the intake stroke, then decrease continuously till the end of compression stroke. While the velocity rms values increase at the beginning of expansion stroke and opening of the exhaust valve, that of temperature remains very small during the intake stroke. However, during the compression stroke, the rms of temperature increases and reaches to its maximum value at TDC and then decreases again during the expansion stroke. Figure 5.12(b) shows the volumetric average values of SGS turbulent viscosity, vorticity magnitude, velocity vector magnitude and piston speed, normalized by their minimum and maximum values are compared. The graphs follow the piston/valve movement, they increase and reach to their peak values first then decrease as piston speed decreases. Acceleration of piston during the first half part of the intake stroke draws the manifold air into the cylinder with such a high speed that generates strong vorticity, velocity gradients and SGS turbulent viscosity.

Later during the intake stroke, the piston decelerates to the BDC and the intake flow speed starts to decrease leading to lower values of vorticity and SGS turbulent viscosity. During the compression stroke, although the piston accelerates toward the TDC, the intake valves are closed, therefore the volumetric average values of variables shown in Fig. 5.12(b) decrease.

To quantify the flow inhomogeneity and the level of turbulence in the cylinder during the intake and compression strokes, the volumetric average values of turbulent intensity are calculated at nine different zones or sections inside the cylinder. These sections, as shown in Fig. 5.13(a), have equal volumes and cover different regions of the flow near the cylinder head. The calculated turbulent intensity at each section at crank angle of 90° , 180° , 270° , and 360° are shown in Fig. 5.13(b). Based on the results in this figure, one may conclude that the in-cylinder flow is highly inhomogeneous at mid-intake stroke time ($CA=90^\circ$), after that time, in-cylinder turbulent flow starts to decay and becomes relatively homogenous at the end of compression stroke.

For a better understanding of the flow dynamics during the intake stroke, the evolution of flow variables (e.g. pressure and velocity) for a set of 40 Lagrangian fluid particles were monitored during the simulation. These particles were originally located around one of the intake valves at crank angle of 30° , but they move into the cylinder along various paths by the filtered velocity, molecular and subgrid diffusions. The velocity, pressure and temperature at each particle location were interpolated from the surrounding Eulerian grid points at every time step. Figure 5.14(a), (b) and (c) show the temperature, the vorticity, and the kinetic energy of 6 sample particles at different crank angles. During the intake stroke, the particles have very different temperature, vorticity and kinetic energy as they undergo different paths and experience different flow conditions. However, during the compression stroke, the particle values become closer to the volume-averaged values. These findings are consistent with the results shown in Fig. 5.13(b), indicating that the flow is highly inhomogeneous during

the intake stroke but becomes relatively homogeneous in the compression stroke. During the intake stroke, the flow in the 3-valve engine has some similarities with that in the non-moving single-valve "engine" (Figs. 5.4-5.8). For example, the recirculation zones between the valve and the cylinder wall or the wake flow behind the valves are somewhat similar. There are, however, some noticeable differences between these two flows. For instance, in the 3-valve engine, as the incoming flow from the intake ports enter the cylinder and merge, they form a stronger flow that has different physical structures and turbulent features than those shown in the single-valve engine. In the 3-valve engine, part of the flow recirculates back toward the cylinder head making two large-scale vortices in the corners of the cylinder head. Other vortical motions are generated when the incoming flow from the tilted intake valves accelerates inside the cylinder toward the region under the closed exhaust valve. As the flow reaches the cylinder wall, a significant portion of it moves toward the piston, but a fraction of it returns back toward the exhaust valve. These fluid movements are visualized with 4 sample particles and their corresponding Lagrangian variables (Fig. 5.14). The path-lines of sample particles together with 3D contour plots of the pressure during the intake stroke at crank angles of 60° , 90° , and 180° are shown in Figs. 5.15(a), (b) and (c), respectively. Close examinations of various particle path-lines indicate that some of the particles are initially trapped at the recirculation zone between one of the intake valves and the cylinder walls at corner regions before entering the center portion of the cylinder. In contrast, some of the fluid particles circulate for some time in the vortical flow between the two valves, and then move into the cylinder in the wake flow behind the intake valves. There are also some particles moving directly into the central section of the cylinder in the region just under the exhaust valve. Some of these particles reach to the piston, but some return back toward the exhaust valve. The pressure contours in Figs. 5.15(a), (b) and (c) indicate that during the intake stroke, the in-cylinder pressure is smaller than the manifold pressure on average. This

is because of the vacuum generated by the piston which is expected. However, at the end of intake stroke, when the piston decelerates, and the manifold air enters the engine with high momentum, the in-cylinder pressure becomes slightly higher than the manifold pressure.

Figures 5.16(a), (b) and (c) show the 2D axial velocity at a center plane over the intake valve at crank angles of 60° , 90° , and 180° , respectively. At 60° crank angle (Fig. 5.16(a)), the piston velocity and valve lift are 8.5 m/s and 8 mm. At this crank angle, a strong vorticity field is observed at the upper corner of the cylinder close to the intake valves. In Fig. 5.16(b), the piston is at its maximum velocity of 14 m/s and the valve lift is 11 mm. Again, there is a vorticity at the cylinder corner, a wake flow behind the valve, and a recirculation zone under the exhaust valve, all interacting with each other and with the cylinder and piston wall. With the deceleration of piston the in-cylinder vorticity and the turbulence are weakened to such an extent that at BDC (Fig. 5.16(c)) the recirculation zones almost disappear. At crank angle of 220° during the compression stroke, the intake valves are closed. From this point, the main source of turbulent production is absent and the piston motion compresses the in-cylinder flow to higher pressures and temperatures while the in-cylinder turbulence decays and becomes somewhat homogeneous. Nevertheless, the 2D and 3D contours of velocity, vorticity, pressure, and temperature indicate that in-cylinder flow is a complex unsteady inhomogeneous turbulent flow with substantial CCV, justifying the use of LES for simulation of flows in IC engines.

5.2.2 Reacting flows

In this section, the results obtained by the LES/FMDF model for reacting flows (with and without spray) in the DISI engine is presented. In the simulated DISI engine, the fuel is injected into the cylinder during the intake stroke at sufficiently early times so that the fuel is evaporated, mixed and compressed prior to the ignition. How-

ever, before simulating the spray combustion with the LES/FMDF model, premixed single-phase combustion simulations in the DISI engine are performed to establish the accuracy of the LES solver for simpler system.

5.2.2.1 Reacting flow without spray

In the spark ignition engines, the combustion is initiated by an electrical spark some time before TDC. Advance ignition gives sufficient time for the ignition and flame propagation before the piston reaches to TDC. Generally, the size of the spark can be smaller than the LES filter size, and in that case SGS model may be employed in "conventional" LES models to represent the ignition. In the LES/FMDF methodology, the MC particles can move freely in the computational domain including the SGS domain. Here, the spark plug is modeled by adding a energy deposition source term [109]:

$$\dot{Q}_{ig} = \frac{\epsilon}{4\pi^2 \Delta_{ig}^3 \tau_{ig}} \exp\left(-\frac{1}{2} \frac{(X_i^+ - X_{ig})^2}{\Delta_{ig}^2}\right) \exp\left(-\frac{1}{2} \frac{(t - t_m)^2}{\tau_{ig}^2}\right). \quad (5.1)$$

to the FMDF equation. By including this term in the FMDF stochastic MC equation for the enthalpy (Eq. (2.35) with $\alpha = N_{s+1}$), certain amount of energy ϵ is added to the MC particles which are located in the vicinity of spark plug with the length scale Δ_{ig} and within the time scale τ_{ig} . These two parameters should be set in such a way that the temperature does not increase beyond a specific temperature [109]. The temperature profile generated by this source term is Gaussian in space and time. In Eq. (5.1), X_i^+ and X_{ig} are the position of MC particles and location of the spark plug, respectively. Also, t_m is the time of maximum input power. Using Eq. (2.37), the source term in Eq. (5.1) is then weighted averaged and added to the LES-FD energy equation at every time step. Although the energy deposition ignition model defined in Eq. (5.1) does not simulate the plasma thermodynamics,

it can capture the initial flame kernel. Before starting the combustion, the flow in the cylinder is simulated for several cycles. At crank angle of 220° during the compression stroke, the intake valves are closed. At this crank angle, MC particles are introduced randomly in the cylinder with the initial in-cylinder flow temperature and perfectly premixed stoichiometric i-octane/air mixture. During the compression, the total derivative of pressure ($D\langle p\rangle_t/Dt$), as computed from the Eulerian grid points are interpolated and added to the corresponding MC particles. Consistency of the temperature obtained from the Lagrangian MC data, with those obtained by the Eulerian carrier-gas equations via finite difference (FD) method is dependent on the inclusion of the pressure term in the FMDF equation [82]. At crank angle of 335° , ignition energy deposition source term is added to the FMDF-MC equation for about 1 crank angle time. For the i-octane reaction, a one step global mechanism is employed [90]. Figures 5.17(a),(b) and (c) show the iso-levels and scatter plots of temperature as predicted by LES-FD and FMDF-MC at crank angles 345° 355° and 365° . In the previous section, it was shown that the in-cylinder flow becomes nearly homogeneous at the end of compression stroke. With the premixed mixture and homogeneous flow condition, the flame propagates radially from the cylinder center at TDC where the ignition starts. The diameter of the "flame front" in Fig. 5.17(a) and (b) are about 20 and 40 mm. Nevertheless, the flame propagation after ignition is well captured by the LES/FMDF. The temperature predicted by the LES-FD and FMDF-MC during the flame propagation are in good agreement with each other. The scatter plots of LES-FD and FMDF-MC temperatures also show good consistency between two methods at all crank angles. The consistency of LES-FD and FMDF-MC results indicate the accuracy of the numerical simulation. Some of the differences are due to numerical diffusivity in the LES-FD.

5.2.2.2 Spray combustion in DISI engine

After establishing consistency of LES-FD and FMDF-MC for single-phase combustion system, the new two-phase compressible scalar LES/FMDF model is employed to study the spray and combustion in the DISI engine. The spray combustion in the DISI engine combustion have been studied experimentally [110, 111] and numerically [112, 113] in the past. For the spray combustion simulation, we allow the flow in the cylinder to be developed for several cycles before spray and combustion starts. The fuel injection starts when the crank angle is 79° and stops at crank angle of 148° . Fuel injector has 8 nozzles and is located between the intake valves in the cylinder head. Fuel droplets are injected toward the region under the exhaust valve. Here, the liquid i-octane fuel are injected with average initial velocity of 50 m/s and a Rosin-Rammler distribution with Sauter mean diameter (SMD) of $30\mu m$ is used to represent the initial droplet distribution before they undergo secondary break-up. Secondary Spray droplet break-up was performed by the standard Rayleigh-Taylor (RT) model [92, 114, 115]. Those droplets which reach the piston and cylinder wall are modeled to randomly bounce back or to stick to the walls as a liquid film. Figures 5.18(a), (b) and (c) show the injected fuel droplets at crank angles of 84° , 100° and 148° , respectively. Initial spray pattern and impingement of droplets to the cylinder wall under the exhaust valve are shown in Figs. 5.18(a), (b). Some of the droplets which were reflected back from the wall under the exhaust valve are shown in Fig. 5.18(c). Also, due to circular fluid motion in the cylinder above the open intake valves some fuel droplets enter the intake manifold (Fig. 5.18(c)). Similar patterns for the fuel droplets and for the impingement of droplets on the cylinder wall below the exhaust valve and on the intake valve were observed in the experiment [110, 111]. A close examination of the contour plots of temperature and the evaporated fuel mass fraction indicate that during the intake stroke the carrier gas temperature is

relatively low and there is no considerable fuel evaporation. During the intake and early compression stroke period (between crank angles of $79^\circ - 270^\circ$), droplets are strongly dispersed under the influence of in-cylinder turbulent flow and evaporation is not significant. High level of fuel evaporation starts in the middle of compression stroke as the temperature increases. Secondary break-up of particles are found to be not important as initial injected droplets' sizes are small.

Figure 5.19 shows the 2D contour plots of the evaporated fuel mass fraction and the temperature at the center plane of the exhaust valve at crank angle of 270° as predicted by LES-FD and FMDF-MC. Qualitatively, the LES-FD and FMDF-FD predictions are consistent at this crank angle. Consistency of these two parts of the hybrid two-phase LES/FMDF methodology is important and establishes the accuracy of both LES-FD and FMDF-MC flow solvers. In order to assess the performance of compressible two-phase FMDF, the spatial variations of the gas temperature and evaporated fuel mass fraction as predicted by LES-FD and FMDF-MC along three arbitrary axial lines are also compared in Fig. 5.20. These lines are chosen to be the ones connecting the center of the exhaust and the two intake valves to the piston face. In Fig. 5.20, the comparison between the LES-FD and the FMDF-MC results are made during the compression at three different crank angles of 250° , 290° and 330° . The high rate of evaporation and significant changes in temperature during the compression stroke is very well captured by the compressible two-phase FMDF model. Good consistency between the LES-FD and FMDF-MC results during the compression stroke between the turbulent gas temperature and the evaporated fuel droplets confirms the accuracy and the reliability of the three-way coupling of Eulerian carrier gas, Lagrangian fuel droplets and MC particles equations.

The 2D contour plots of the evaporated fuel mass fraction and the gas temperature at a parallel plane to the piston at crank angle of 335° , just before the ignition, as predicted by the LES-FD and FMDF-MC are shown in Fig. 5.21. Scatter plots of

LES-FD and FMDF-MC fuel mass fractions and temperatures are also shown in Fig. 5.21. These figures clearly show the consistency of LES-FD and FMDF-MC parts of the hybrid model and the reliability of its numerical solution method for complex spray combustion systems. The combustion is initiated by activating a spark plug in the cylinder head, when the crank angle is 335° . Numerically, it is modeled by adding the energy deposition source term (Eq. (5.1)) to the FMDF energy equation which increases the energy content of MC particles that are within the spark plug area. Using Eq. (2.37), this source term is weighted averaged and added to the LES-FD energy equation as well. The iso-levels and scatter plots of temperature as predicted by LES-FD and FMDF-MC at crank angles 345° 355° and 365° are shown in Figs. 5.22(a), (b) and (c). Due to inhomogeneity of fuel mass fraction and temperature at the time of ignition (Fig. 5.21), unlike the previous section for premixed flame, the flame does not propagate radially. Nevertheless, the complex turbulent flame propagation after ignition is very well captured by the LES/FMDF. Scatter plots of LES-FD and FMDF-MC temperatures at different crank angles again show consistency and accuracy of the numerical methods.

Figure 5.23 shows the volume-averaged in-cylinder values of filtered pressure, temperature and fuel mass fraction. This figure shows that the flame propagation takes about 30 crank angles time after the ignition. The volume-averaged pressure reaches a peak value few degree after the TDC which is in good agreement with the experimental data in Ref. [111]. Volume-averaged values of the temperature and fuel mass fraction as predicted by the FMDF-MC are also shown in Fig. 5.23 to be in good agreement with the LES-FD results.

5.3 Conclusions

To better understand and model the fluid motions, spray and combustion in internal combustion (IC) engines, large-eddy simulations (LES) of flow in several IC engines relevant configurations are performed. Spray and combustion simulations are conducted with our probability density function based two-phase subgrid combustion model, termed the filtered mass density function (FMDF) and its hybrid finite difference-Monte Carlo (FD-MC) method. A new Lagrangian-Eulerian-Lagrangian computational methodology is employed for simulating the flow, spray and combustion. Non-reacting and reacting flows with and without spray are simulated for three configurations: (1) non-reacting flow around a fixed poppet valve in a sudden expansion, (2) non-reacting flow in a simple piston cylinder assembly with a stationary valve and harmonically moving flat piston, (3) non-reacting and reacting flows with and without spray in a single-cylinder, 3-valve direct-injection spark-ignition (DISI) engine with moving valves and piston. The first two configurations are relatively simple in comparison to those seen in real IC engines, and are considered here for better understanding of the in-cylinder fluid flow dynamics and validation of LES. The third configuration represents the in-cylinder flow in a realistic DISI engine. The first flow is a simplified steady state representation of the flow over valves in IC engines during intake stroke. The LES results for this flow indicate that the fluid enters the cylinder like a coannular jet and large-scale vortical fluid motions are generated in the cylinder head corners and behind the intake valve as expected. Comparison of mean axial velocity and its rms, as obtained with the constant coefficient and dynamic Smagorinsky models, with the experimental data indicate that the flow statistics are predicted well by the dynamic Smagorinsky model. Complete unsteady simulation of the intake stroke flow is carried on the second flow configuration which involves a moving piston but a fixed valve. The harmonic movement of the piston causes un-

steady generation and dissipation of large-scale vortical fluid motions in the cylinder. The LES results indicate cycle-to-cycle variations (CCV) in the in-cylinder velocity field. The predicted axial velocity and its rms by the (constant-coefficient and the dynamic) Smagorinsky SGS models are shown to compare well with the experimental data. The LES results for the third flow configuration (DISI engine), indicate substantial CCV in velocity field but CCV of the thermodynamic variables are found to be not significant. This is consistent with the experimental observation. During the intake stroke, the flow through the open intake valves into the cylinder makes the in-cylinder flow highly inhomogeneous. However, during the compression stroke and after closing the intake valves, the in-cylinder flow becomes more homogeneous as the turbulence decays. Studies of the path-lines of Lagrangian fluid particles in the cylinder also indicate that the particles entering the cylinder attain very different values as they travel through different paths. During compression stroke, the particle values became closer to the in-cylinder averaged values. Reacting flow simulations (with and without spray) in the DISI engine with the two-phase compressible LES/FMDF model also show the reliability of the model. For the case without spray, a premixed i-octane mixture in the cylinder is considered. It is shown that the premixed flame propagates radially after the ignition. The flame propagation is consistently well captured by the LES-FD and FMDF-MC parts of the hybrid LES-FD and FMDF-MC model. For the spray combustion simulation, it is shown that the fuel mass fraction and temperature statistics obtained by the FD and MC components of the hybrid solver are also in good agreement with each other despite complexity of the flow due to spray, evaporation, mixing, non-premixed combustion and complex geometry. High correlation between the Eulerian and Lagrangian parts of the LES/FMDF model is established during the gas compression, fuel droplet evaporation and constant-volume combustion in the DISI engine. This indicates the accuracy of the three way coupling between the flow, spray and combustion (FMDF) equation.

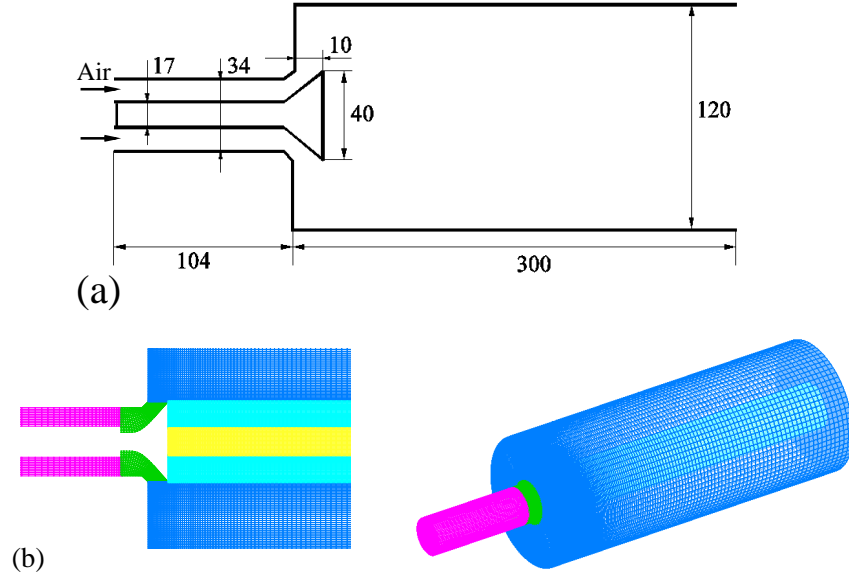


Figure 5.1: (a) Geometrical details of the sudden expansion configuration with fixed valve. There is no piston and the valve is fixed, (b) Two-dimensional and three-dimensional cross sectional view of the 5-block grid system employed for LES of the sudden-expansion plus valve flow configuration.

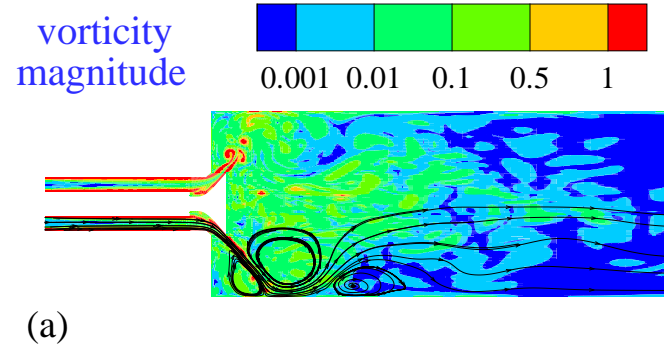


Figure 5.2: (a) Two-dimensional and (b) three-dimensional contour plots of vorticity.

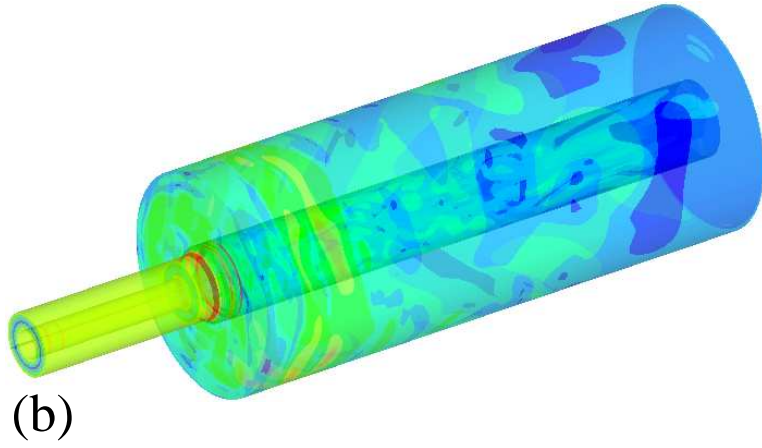


Figure 5.2 continued.

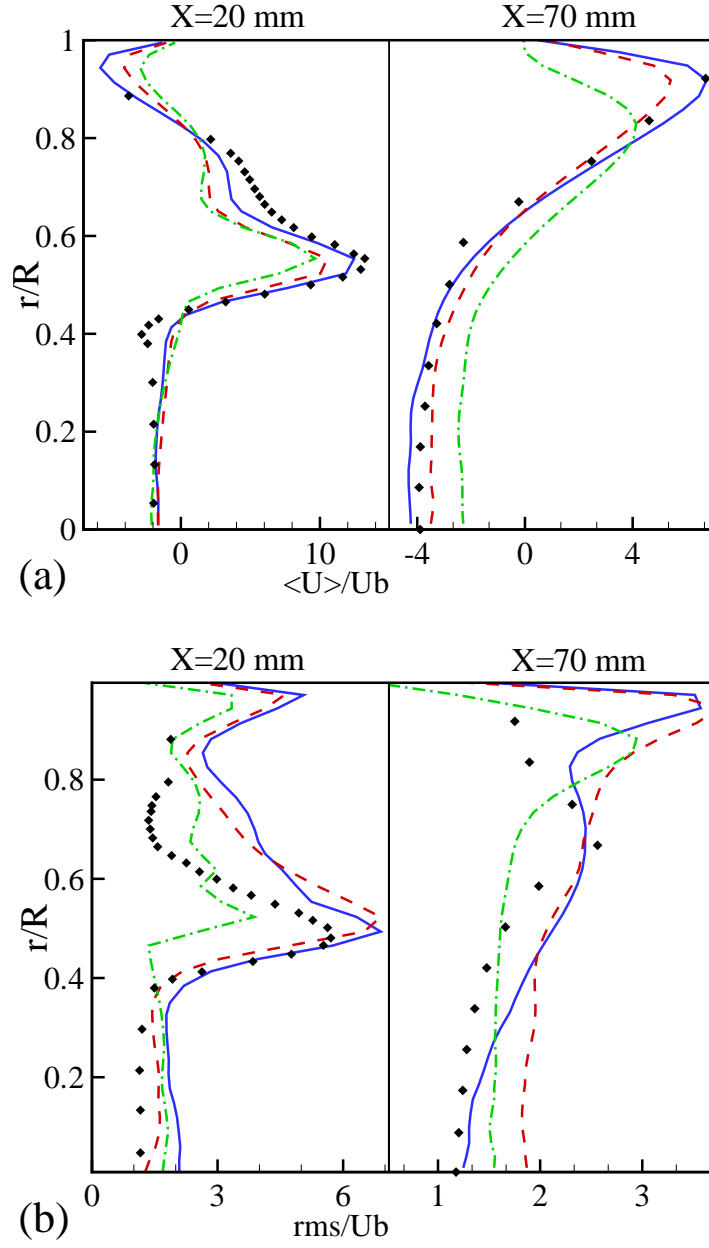


Figure 5.3: (a) Mean axial velocity and (b) rms of axial velocity normalized with the inlet velocity. Solid lines and dashed lines show the LES results with dynamic and constant coefficient ($C_d = 0.1$) Smagorinsky, respectively. Symbols represent the experimental (LDA) data.

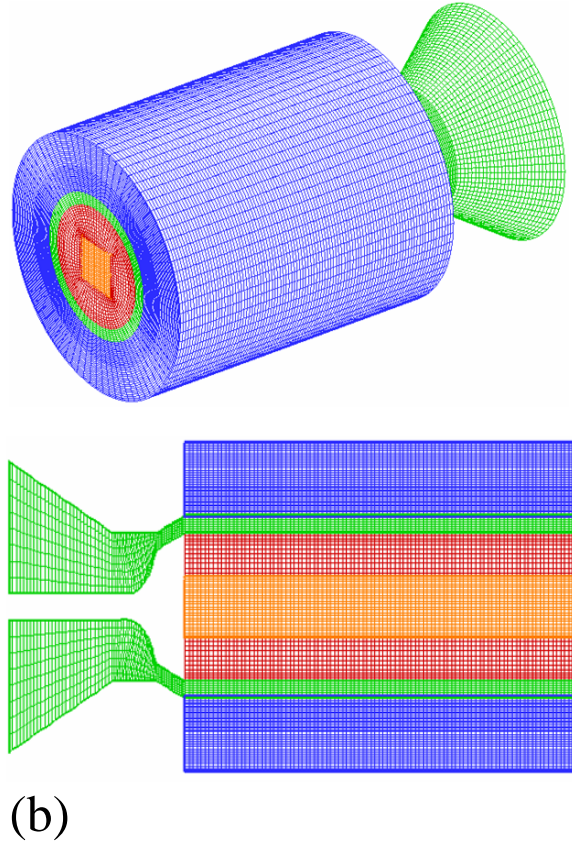
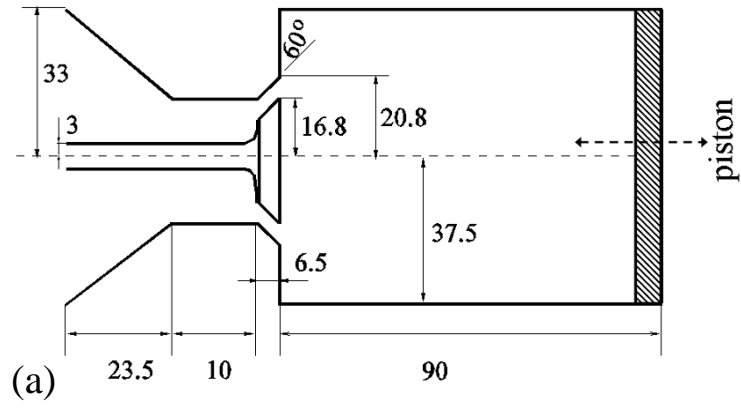


Figure 5.4: (a) Geometrical details of the simulated piston-cylinder assembly with fixed valve and moving piston (Moore et al.[23]),(b) Three-dimensional and two-dimensional view of the 4-block grid system employed for LES of flow in a simple piston-cylinder configuration with fixed valve and flat moving piston.

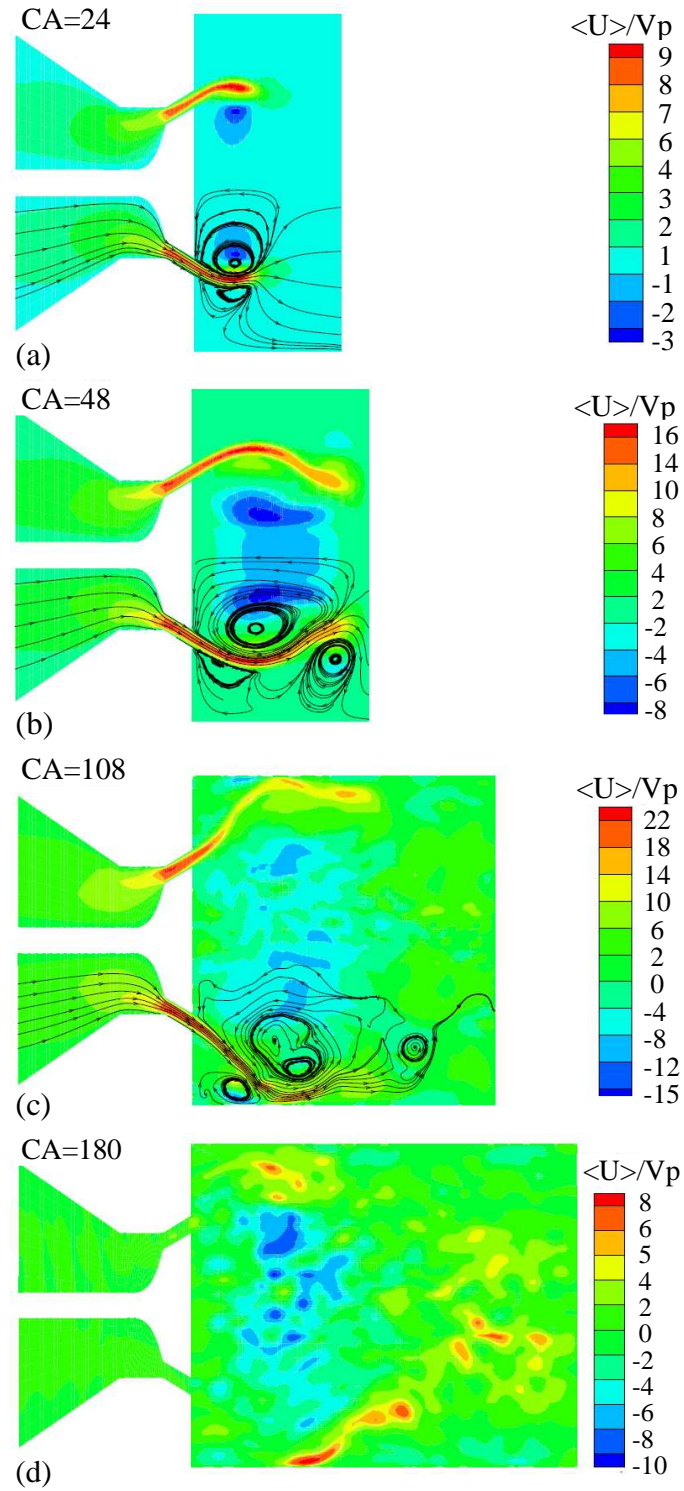


Figure 5.5: Instantaneous contours of the axial velocity normalized by the mean piston speed, (a) at crank angle of 24, (b) at crank angle of 48 (c) at crank angle of 108, (d) at crank angle of 180.

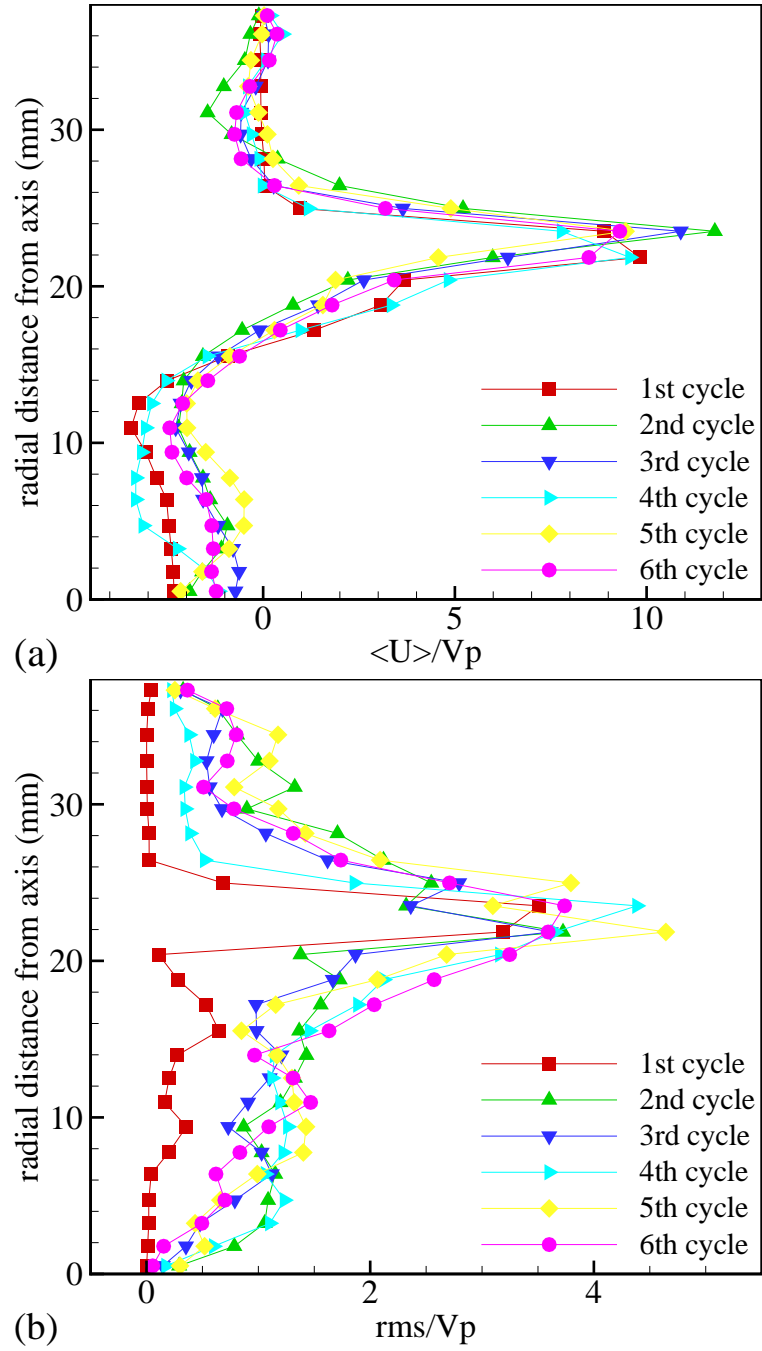


Figure 5.6: (a) Mean axial velocity and (b) rms of axial velocity, normalized by the mean piston speed, at crank angle of 36° and location of 10 mm from the cylinder head calculated by azimuthally averaging of the instantaneous filtered velocity for six subsequent cycles.

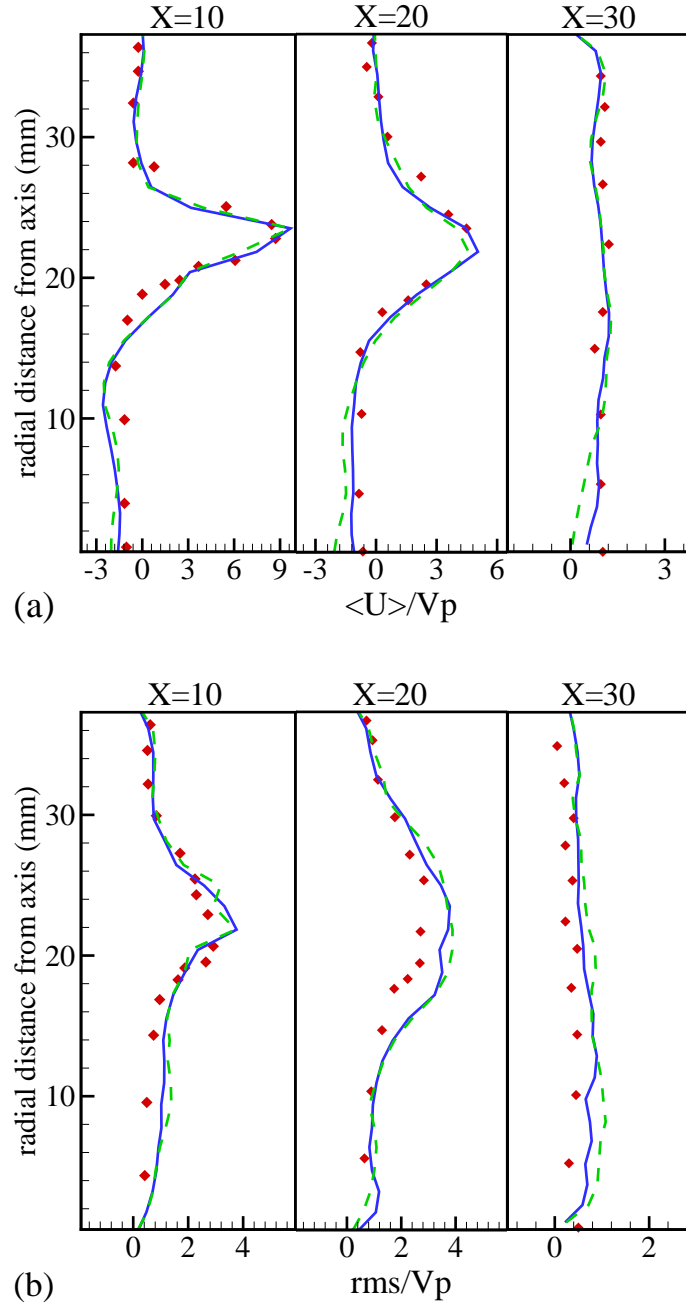


Figure 5.7: (a) Mean axial velocity and (b) rms of axial velocity, normalized by the mean piston speed, at crank angle of 36° . Solid lines and dashed lines are LES results obtained by the dynamic and constant coefficient ($C_d = 0.1$) Smagorinsky models, respectively, and symbols are LDA data.

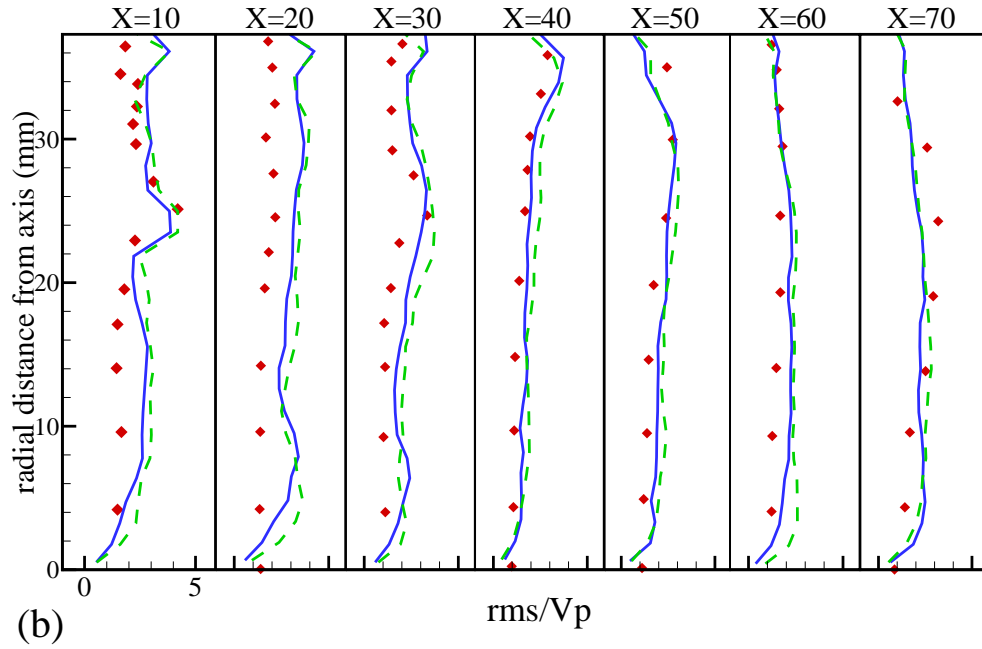
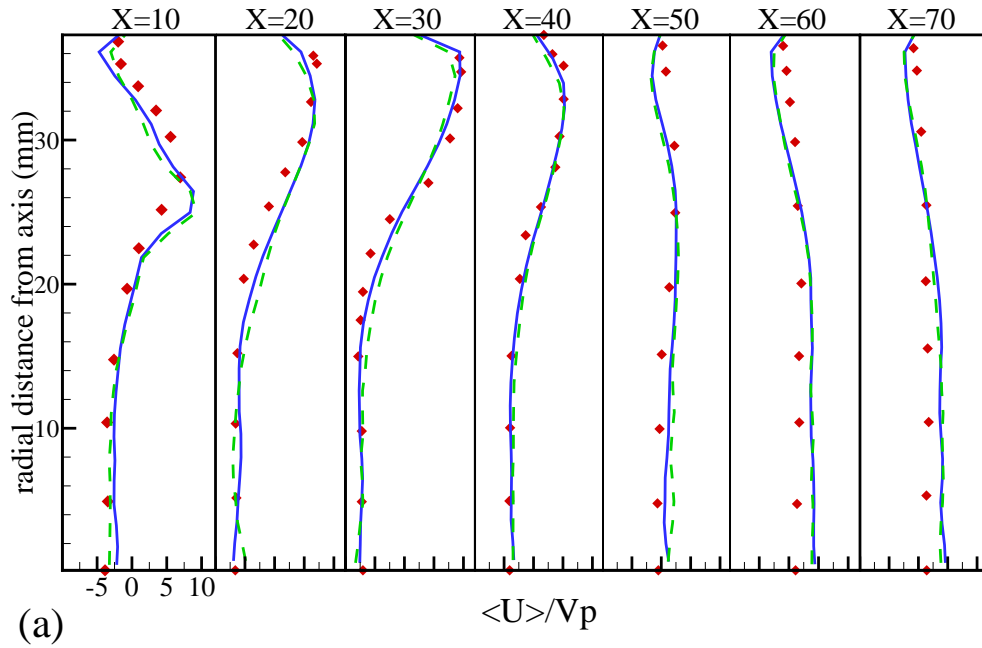
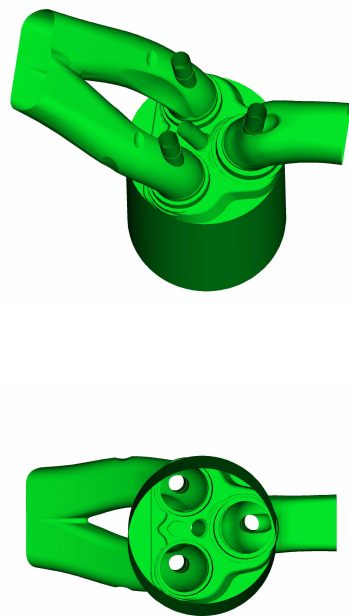
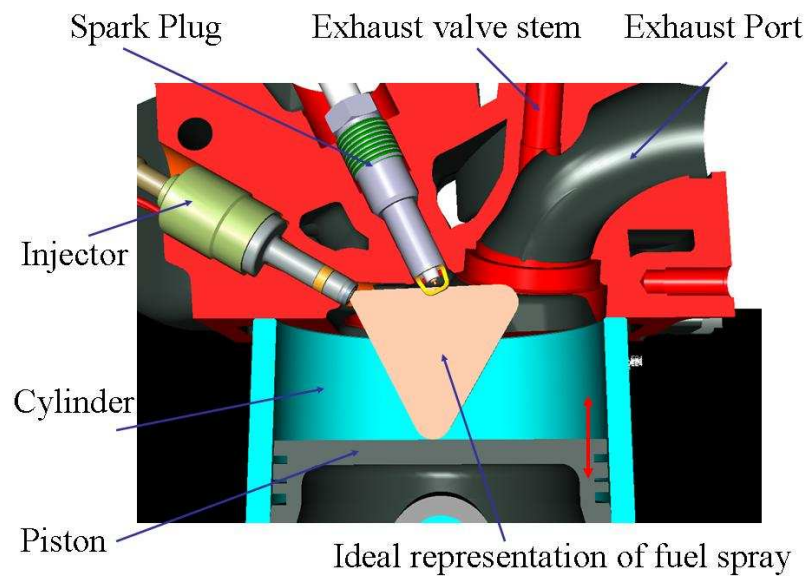


Figure 5.8: (a) Mean axial velocity and (b) rms of axial velocity (b) normalized by the mean piston speed, at crank angle of 144° . Solid lines and dashed lines are LES results obtained by the dynamic and constant coefficient ($C_d = 0.1$) Smagorinsky models, respectively, and symbols are LDA data.



stroke = 106 mm
 bore = 90 mm
 RPM = 2500
 compression ratio = 11 : 1
 Intake valve diameter = 33 mm
 Intake valve Max. lift = 11 mm
 Intake valve tilt angle = 5.6°
 Exhaust valve diameter = 37 mm
 Exhaust valve Max. lift = 12 mm
 Exhaust valve tilt angle = 5.1°

Figure 5.9: Schematic pictures of the MSUs 3-valve DISI engine.

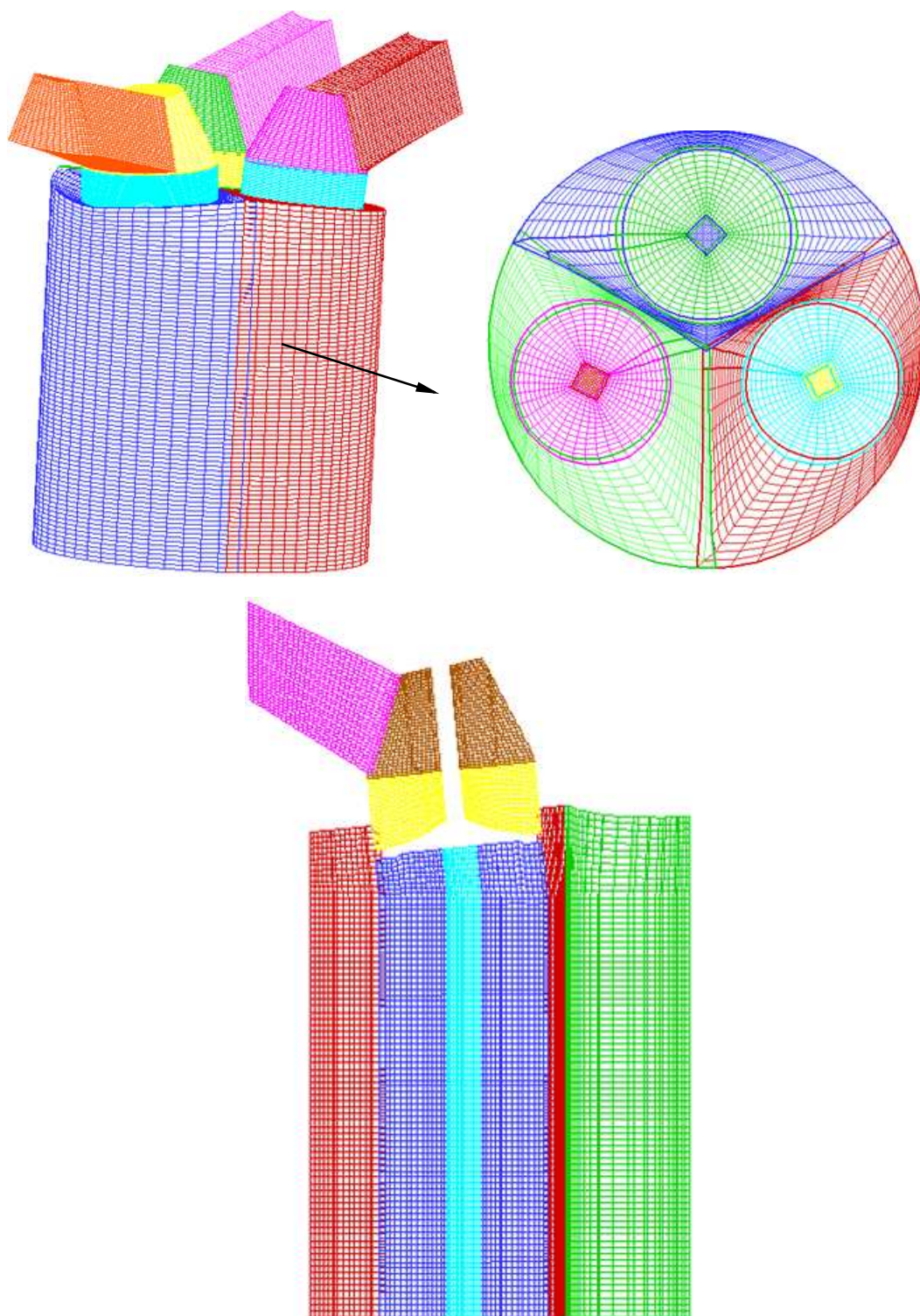


Figure 5.10: Three-dimensional and two-dimensional cross sectional views of the 18-block grid system used for LES of MSUs 3-valve DISI engine.

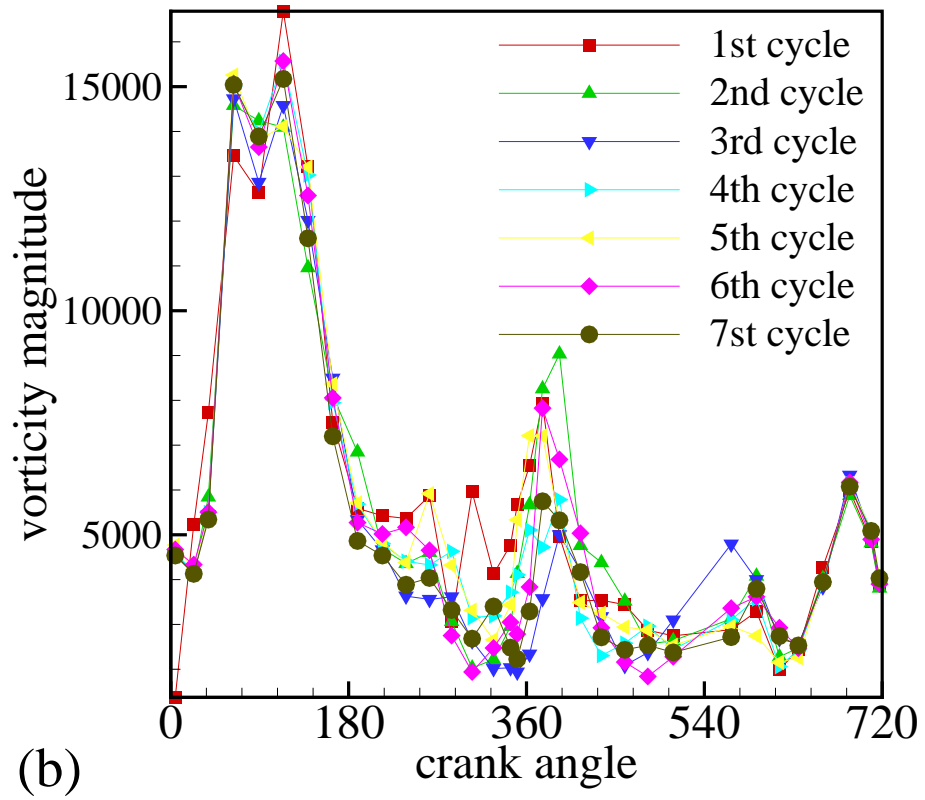
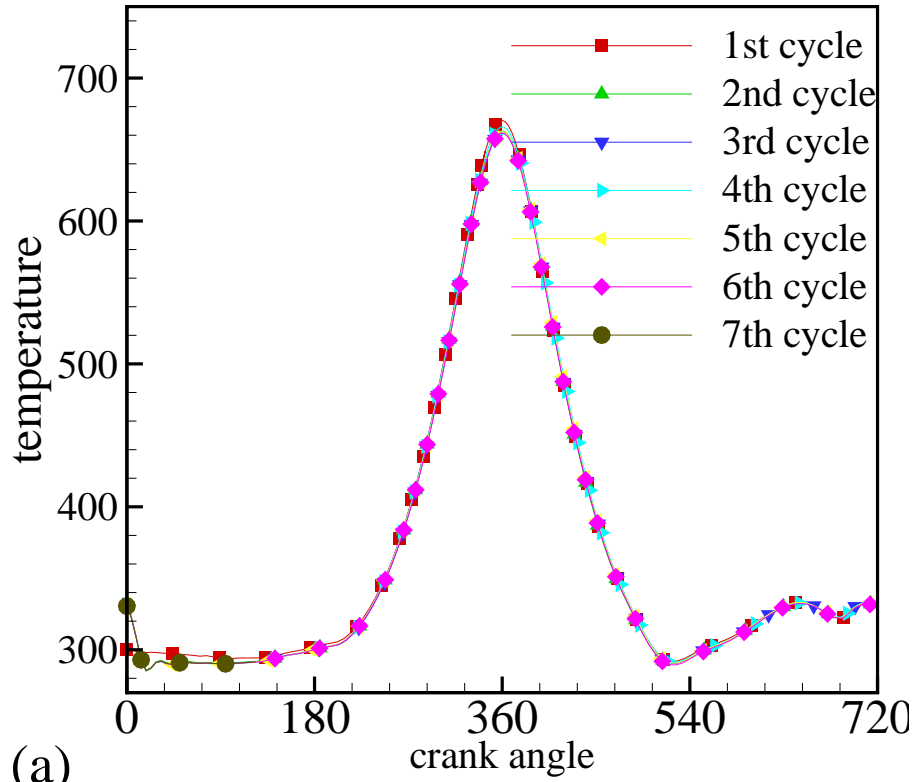


Figure 5.11: Volumetric averaged values of (a) temperature, (b) vorticity and (c) turbulent viscosity at different crank angles and cycles.

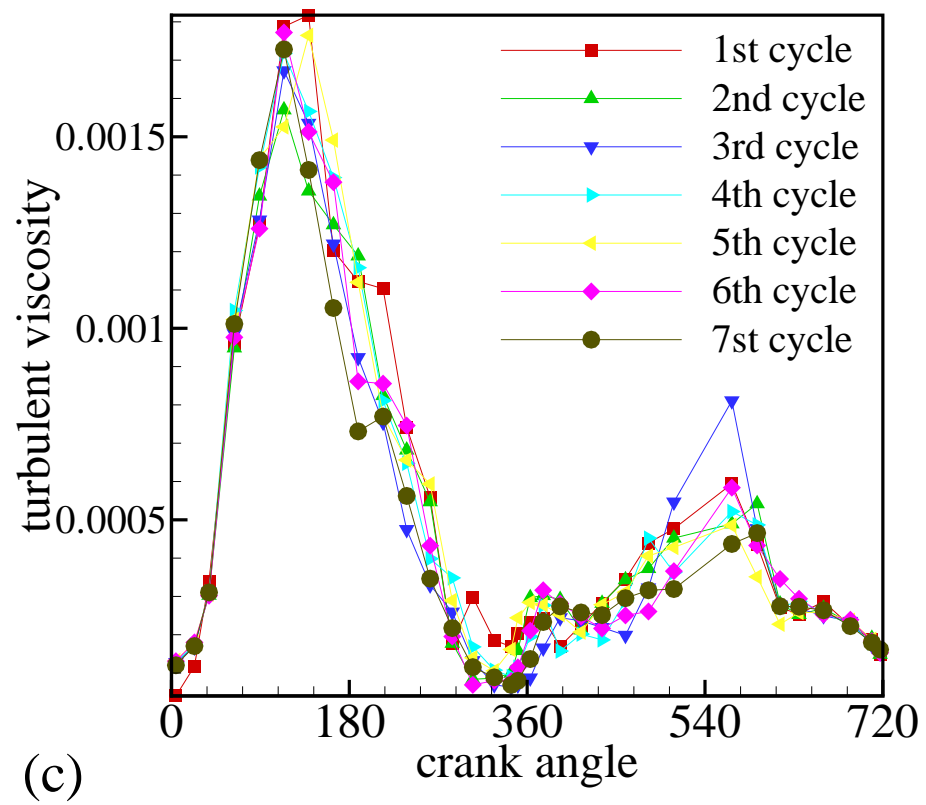


Figure 5.11 continued.

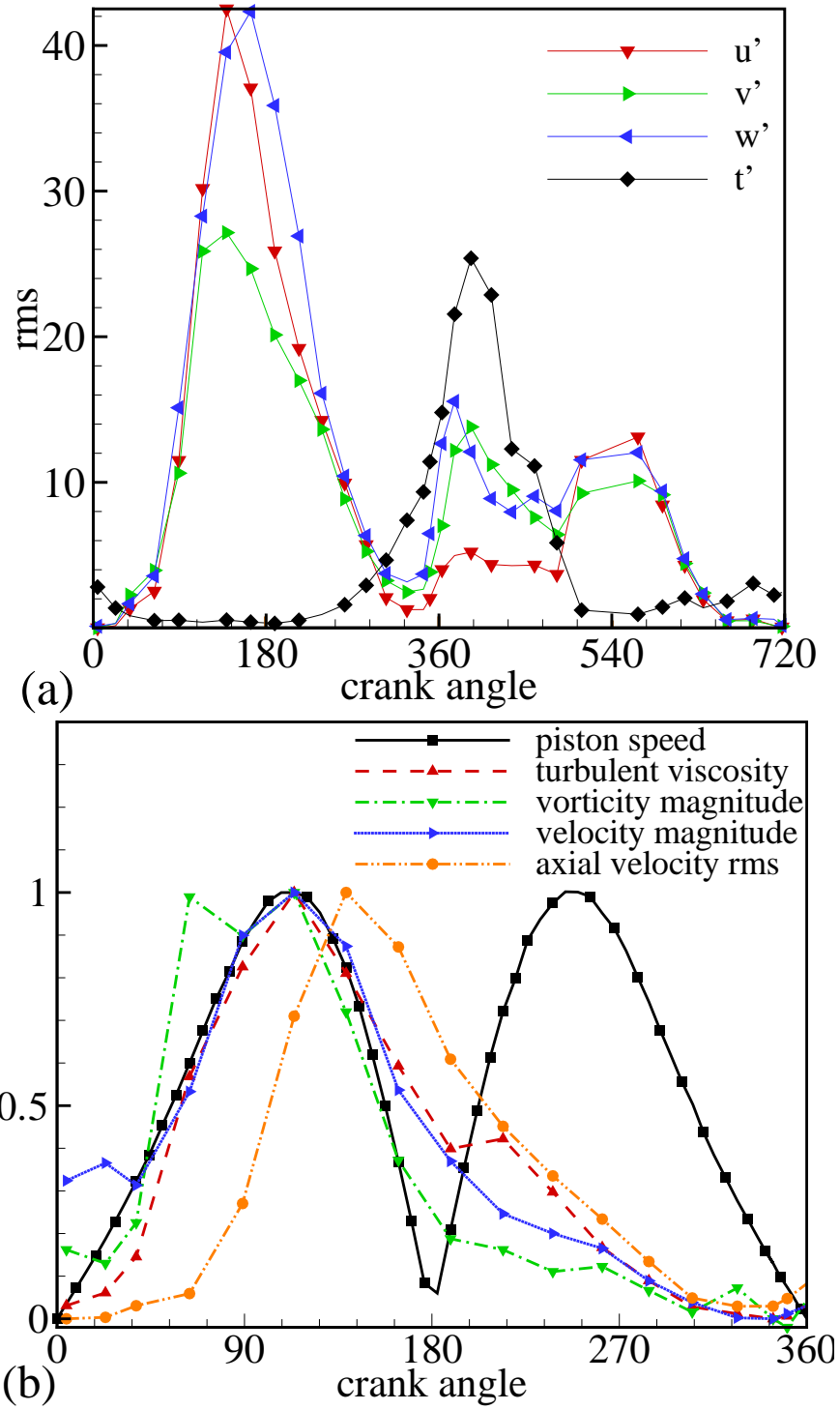


Figure 5.12: Comparison of in-cylinder flow statistics at different crank angles; (a) rms of the three velocity components and temperature, and (b) piston speed, turbulent viscosity, vorticity, velocity magnitude and rms of axial velocity.

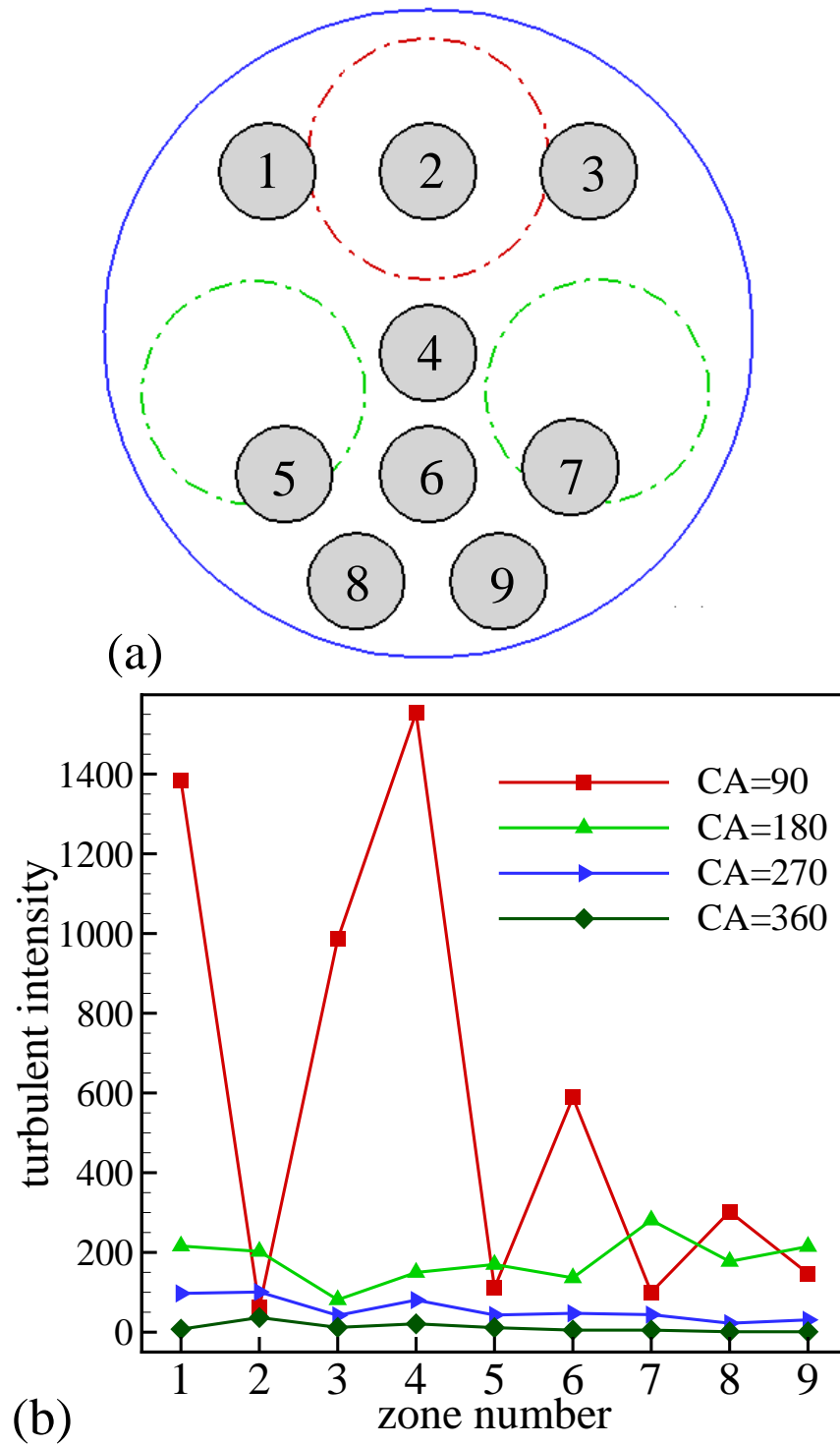


Figure 5.13: (a) Nine different zones or sections inside the cylinder for calculating turbulent intensity, (b) turbulent intensity in 9 special filter at different crank angles.

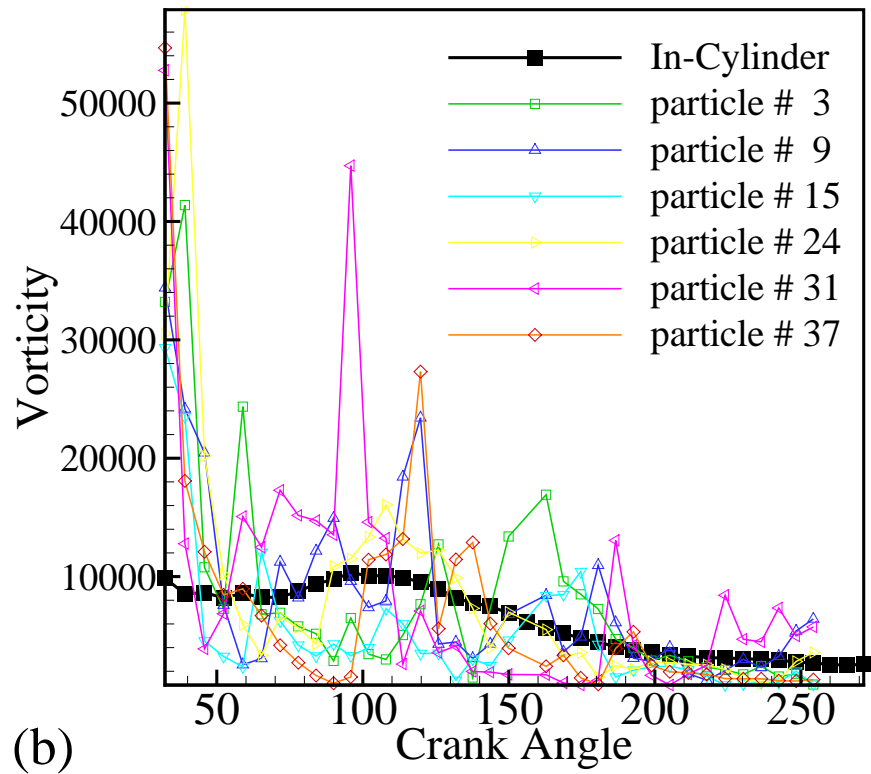
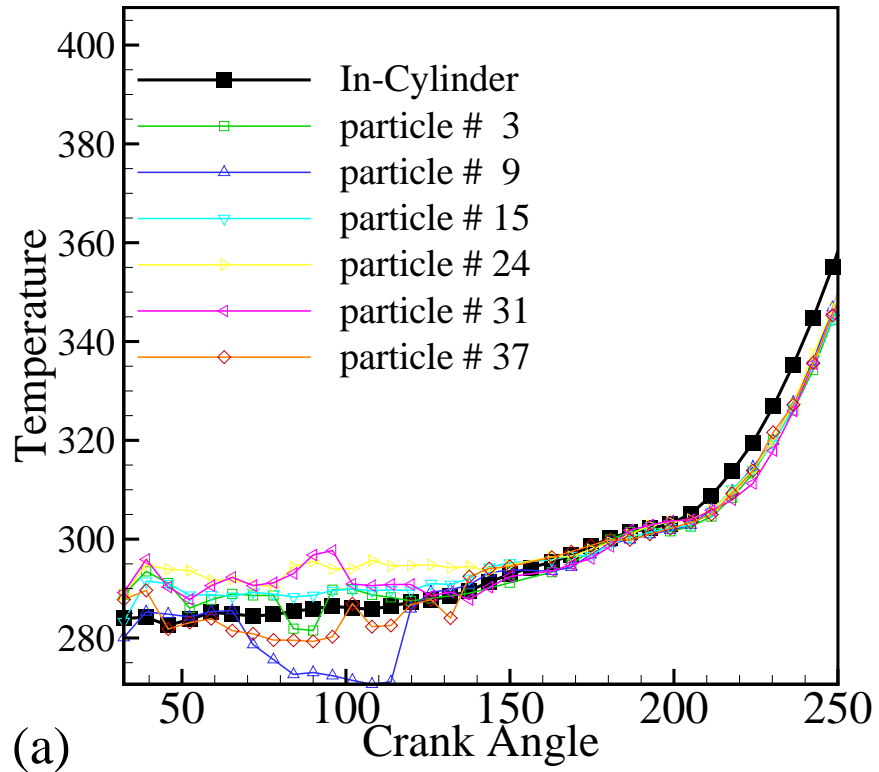


Figure 5.14: (a) Temperature, (b) vorticity , and (c) kinetic energy of several fluid particles traveling in the cylinder during the intake stroke and beginning of compression stroke.

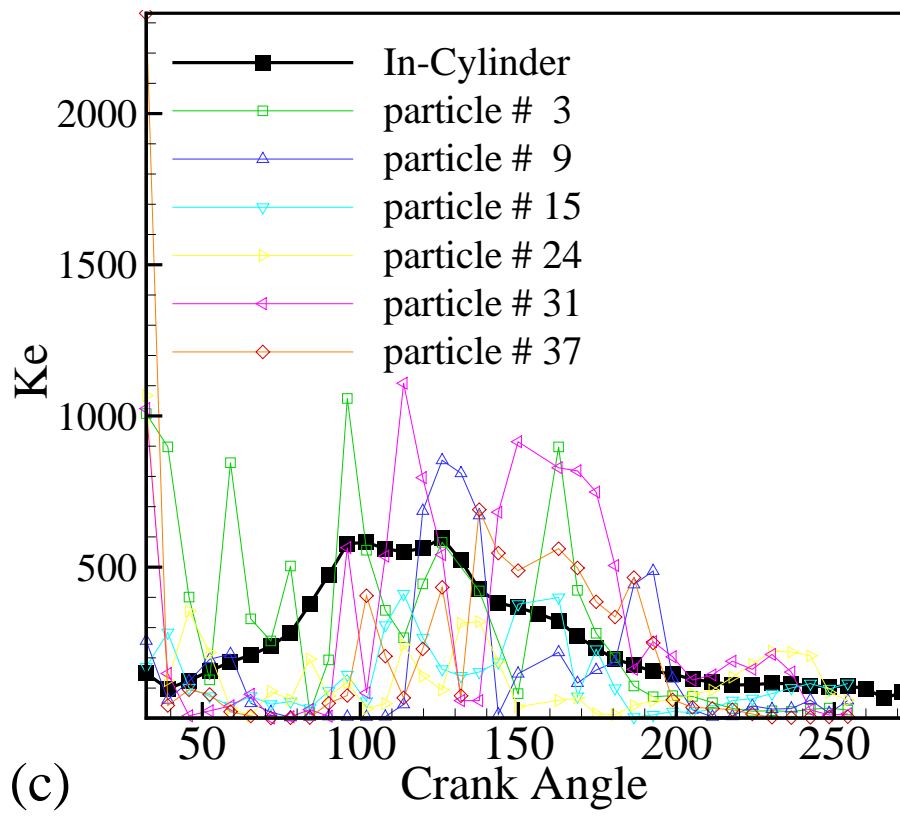


Figure 5.14 continued.

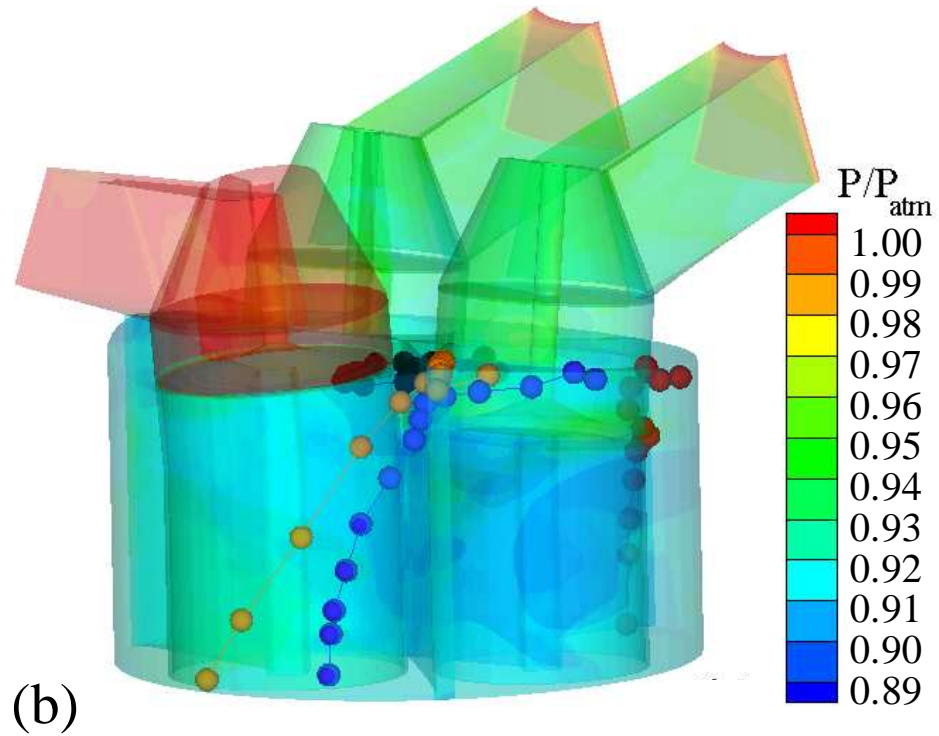
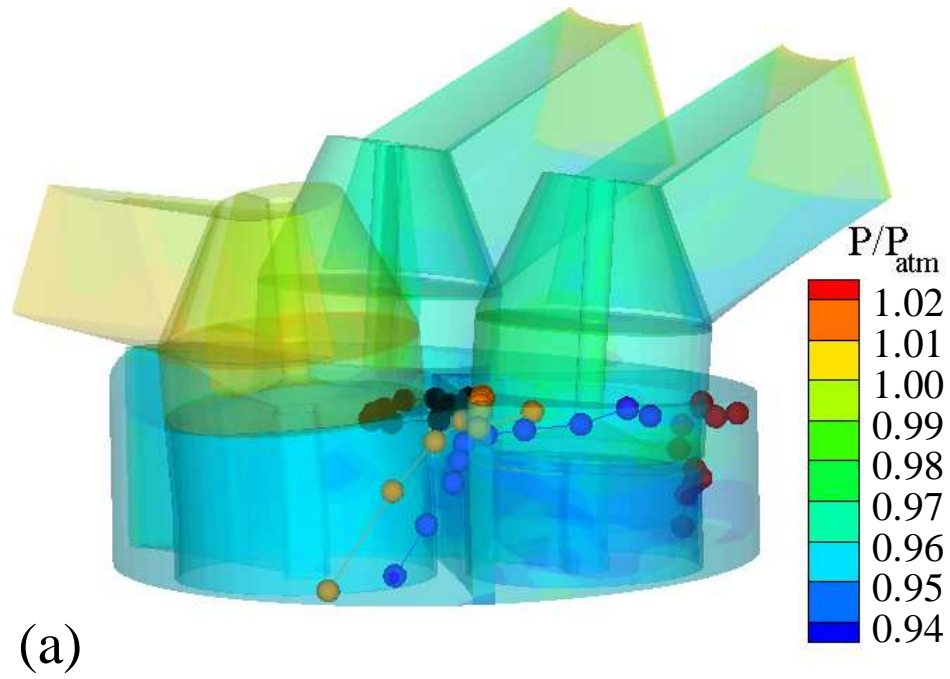


Figure 5.15: Three-dimensional contours of the pressure and several sample Lagrangian particles during the intake at crank angles of (a) 60° , (b) 90° and (c) 180° .

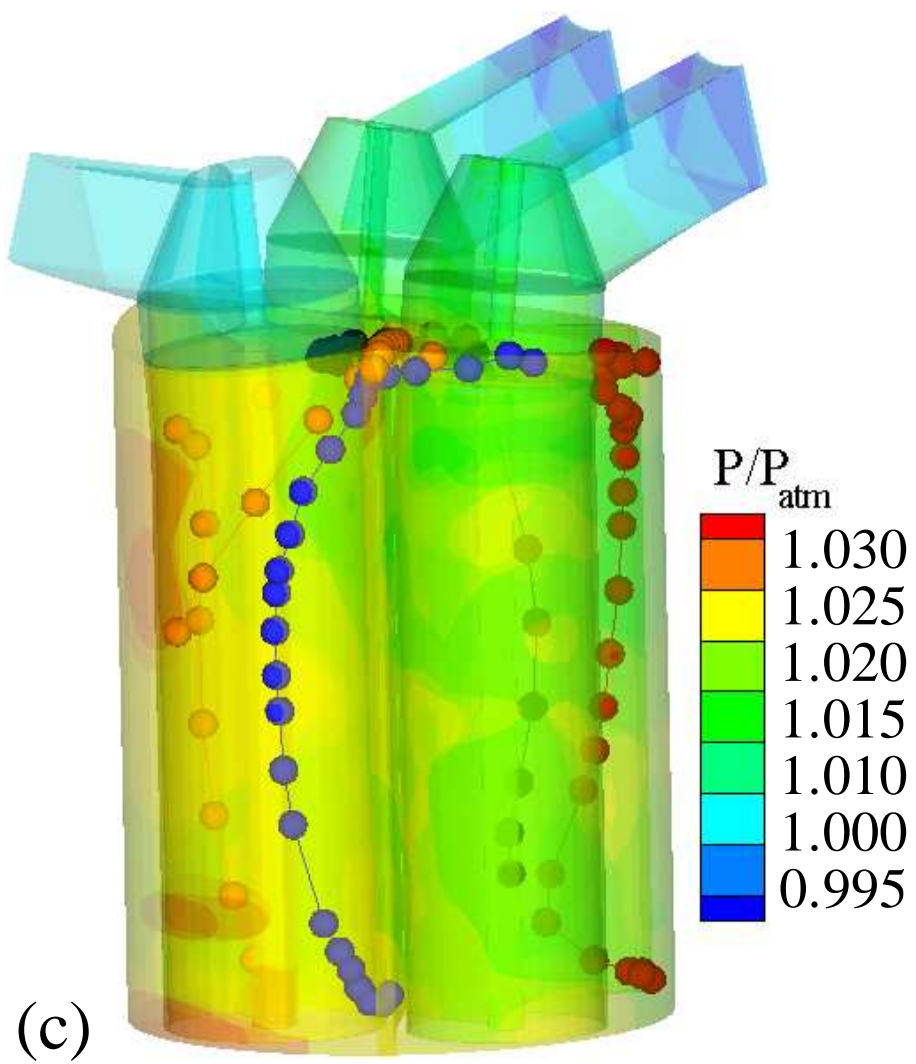


Figure 5.15 continued.

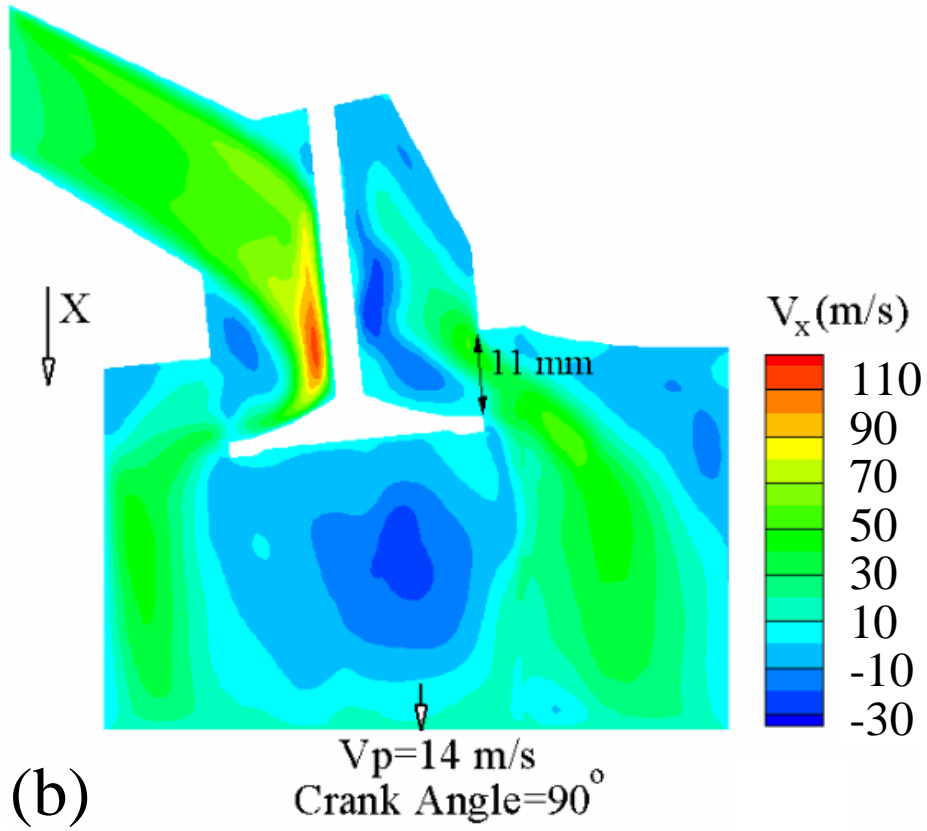
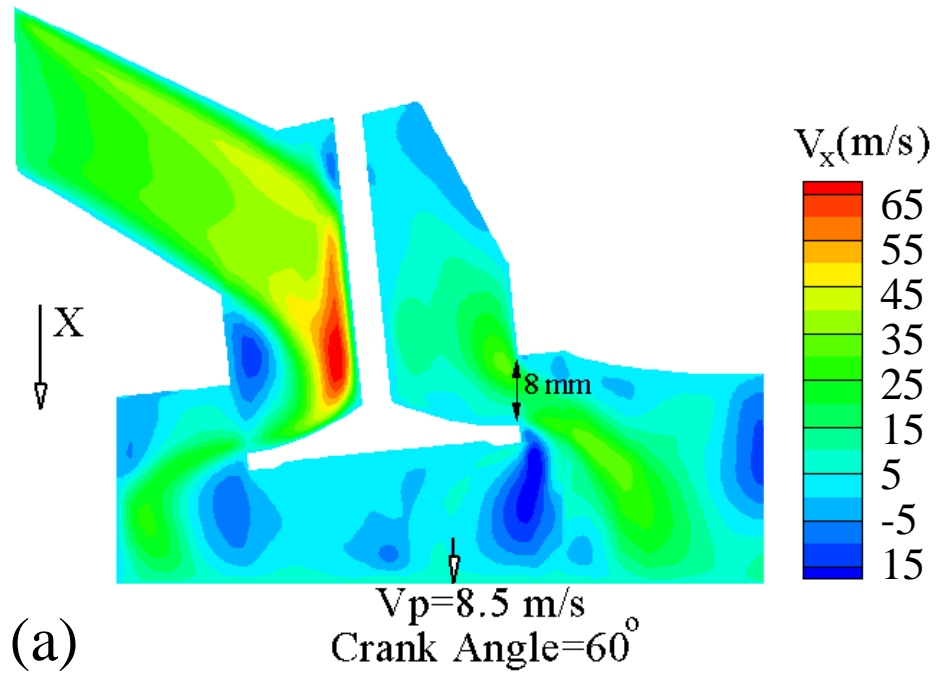


Figure 5.16: Two-dimensional contours of the axial velocity during the intake at crank angles of (a) 60° , (b) 90° and (c) 180° .

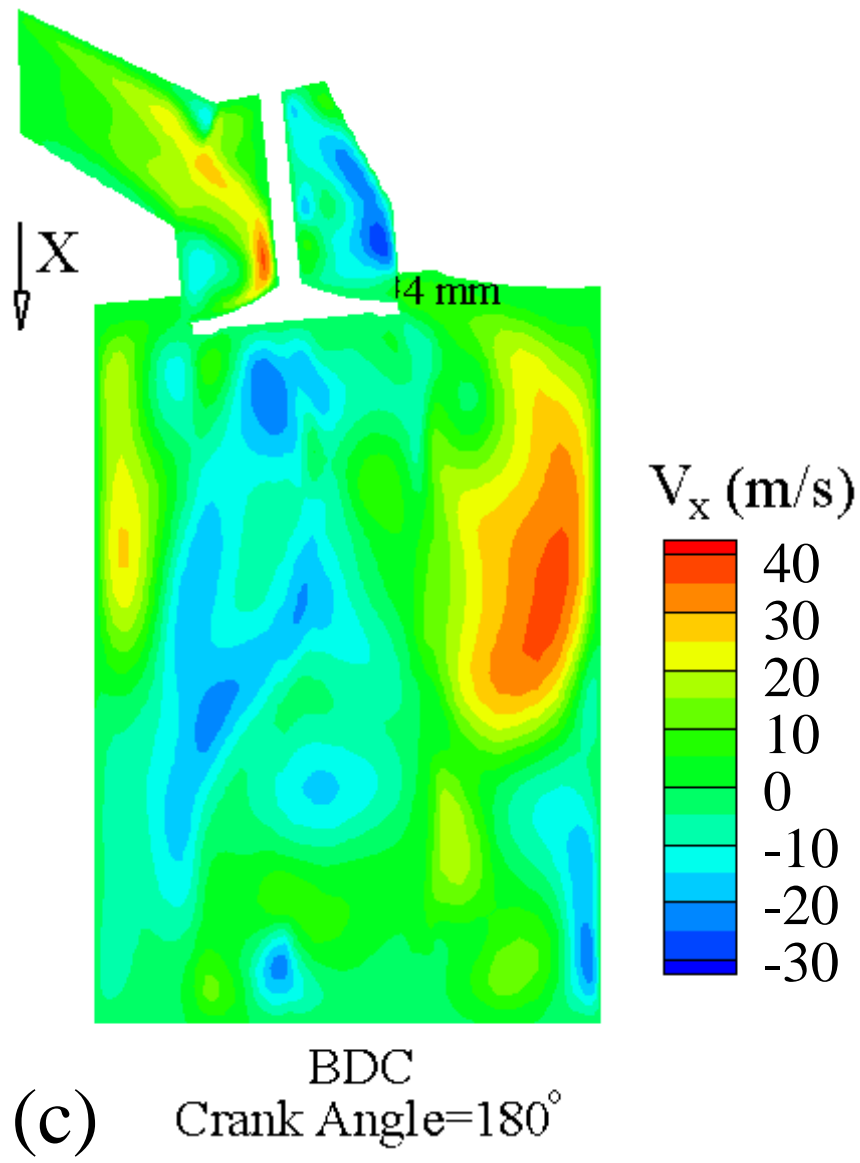


Figure 5.16 continued.

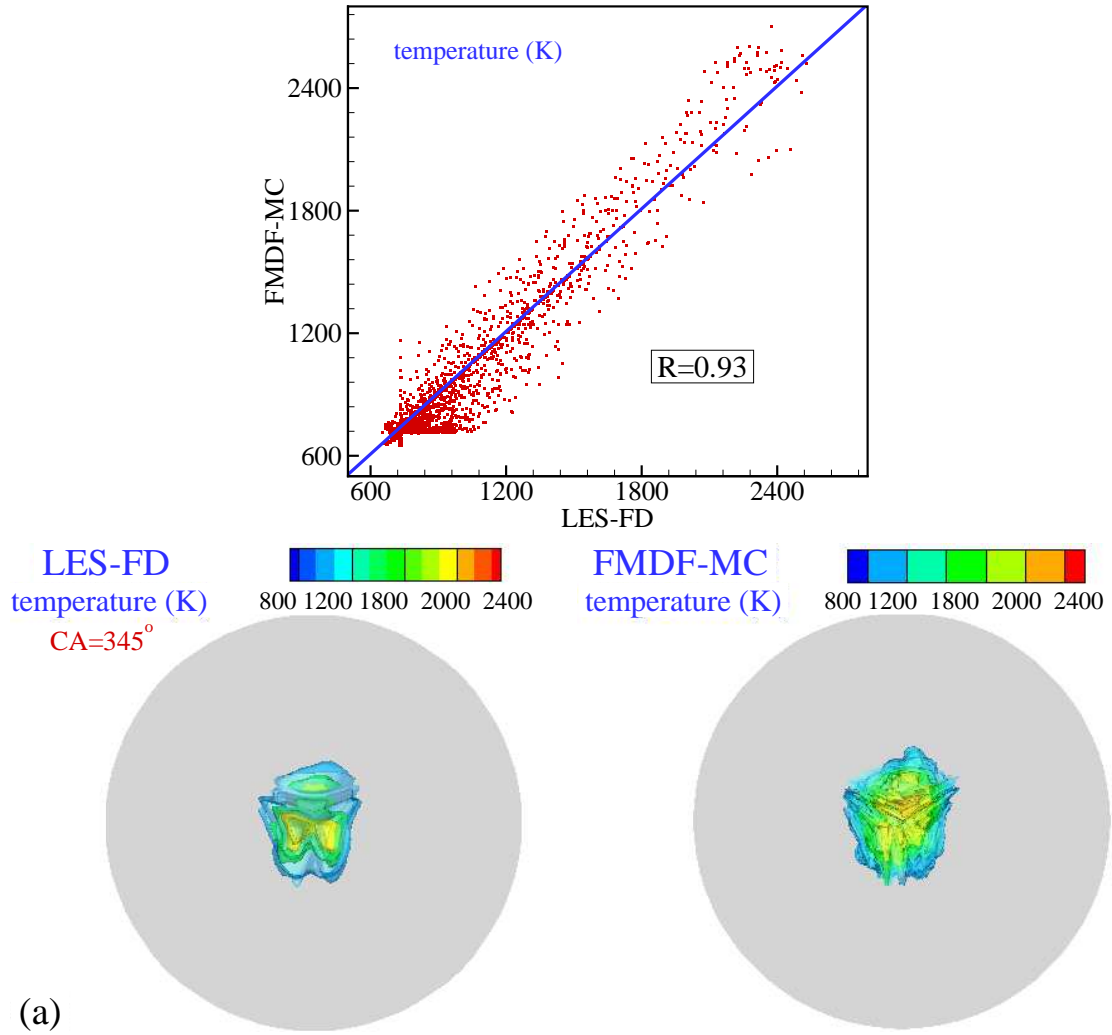


Figure 5.17: Scatter plots and iso-levels of temperatures as predicted by LES-FD and FMDF-MC during the flame propagation in the DISI engine at crank angle (a) 345° , (b) 355° and (c) 365° .

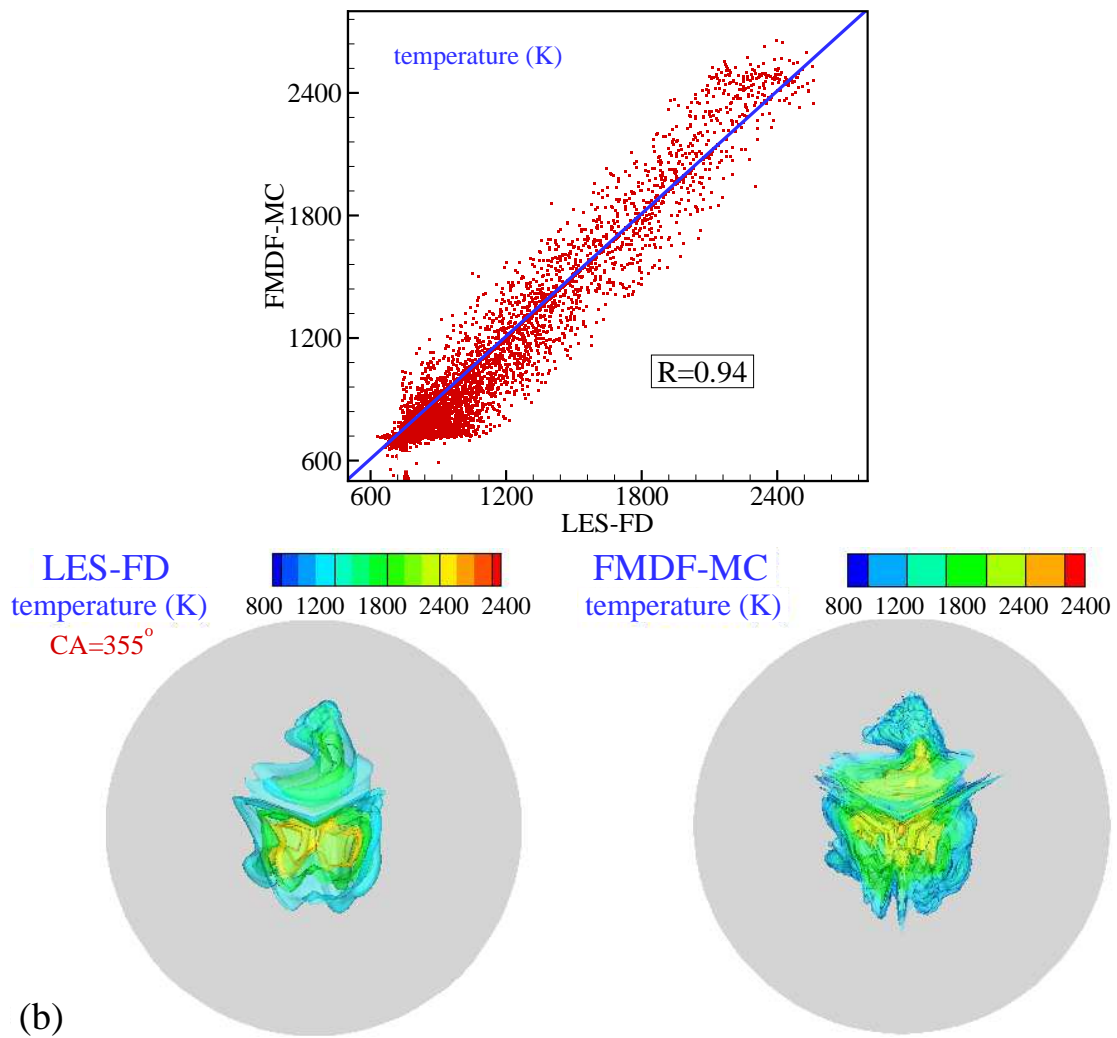


Figure 5.17 continued.

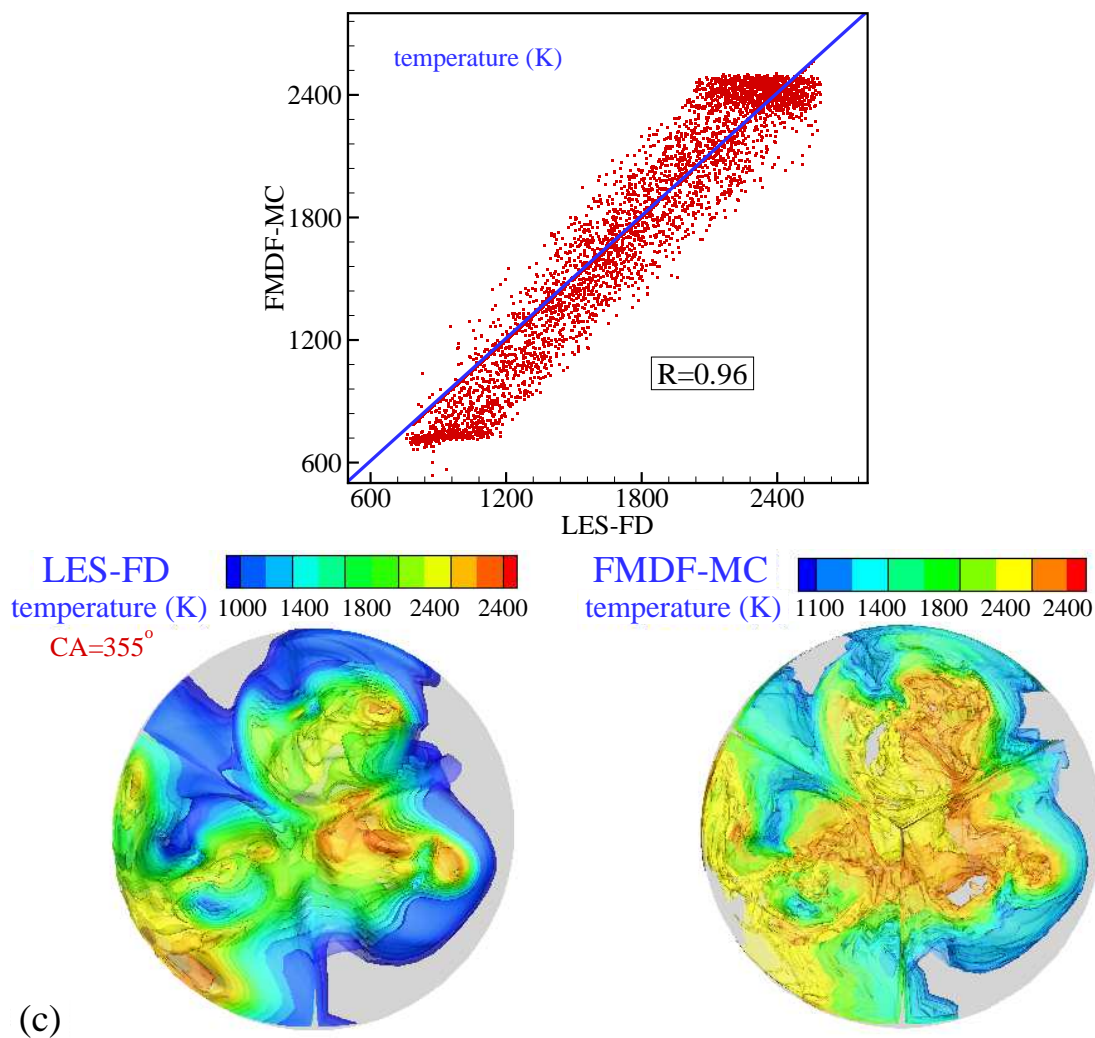


Figure 5.17 continued.

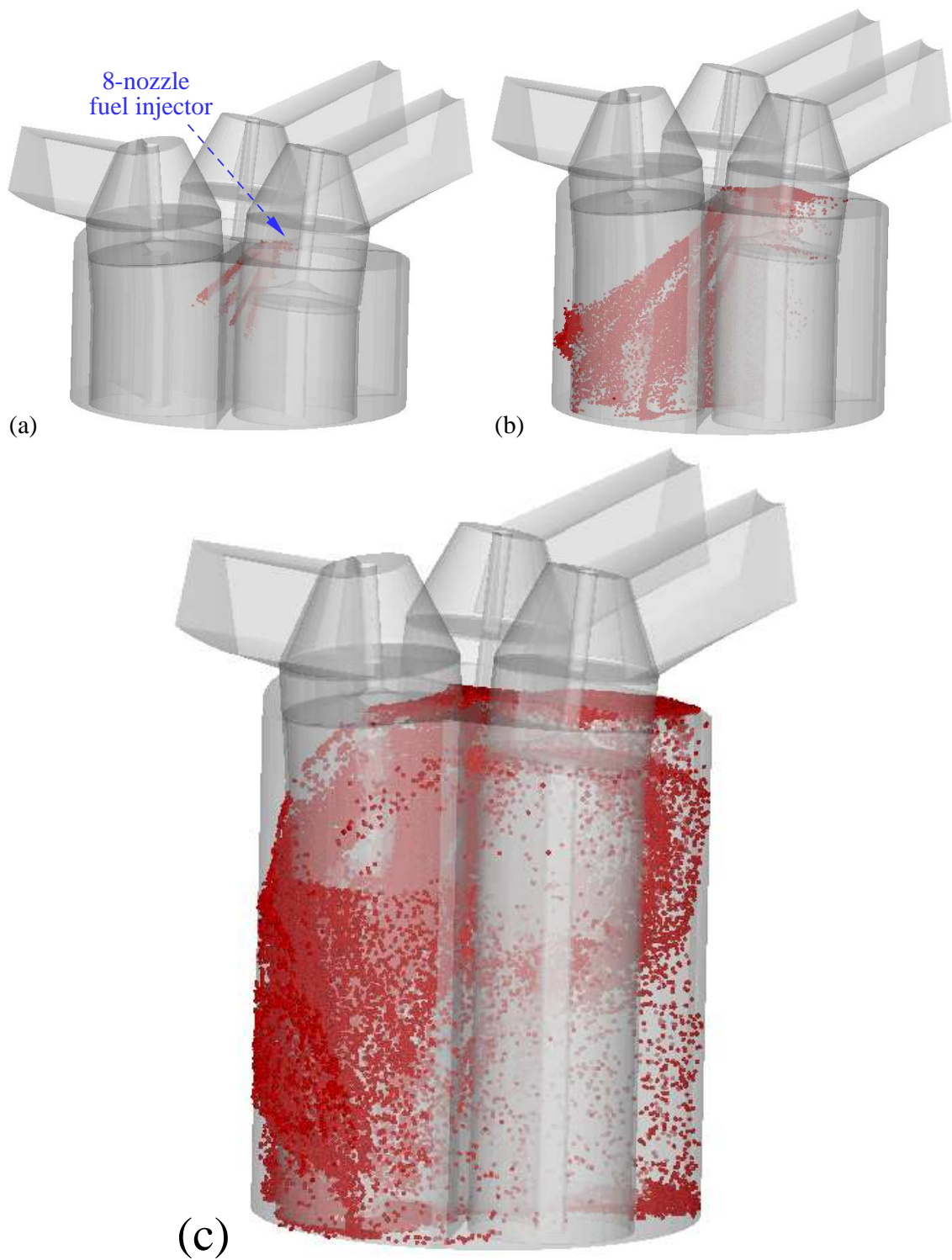


Figure 5.18: Fuel droplets' pattern during the intake at crank angles of (a) 84° , (b) 100° and (c) 148° .

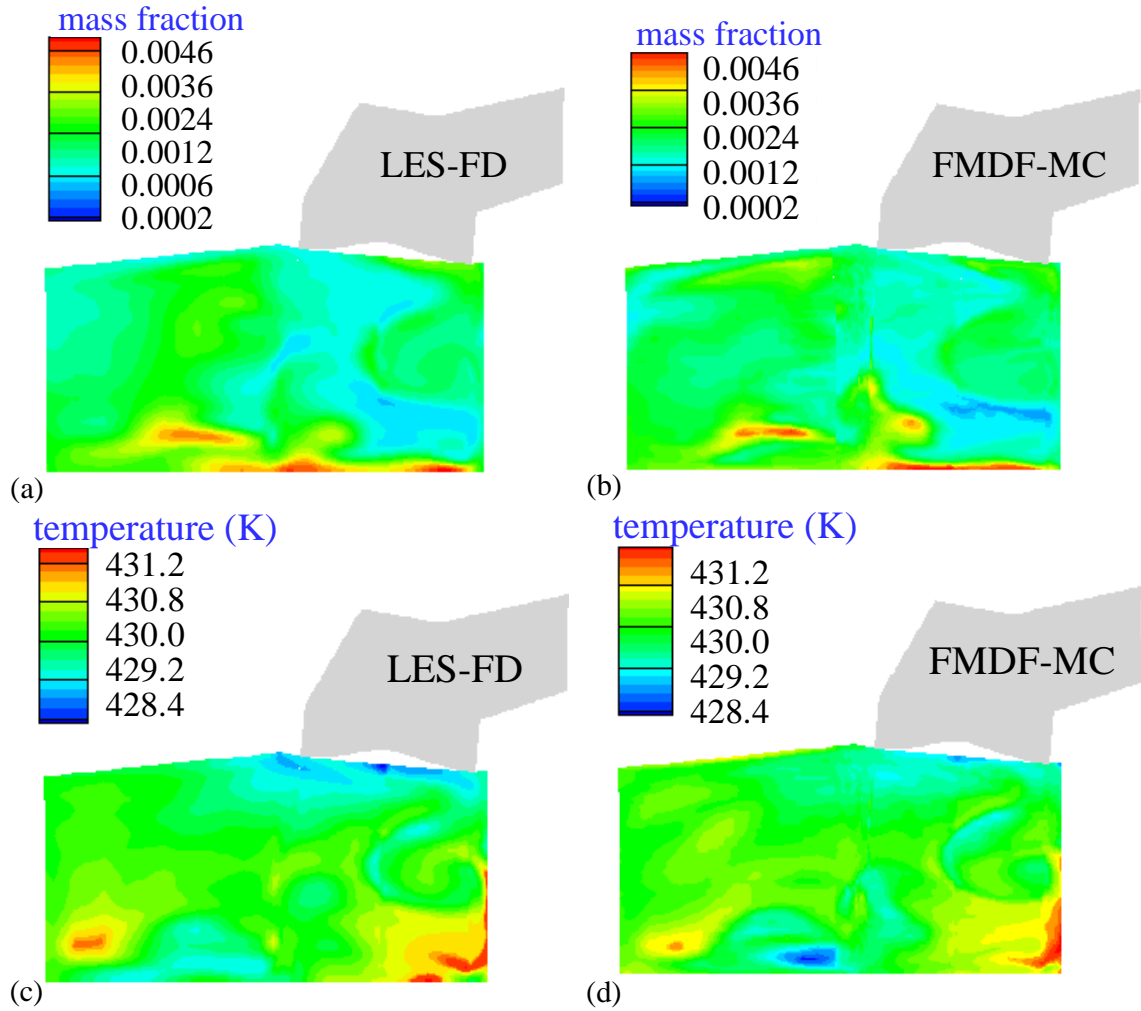


Figure 5.19: Instantaneous contour plots of evaporated fuel mass fraction predicted by (a) LES-FD and (b) FMDF-MC, and temperature contour plots predicted by (c) LES-FD and (d) FMDF-FD, when the crank angle is 270° .

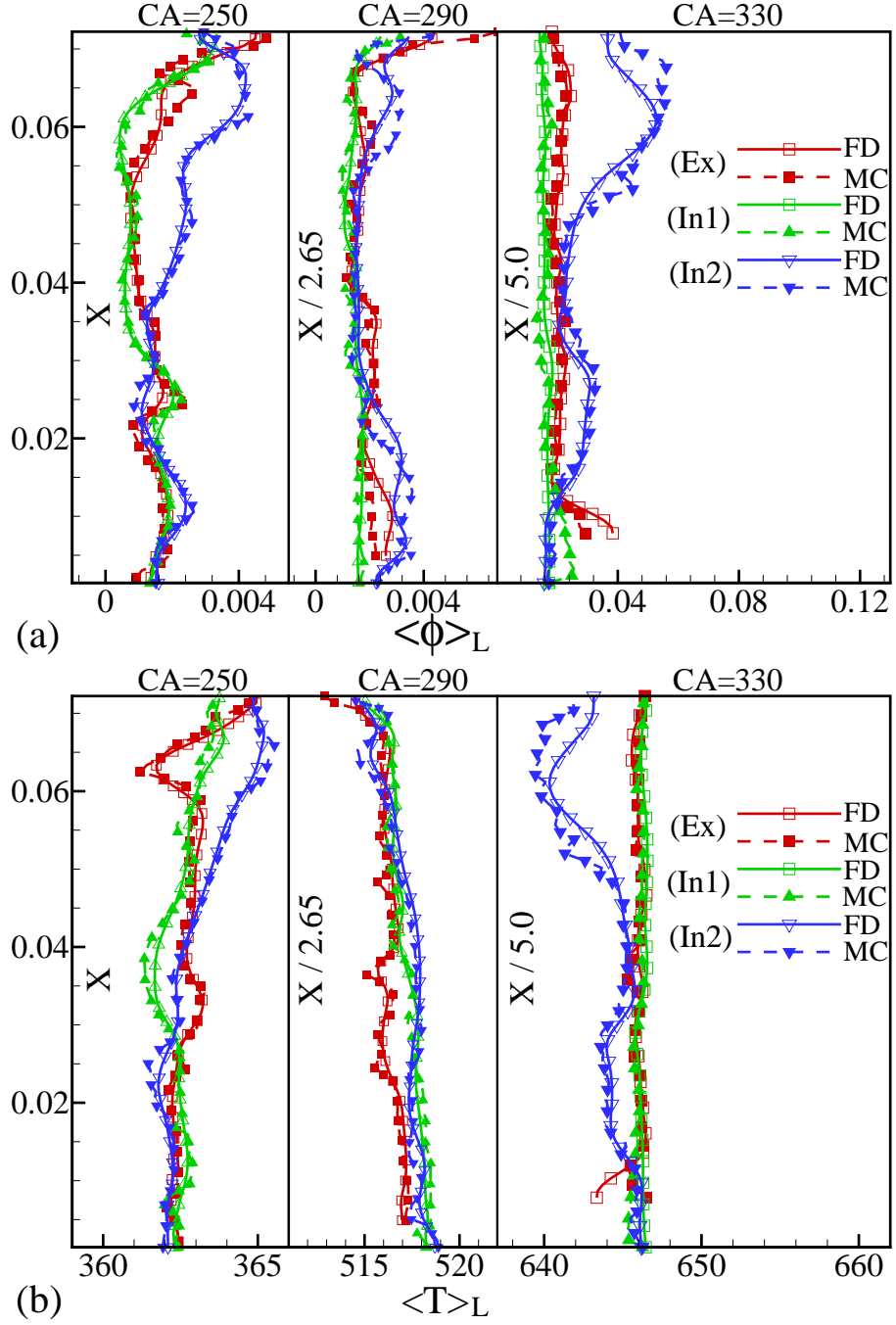


Figure 5.20: Consistency of LES-FD and FMDF-MC for (a) evaporated fuel mass fraction and (b) temperature during the compression at crank angles of 250° , 290° and 330° along the three line connecting the exhaust (Ex), and two intake (In1, In2) valve to the piston.

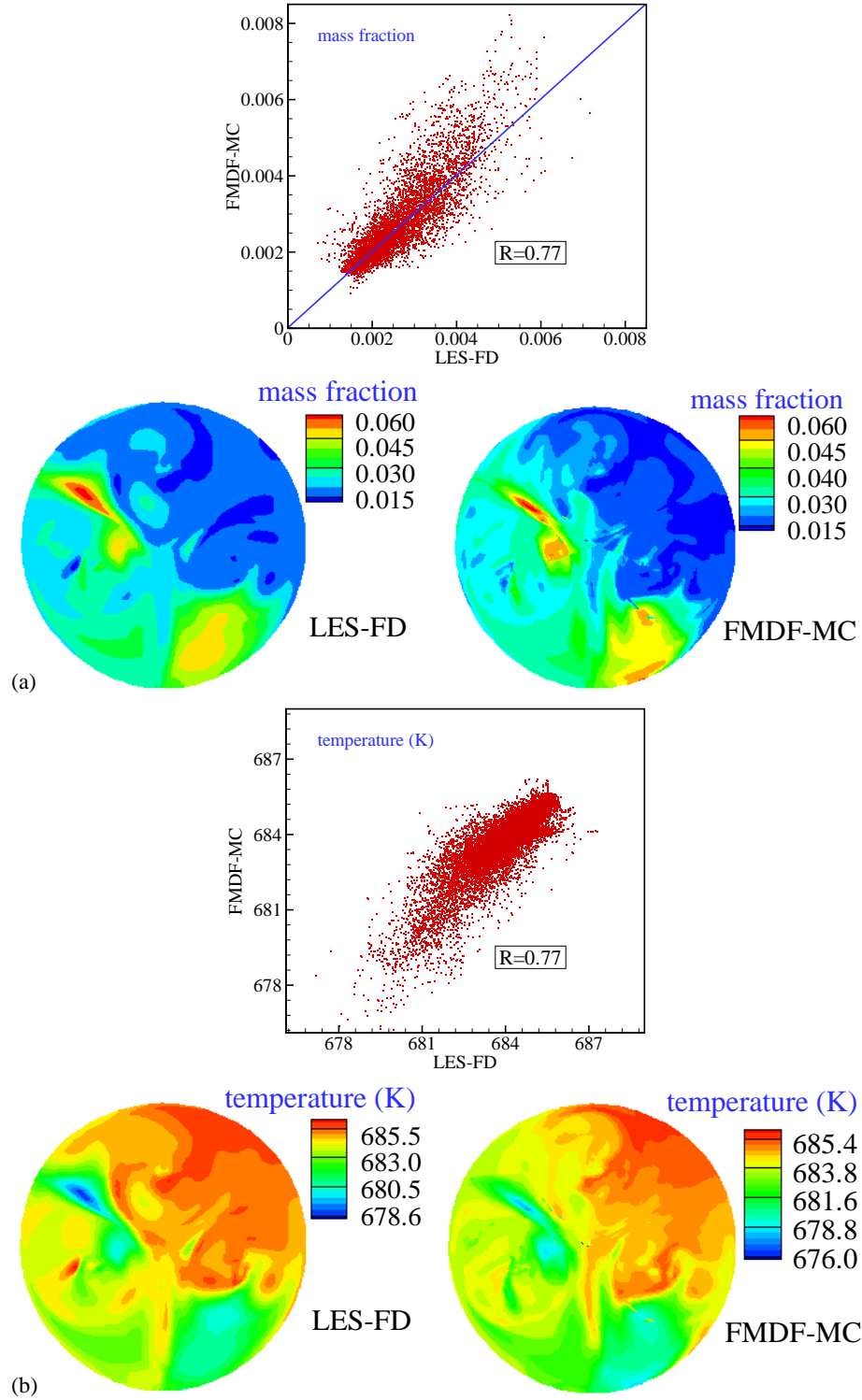


Figure 5.21: Scatter plots and instantaneous contour plots of evaporated fuel mass fraction predicted by (a) LES-FD and (b) FMDF-MC, and temperature contour plots predicted by (c) LES-FD and (d) FMDF-FD, at the crank angle of 335° before ignition.

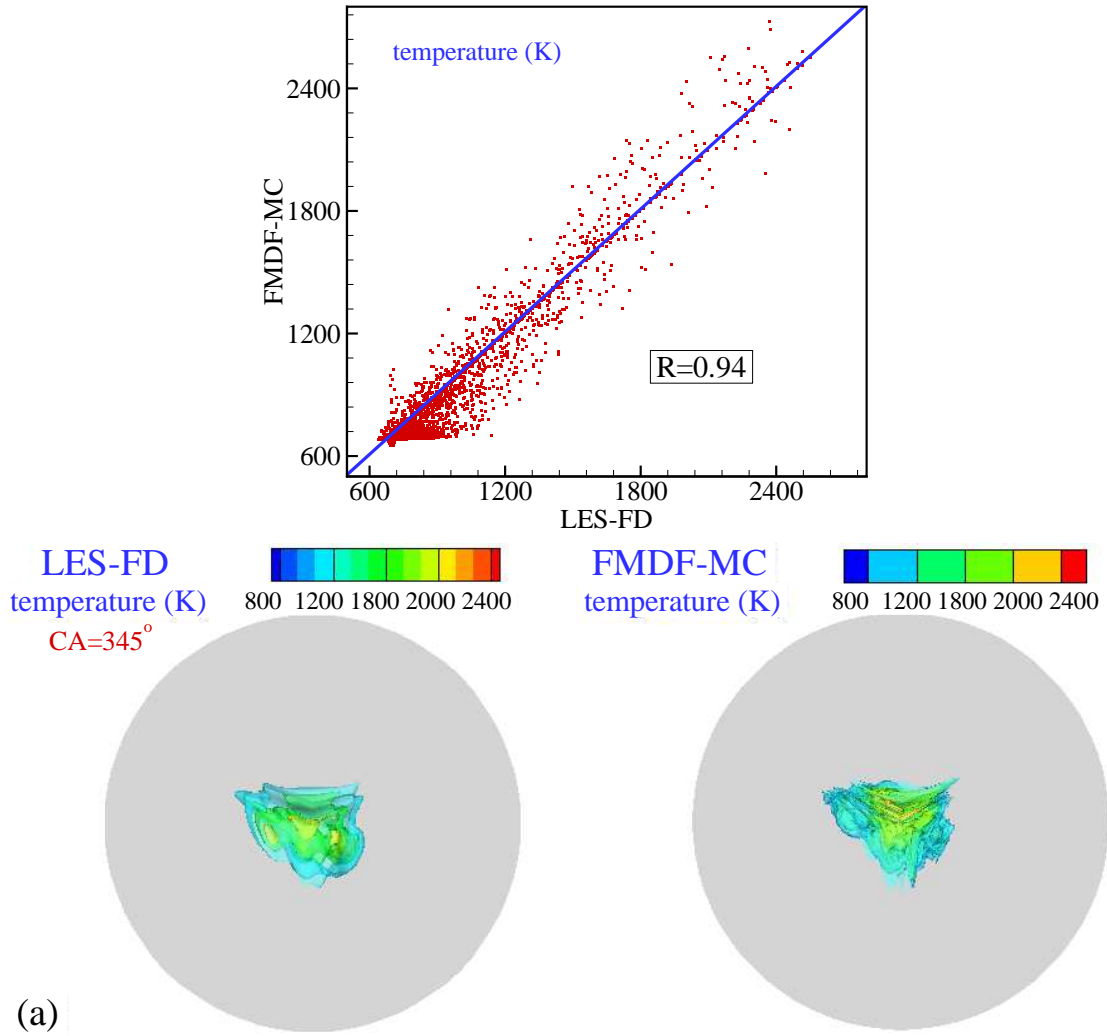


Figure 5.22: Scatter plots and iso-levels of temperatures as predicted by LES-FD and FMDF-MC during the flame propagation in the DISI engine at crank angle (a) 345° , (b) 355° and (c) 365° .

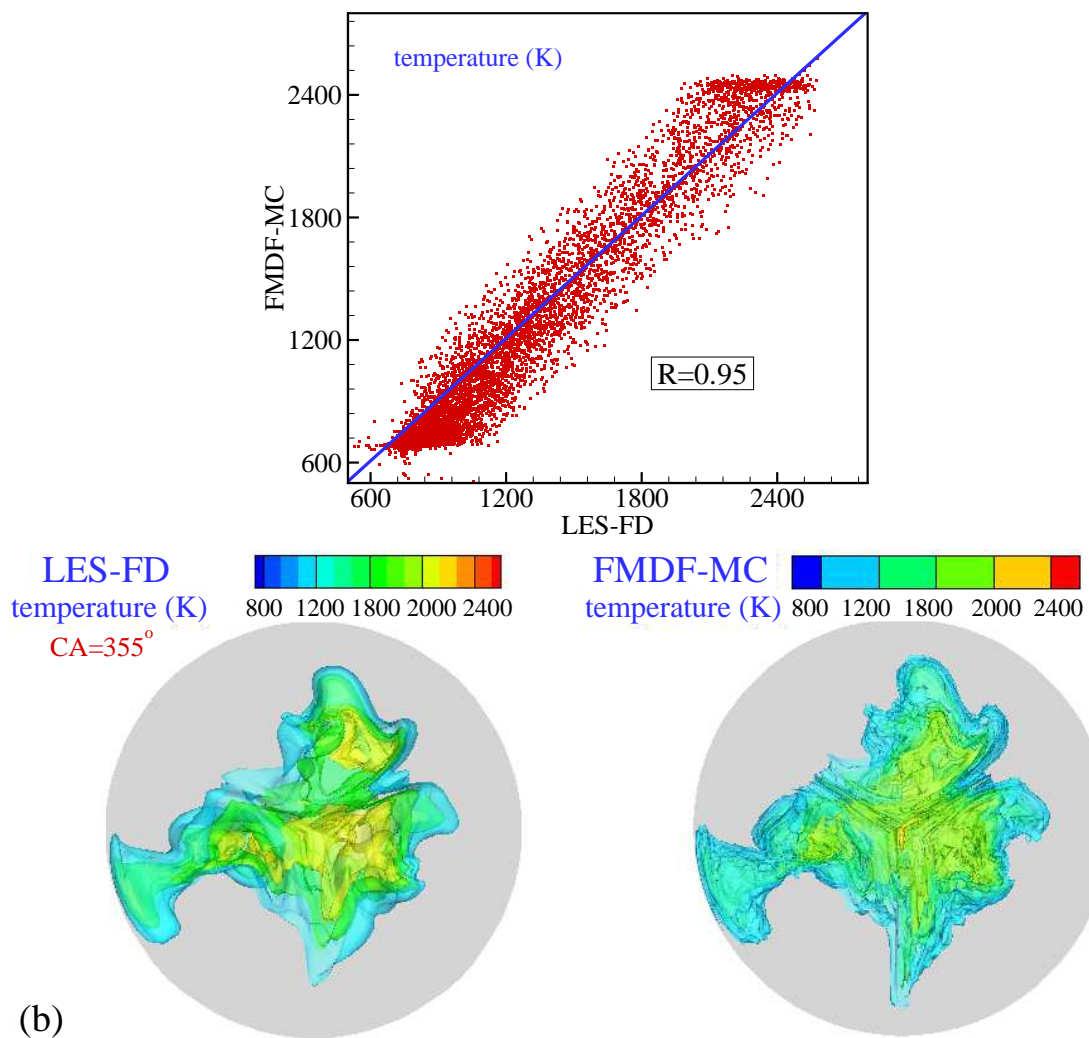


Figure 5.22 continued.

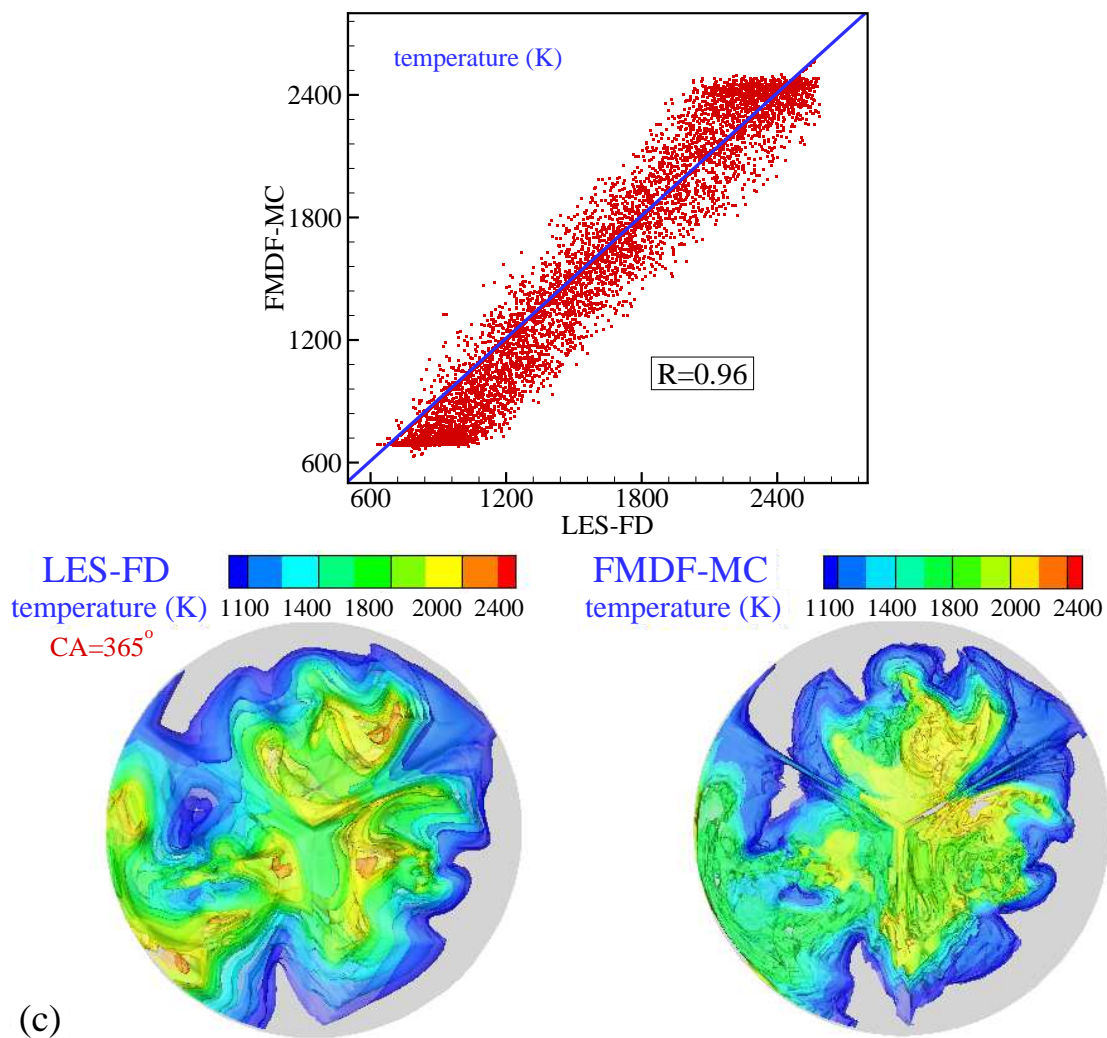


Figure 5.22 continued.

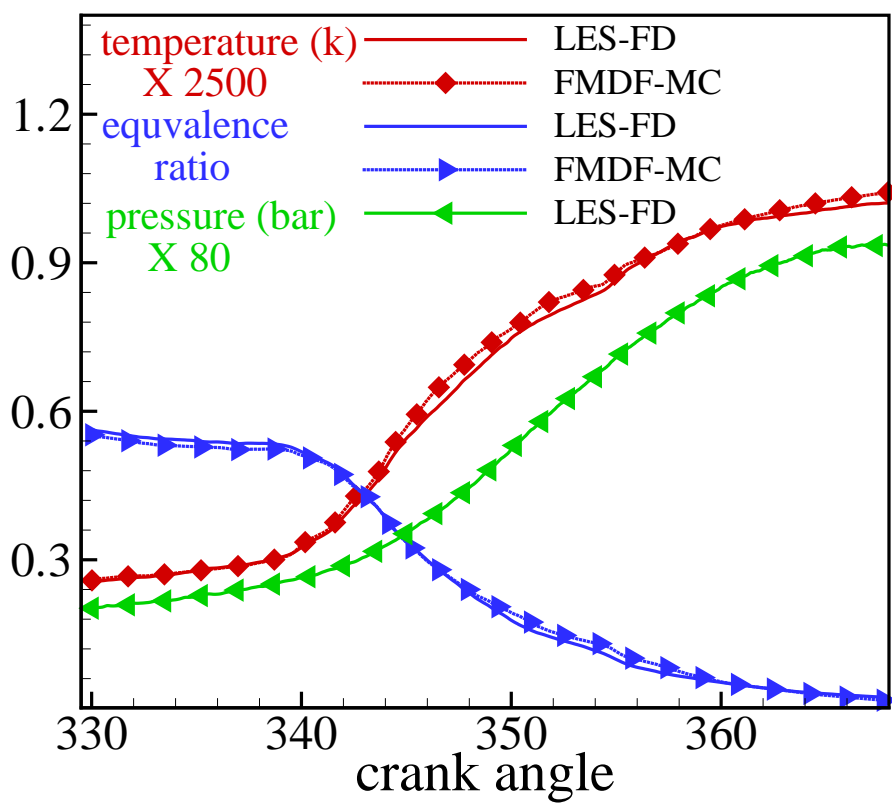


Figure 5.23: Volume-averaged values of temperature, equivalence ratio and pressure as predicted by LES-FD and FMDF-MC.

Chapter 6

Summary and conclusions

To simulate and to understand the fluid dynamics, the spray and the combustion in internal combustion (IC) engines, a high fidelity turbulent spray combustion model based on large-eddy simulations (LES) approach is developed. Spray and combustion are conducted with the two-phase filtered mass density function (FMDF) which is the subgrid scale (SGS) probability density function. Compressibility effect is included in the FMDF formulation by adding the pressure terms to the FMDF energy equation. A hybrid finite difference-Monte Carlo (FD-MC) method is employed for the solution of LES and FMDF equations. For spray simulations, Lagrangian equations for the position, velocity, temperature and mass of individual droplets are solved together with the LES and FMDF equations. A new Lagrangian-Eulerian-Lagrangian computational methodology is employed. By simulating several compressible subsonic and supersonic flows, it has been shown that the new compressible scalar FMDF model can very well handle the effect of pressure on the FMDF and MC particles. The accuracy and the consistency of the temperature values predicted by the FMDF-MC and the LES-FD parts of the hybrid LES-FMDF solver is dependent on the inclusion of pressure effect in the FMDF (energy) equation.

The fluid flow and heat transfer inside a rapid compression machine is simulated

by the LES-FD and FMDF-MC. It was shown that the isothermal wall condition can be implemented in the FMDF-MC by interpolating the LES-FD temperature values in the boundary cells to the corresponding MC particles. It is concluded that the thermodynamic values inside the RCM is more uniform when a crevice piston is employed.

The fuel spray characteristics and parameters affecting the fuel mixing is also studied in a stagnant environment. It is shown that by increasing the initial ambient gas temperature and gas density the liquid jet penetration decrease. However, by increasing the injector nozzle diameter the penetration depth becomes longer. It is also shown that the injector pressure does not have a significant effect on the penetration length. For the reacting sprays, it is observed that by increasing the gas phase temperature, the flame lift-off height decreases.

Cycle-to-cycle variations (CCV) of the flow in the cylinder was studied by conducting LES of non-reacting flows inside a simple cylinder with a harmonically moving piston and a three-valve direct-injection spark-ignition (DISI) engine. LES results, consistent with the experimental results, showed that the CCV in the thermodynamic variables is not significant but the velocity field exhibits substantial CCV. Also by calculating the turbulent intensity within the specific zones at different crank angles and by following the pathlines of sample fluid particles, it was found that the flow during the intake stroke is highly turbulent and inhomogeneous. Nevertheless, turbulence decays after the mid-intake due to piston deceleration and particularly during the compression stroke when intake valves are closed. The in-cylinder flow becomes nearly homogeneous at the end of compression stroke.

Using the new two-phase compressible LES/FMDF method, gaseous fuel (single-phase) combustion and spray combustion inside the DISI engine are simulated. Ignition was initiated by an energy source term model in the FMDF-MC energy equation. Consistency of LES-FD and FMDF-MC temperature and fuel mass fraction values

during the compression, fuel evaporation, ignition and flame propagation periods are established. Unlike the non-reacting flow, the evaporation of fuel droplets make the in-cylinder flow inhomogeneous at the end of compression stroke. It is shown that the flame propagation takes about 30 crank angle.

The main conclusions of this work are:

- ▷ Two-phase LES/fMDF is a robust and efficient mathematical/numerical methodology for two-phase turbulent reacting flows in complex flow configurations.
- ▷ The numerical results compare well with the experimental data. ▷ The consistency of LES-FD and FMDF-MC temperatures are dependent on the inclusion of pressure in the FMDF formulation.
- ▷ Isothermal wall condition in the FMDF-MC can be achieved by interpolating the LES-FD temperatures to the MC particles in the boundary cells.
- ▷ In turbulent mixing simulation, mixing layer grows faster with the MKEV model than with the constant coefficient Smagorinsky model.
- ▷ LES is able to predict the cycle-to-cycle variations in the IC engines.
- ▷ The in-cylinder flow in IC engines during the intake stroke is highly turbulent and inhomogeneous. However, the turbulent decays during the compression stroke and the flow becomes relatively homogeneous at the end of compression.
- ▷ In the RCM, more uniform in-cylinder temperature can be obtained by employing the crevice piston.
- ▷ In the spray simulations, the gas phase temperature and density and the nozzle diameter have significant effect on the liquid penetration. However, the injection pressure effect is not significant.

Bibliography

- [1] Aldama, A. A., "Filtering Techniques for Turbulent Flow Simulations," *Lecture Notes in Engineering*, Vol. 49, SpringerVerlag, New York, 1990.
- [2] Visbal, M. R., and Gaitonde, D., "On the Use of Higher-Order Finite-Difference Schemes on Curvilinear and Deforming Meshes," *Journal of Computational Physics*, Vol. 181, 2002, pp. 155-185.
- [3] Visbal, M. R., and Rizzetta, D. P., "Large-eddy simulation on curvilinear grids using compact differencing and filtering schemes," *ASME Journal of Fluid Engineering*, Vol. 124, 2002, pp. 836-847.
- [4] Afshari, A., Jaber, F. A., and Shih, T. I-P., "Large-eddy simulations of turbulent flows in an axisymmetric dump combustor," *AIAA Journal*, Vol. 46, No. 7, 2008, pp. 1576-1592.
- [5] Rizzetta, D. P., Visbal, M. R., and Morgan, P. E., "A high-order compact finite-difference scheme for large-eddy simulation of active flow control," *Progress in Aerospace Sciences*, Vol. 44(6), 2008, pp. 397-426.
- [6] Smagorinsky, J., "General Circulation Experiments with the Primitive Equations. 1. The Basic Experiment," *Monthly Weather Review*, Vol. 91(3), 1963, pp. 99-164.
- [7] Yoshizawa, A., Statistical Theory for Compressible Turbulent Shear Flows, with the Application to Subgrid Modelling, *Physics of Fluids*, Vol. 29, No. 7, 1986, pp. 2152-2164.
- [8] Germano, R., Piomelli, U., Moin, P., and Cabot, W. H., "A dynamic subgrid-scale eddy viscosity model," *Physics of Fluids A*, Vol. 3, 1991, pp. 1760-1765.
- [9] Moin, P., Squires, W., Cabot, W. H., and Lee, S., "A dynamic subgrid-scale model for compressible turbulence and scalar transport," *Physics of Fluids A*, Vol. 3, 1991, pp. 2746-2757.
- [10] Lilly, D. K., "A proposed modification of the Germano subgrid-scale closure method," *Physics of Fluids A*, Vol. 3, 1992, pp. 633-635.
- [11] Thomas, P. D., and Lombard, C. K., "Geometric conservation law and its application to flow computations on moving grids," *AIAA Journal*, Vol. 17(10), 1979, pp. 1030-1037.
- [12] Lele, S. k., "Compact finite difference schemes with spectral-like resolution," *Journal of Computational Physics*, Vol. 103, Issue 1, 1992, pp. 12-42.
- [13] Cook, A. W., and Cabot, W. H., "A high-wavenumber viscosity for high-resolution numerical methods," *Journal of Computational Physics*, Vol. 195, Issue 2, 2004, pp. 594-601.

- [14] Cook, A. W., and Cabot, W. H., "Hyperviscosity for shock-turbulence interactions," *Journal of Computational Physics*, Vol. 203, Issue 2, 2005, pp. 379-385.
- [15] Cook, A. W., "Artificial fluid properties for large-eddy simulation of compressible turbulent mixing," *Physics of Fluids*, Vol. 19, Issue 5, 2007, 055103.
- [16] Fiorina, B., and Lele, S. K., "An artificial nonlinear diffusivity method for supersonic reacting flows with shocks," *Journal of Computational Physics*, Vol. 222, Issue 1, 2007, pp. 246-264.
- [17] Kawai, S., and Lele, S. K., "Localized artificial diffusivity scheme for discontinuity capturing on curvilinear meshes," *Journal of Computational Physics*, Vol. 227, Issue 22, 2008, pp. 9498-9526.
- [18] Colucci, P. J., Jaber, F. A., Givi, P., and Pope, S. B., "Filtered Density Function for Large Eddy Simulation of Turbulent Reacting Flows," *Physics of Fluids*, Vol. 10, No. 2, 1998, pp. 499-515.
- [19] Jaber, F. A., Colucci, P. J., James, S., Givi, P., and Pope, S. B., "Filtered Mass Density Function For Large Eddy Simulation of Turbulent Reacting Flows," *Journal of Fluid Mechanics*, Vol. 401, Dec. 1999, pp. 85-121.
- [20] O'Brien, E. E., "*The probability density function (PDF) approach to reacting turbulent flows*," (ed. P. A. Libby and F. A. Williams) Chap. 5, pp. 185-218, 1980, Springer.
- [21] Dopazo, C., and O'Brien, E. E., "Statistical treatment of non-isothermal reactions in turbulent," *Combustion Science and Technology*, Vol. 13, 1976, pp. 99-112.
- [22] Borghi, R., "Turbulent combustion modeling," *Progress in Energy and Combustion Science*, Vol. 14, 1988, pp. 245-292.
- [23] Delarue, B. J., and Pope, S. B., "Application of PDF methods to compressible turbulent flows," *Physics of Fluids*, Vol. 9, No. 9, 1997, pp. 2704-2715.
- [24] Faeth, G. M., "Mixing, transport and combustion in sprays," *Progress in Energy and Combustion Science*, Vol. 13, 1987, pp. 293-304.
- [25] Baumgarten, C., "Mixture Formation in Internal Combustion Engines," Springer-Verlag, Berlin, Heidelberg, 2006.
- [26] Miller, R. S. and Bellan, J., "Direct numerical simulation of a coned three-dimensional gas mixing layer with one evaporating," hydrocarbon-droplet-laden stream, *Journal of Fluid Mechanics*, Vol. 384, 1999, pp. 293-338.
- [27] Pope, S. B., "PDF methods for turbulent reactive flows," *Progress in Energy and Combustion Science*, Vol. 11, 1985, pp. 119-192.

- [28] Gardiner, W., *"Handbook of Stochastic Methods,"* Springer-Verlag, New York, 1990.
- [29] Karlin, S., and Taylor, H. M., *"A Second Course in Stochastic Processes,"* Academic Press, New York, 1981.
- [30] van Leer, B., "Towards the Ultimate Conservative Difference Scheme. V. A Second Order Sequel to Godunov's Method," *Journal of Computational Physics*, Vol. 32, 1979, pp. 101-136.
- [31] Li, Z., Yaldizli, M., and Jaber, F. A., "Filtered Mass Density Function for Numerical Simulations of Spray Combustion," *AIAA paper*: 2008-511, 2008.
- [32] Pope, S. B., *"Turbulent Flows,"* Cambridge University Press, Cambridge, UK, 2000.
- [33] Poinso, T., and Veynante, D., *"Theoretical and Numerical Combustion,"* R. T. Edwards, Inc., Philadelphia, PA, 2001.
- [34] Peters, N., *"Turbulent Combustion,"* Cambridge University Press, Cambridge, UK, 2000.
- [35] Fox, R. O., *"Computational Models for Turbulent Reacting Flows,"* Cambridge University Press, Cambridge, UK, 2003.
- [36] Oran, E. S., and Boris, J. P., *"Numerical Simulation of Reactive Flows,"* Cambridge University Press, New York, NY, 2nd edition, 2001.
- [37] Williams, F. A., *"Combustion Theory,"* The Benjamin/Cummings Publishing Company, Menlo Park, CA, 2nd edition, 1985.
- [38] Bilger, R. W., "Future Progress in Turbulent Combustion Research," *Progress in Energy and Combustion Science*, Vol. 26, Issues 4-6, 2000, pp. 367-380.
- [39] Menon, S., "Subgrid Combustion Modelling for Large-Eddy Simulations," *International Journal of Engine Research*, Vol. 1, No. 2, 2000, pp. 209-227.
- [40] Candel, S., Thevenin, D., Darabiha, N., and Veynante, D., "Progress in Numerical Combustion," *Combustion Science and Technology*, Vol. 149, No. 1-6, 1999, pp. 297-337.
- [41] Vanteyne, D., and Vervisch, L., "Turbulent Combustion Modeling," *Progress in Energy and Combustion Science*, Vol. 28, Issue 3, 2002, pp. 193-301.
- [42] Givi, P., "Filtered Density Function for Subgrid Scale Modeling of Turbulent Combustion," *AIAA Journal*, Vol. 44, No. 1, 2006, pp. 16-23.
- [43] Haworth, D. C., "Progress in probability density function methods for turbulent reacting flows," *Progress in Energy and Combustion Science*, Vol. 36, Issue 2, 2010, pp. 168-259.

- [44] Pope, S. B., "Computations of turbulent combustion: Progress and challenges," *Proceedings of Combustion Institute*, Vol. 23, 1990, pp. 591-612.
- [45] Gao, F., and O'Brien, E. E., "A Large Eddy Scheme for Turbulent Reacting Flows," *Physics of Fluids A*, Vol. 5, No. 6, 1993, pp. 1282-1284.
- [46] James, S., and Jaber, F. A., "Large Scale Simulations of Two-Dimensional Non-premixed Methane Jet Flames," *Combustion and Flame*, Vol. 123, Issue 4, 2000, pp. 465-487.
- [47] Gicquel, L. Y. M., Givi, P., Jaber, F. A., and Pope, S. B., "Velocity filtered density function for large eddy simulation of turbulent flows," *Physics of Fluids*, Vol. 14, No. 3, 2002, pp. 1196-1213.
- [48] Sheikhi, M. R. H., Drozda, T. G., Givi, P., and Pope, S. B., "Velocity-scalar filtered density function for large eddy simulation of turbulent flows," *Physics of Fluids*, Vol. 15, No. 8, 2003, pp. 2321-2337.
- [49] Sheikhi, M. R. H., Givi, P., and Pope, S. B., "Velocity-scalar filtered mass density function for large eddy simulation of turbulent flows," *Physics of Fluids*, Vol. 19, No. 9, 2007, pp. 095106.
- [50] Nik, M. B., Yilmaz, S. L., Sheikhi, M. R. H., Givi, P., and Pope, S. B., "Simulation of Sandia Flame D Using Velocity-Scalar Filtered Density Function," *AIAA Journal*, Vol. 48, No. 7, 2010, pp. 1513-1522.
- [51] Nik, M. B., Yilmaz, S. L., Sheikhi, M. R. H., and Givi, P., "Grid Resolution Effects on VSFMD/LES," *Flow Turbulence Combustion*, 2010, DOI 10.1007/s10494-010-9272-5.
- [52] Sheikhi, M. R. H., Givi, P., and Pope, S. B., "Frequency-velocity-scalar filtered mass density function for large eddy simulation of turbulent flows," *Physics of Fluids*, Vol. 21, No. 7, 2009, pp. 075102.
- [53] Yaldizli, M., Mehravaran, K., and Jaber, F. A., "Large-eddy simulations of turbulent methane jet flames with filtered mass density function," *International Journal of Heat Mass Transfer* Vol. 53, Issues 11-12, pp. 2551-2562.
- [54] Yilmaz, S. L., Nik, M. B., Givi, P., and Strakey, P. A., "Scalar Filtered Density Function for Large Eddy Simulation of a Bunsen Burner," *Journal of Propulsion and Power*, Vol. 26, No. 1, 2010, pp. 84-93.
- [55] Afshari, A., Almeida, T., Mehravaran, K., and Jaber, F. A., "Large Scale Simulations of Turbulent Combustion and Propulsion Systems," *Proceedings of the seventeen ONR propulsion meeting*, 2004.
- [56] Yaldizli, M., Li Z., and Jaber, F. A., "A New model for Large Eddy Simulations of Multi-Phase Turbulent Combustion," *AIAA paper*: 2007-5752, 2007.

- [57] Banaeizadeh, A., Afshari, A., Schock, H. and Jaber, F. A., "Large eddy simulations of turbulent flows in IC engines," *ASME Paper: DETC2008-49788*, 2008.
- [58] Allen, C., Mittal, G., Sung, C. J., Toulson, E., and Lee, T., "An Aerosol Rapid Compression Machine for Studying Energetic-Nanoparticle-Enhanced Combustion of Liquid Fuels," *Proceedings of Combustion Institute*, 33, in press, 2010.
- [59] Mittal, G., and Sung, C.-J., "Aerodynamics inside a rapid compression machine," *Combustion and Flame*, Vol. 145, 2006, pp. 160-180.
- [60] Sod, G. A., "A survey of several finite difference methods for systems on non-linear hyperbolic conservation laws," *Journal of Computational Physics*, Vol. 27, Issue 1, 1978, pp. 1-31.
- [61] Drummond, J. P., Diskin, G. S., and Cutler, A. D., "Fuel-air mixing and combustion in scramjets," *AIAA paper: AIAA-2002-3878*, 2002.
- [62] Cutler, A. D., Diskin, G. S., Drummond, J. P., and White, J. A., "Supersonic Coaxial Jet Experiment for Computational Fluid Dynamics Code Validation," *AIAA Journal*, Vol. 44, No. 3, 2006, pp. 585-592.
- [63] Mohebbi, M., "Large-eddy simulation of NASA LaRC coaxial He-O₂/AIR jet," M.S. thesis, University of Pittsburgh, 2007.
- [64] Griffiths, J. F., Jiao, Q., Kordylewski, W., Schreiber, M., Meyer, J., and Knoche, K. F., "Experimental and numerical studies of Di-tert-butyl Peroxide combustion at high pressures in a rapid compression machine," *Combustion and flame*, Vol. 93, 1993, pp. 303-315.
- [65] Lee, D., and Hochgreb, S., "Rapid compression machines: heat transfer and suppression of corner vortex," *Combustion and flame*, Vol. 114, 1998, pp. 531-545.
- [66] Clarkson, J., Griffiths, J. F., Macnamara, J. P., and Whitaker, B. J., "Temperature fields during the development of combustion in a rapid compression machine," *Combustion and flame*, Vol. 125, 2001, pp. 1162-1175.
- [67] Wrmel, J., and Simmie, J. M., "CFD studies of a twin-piston rapid compression machine," *Combustion and flame*, Vol. 141, Issue 4, 2005, pp. 417-430.
- [68] Mittal, G., Raju, M. P., and Sung, C.-J., "Computational fluid dynamics modeling of the hydrogen ignition in a rapid compression machine," *Combustion and flame*, Vol. 155, 2008, pp. 417-428.
- [69] Mittal, G., Raju, M. P., and Sung, C.-J., "CFD modeling of two-stage ignition in a rapid compression machine: Assessment of zero-dimensional approach *Combustion and Flame*," Vol. 157, Issue 7, 2010, pp. 1316-1324.

- [70] Verzicco, R., Mohd-Yusof, J., Orlandi, P., and Haworth, D. C., "LES in complex geometric using boundary body forces," *Proceedings of the Summer Program of the Center for Turbulence Research, Stanford University/NASA Ames Center for Turbulence Research*, 1998, pp. 171-186.
- [71] Haworth, D. C., "Large-eddy simulation of In-Cylinder Flows," *Oil Gas Science and Technology*, Vol. 54(2), 1999, pp. 175-185.
- [72] Haworth, D. C., and Jansen, K., "Large-eddy simulation on unstructured deformation meshes: towards reciprocating IC engines," *Computers & Fluids*, Vol. 29, 2000, pp. 493-524.
- [73] Verzicco, R., Mohd-Yusof, J., Orlandi, P., and Haworth, D. C., "Large Eddy Simulation in complex geometric configuration using boundary body forces," *AIAA Journal*, Vol. 38(3), 2000, pp. 427-433.
- [74] Celik, I., Yavuz, I., and Smirnov, A., "Large eddy simulations of in-cylinder turbulence for internal combustion engines: a review," *International Journal of Engine Research*, Vol. 2(2), 2001, 119-148.
- [75] Lee, D., Pomraning, E., and Rutland, C. J., "LES Modeling of Diesel Engines," *SAE paper*: 2002-01-2779, 2002.
- [76] Sone, K., and Menon, S., "Effect of Subgrid Modeling on the In-Cylinder Unsteady Mixing Process in a Direct Injection Engine," *Journal of Engineering for Gas Turbines and Power*, Vol. 125(2), 2003, pp. 435-443.
- [77] Moureau V., Barton I. Angelberger C. and Poinso T., Towards Large Eddy Simulation in Internal-Combustion: simulation of a compressed tumble flow, *SAE paper*: 2004-01-1995, 2004.
- [78] Thobois, L., Rymer, G., Souleres, T., and Poinso, T., "Large Eddy Simulation for the prediction of aerodynamics in IC engines," *International Journal of Vehicle Design*, Vol. 39(4), 2005, pp. 368-382.
- [79] Dugue, V., Gauchet, N., and Veynante, D., "Applicability of Large Eddy Simulation to the Fluid Mechanics in a Real Engine Configuration by Means of an Industrial Code," *SAE Technical paper*: 2006-01-1194, 2006.
- [80] Jhavar, R., and Rutland, C. J., "Using Large Eddy Simulations to study mixing effects in early injection diesel engines combustion," *SAE Technical paper*: 2006-01-0871, 2006.
- [81] Richard, S., Colin, O., Vermorel, O., Benkenida, A., Angelberger C., Veynante, D., "Towards large eddy simulation of combustion in spark ignition engines," *Proceedings of the Combustion Institute*, Vol. 31, 2007, pp. 3059-3066.
- [82] A Banaeizadeh , Z Li and FA. Jaber, Compressible Scalar FMDF Model for Large-Eddy Simulations of High speed Turbulent Flows, submitted to AIAA.

- [83] Okong'o, N., and Bellan, J., "Consistent Large Eddy Simulation of a Temporal Mixing Layer Laden With Evaporating Drops. Part 1: Direct Numerical Simulation, Formulation, and A priori Analysis," *Journal of Fluid Mechanics*, Vol. 499, 2004, pp. 1-47.
- [84] Leboissetier, A., and Okong'o, N., and Bellan, J., "Consistent Large Eddy Simulation of a Temporal Mixing Layer Laden With Evaporating Drops. Part 2: A Posteriori Modeling," *Journal of Fluid Mechanics*, Vol. 523, 2005, pp. 37-78.
- [85] Sankaran, V., and Menon, S., "LES of Spray Combustion in Swirling Flows," *Journal of Turbulence*, Vol. 3, 2002, pp. 1-23.
- [86] Patel, N., Kirtas, M., Sankaran, V., and Menon S., "Simulation of spray combustion in a lean-direct injection combustor," *Proceedings of the Combustion Institute*, Vol. 3, 2007, pp. 2327-2334.
- [87] Mahesh, K., Constantinescu, G., Apte, S. V., Iaccarino, G., Ham, F., and Moin, P., "Large-Eddy Simulation of Reacting Turbulent Flows in Complex Geometries," *Journal of Applied Mechanics*, Vol. 73, 2006, pp. 374-381.
- [88] Ham, F., Apte, S. V., Iaccarino, G., Wu, X., Herrmann, M., Constantinescu, G., Mahesh, K., and Moin, P., "Unstructure LES of reacting multiphase flows in realistic gas-turbine combustors," Center for Turbulence Research Annual Research Briefs, 2003, Stanford University, Stanford, CA.
- [89] Patel, N., and Menon S., "Simulation of spray-turbulent-flame interactions in a lean direct injection combustor," *Combustion and Flame*, Vol. 153, Issues 1-2, 2008, pp. 228-257 .
- [90] Turns, S., "An Introduction to Combustion: Concepts and Applications," McGraw Hill professional, second edition, 1999.
- [91] Siebers, D., "Liquid-Phase Fuel Penetration in Diesel Sprays," *SAE Technical paper*: 980809, 1998.
- [92] Chan, M., Das, S., Reitz, R. D., "Modeling Multiple Injection and EGR Effects on the Diesel Engine Emission," *SAE Technical paper*: 972864, 1997.
- [93] Beale, J. C., and Reitz, R. D., "Modeling spray atomization with the Kelvin-Helmholtz/Rayleigh-Taylor hybrid model," *Atomization and Sprays*, Vol. 9, 1999, pp. 623-650.
- [94] Stiesch, G., Merker, G.P., Tan Z., and Reitz, R.D., "Modeling the Effect of Split Injections on DISI Engine Performance," *SAE Technical paper*: 2001-01-0965, 2001.
- [95] El Tahry, S. H., Haworth D. C., "Directions in turbulence modeling for in-cylinder flows in reciprocating IC engines," *AIAA Journal of Propulsion and Power*, Vol. 8, 1992, pp. 1040-1048.

- [96] Reynolds, W. C., "Modeling of fluid motions in engines-an introductory review," In "Combustion Modeling in Reciprocating Engines," (Eds. N. Mattavi and C. A. Amann), Plenum Press, New York, 1980.
- [97] Naitoh, K., Itoh, T., Takagi, Y. and Kuwahara, K., "Large eddy simulation of premixed-flame in engine based on the multi-level formulation and the renormalization group theory," *SAE Technical Paper*: 920590, 1992.
- [98] O'Rourke, P. J., and Sahota, M. S., "A variable explicit/implicit numerical method for calculating advection on unstructured meshes," *Journal of Computational Physics*, Vol. 143, 1998, pp. 312-345.
- [99] Morse, A. P., Whitelaw, J. H., and Yianneskia, M., "Turbulent flow measurement by laser Doppler anemometry in a motored reciprocating engine," Imperial College Dept. Mech. Eng. Report FS/78/24, 1978.
- [100] Mohd-Yusof, J., "Interaction of Massive Particles with Turbulence," PhD Thesis, Cornell university, 1996.
- [101] Amsden, A., KIVA-3: A KIVA program with block structured mesh for complex geometries, Los Alamos National Laboratory Report LA-12503-MS, 1993.
- [102] Menon, S., Yeung, P. K., and Kim, W., ".Effect of Subgrid Models on the computed interscale energy transfer of isotropic turbulence," *Computers & Fluids*, Vol. 25(2), 1996, pp. 165-180.
- [103] Lee, D., and Rutland, C. J., "Probability Density Function Combustion Modeling of Diesel Engines," *Combustion Science and Technology*, Vol. 174(10), 2002, pp 19-54.
- [104] . Graftieaux, L., Michard, M., and Grosjean, N., "Combining PIV, POD and vortex identification algorithms for the study of unsteady turbulent swirling flows," *Measurement Science and Technology*, Vol. 12, 2001, pp. 1422-1429.
- [105] PROSTAR Version 3.103.521, Copyright 1988-2002, Computational Dynamics, Ltd.
- [106] Devesa, A., Moreau, J., Hlie, J., Faivre, V., and Poinso, T., "Initial conditions for Large Eddy Simulations of piston engines flows," *Computers & Fluids*, Vol. 36(4), 2007, pp. 701-713.
- [107] Fraser, R. A., and Bracco, F. V., "Cycle-resolved LDV integral length scale - Measurements investigating clearance height scaling, isotropy and homogeneity in an IC engine," *SAE Technical paper*: 890615, 1989.
- [108] Fraser, R. A., and Bracco, F. V., "Cycle-resolved LDV integral length scale measurements in an IC engine," *SAE Technical paper*: 880381, 1988.

- [109] Lacaze, G., Richardson, E., and Poinso, T., "Large eddy simulation of spark ignition in a turbulent methane jet," *Combustion and Flame*, Vol. 156, Issue 10, 2009, pp. 1993-2009.
- [110] Hung, D. L. S., Zhu, G. G., Winkelmann, J. R., Stuecken, T., Schock, H., and Fedewa, A., "A High Speed Flow Visualization Study of Fuel Spray Pattern Effect on Mixture Formation in a Low Pressure Direct Injection Gasoline Engine," *SAE Technical paper*: 2007-01-1411, 2007.
- [111] Hung, D. L. S., Zhu, G. G., and Schock, H. J., "Time-Resolved Measurements of In-Cylinder Fuel Spray and Combustion Characteristics using High-Speed Visualization and Ionization Sensing," *ILASS Americas*, 22nd Annual Conference on Liquid Atomization and Spray Systems, Cincinnati, OH, May 2010.
- [112] Srivastava, S., Schock, H. J., Jaber, F. A., and Hung, D. L. S., "Numerical Simulation of a Direct-Injection Spark-Ignition Engine with Different Fuels," *SAE Technical paper*: 2009-01-0325, 2009.
- [113] Srivastava, S., Jaber, F. A., Schock, H. J., and Hung, D. L. S., "Experimental and Computational Analysis of Fuel Mixing in a Low Pressure Direct Injection Gasoline Engine," *ICLASS 2009*, 11th Triennial International Annual Conference on Liquid Atomization and Spray Systems, Vail, Colorado USA, July 2009
- [114] Su, T. F., Patterson, M., Reitz, R. D., "Experimental and Numerical Studies of High Pressure Multiple Injection Sprays," *SAE Technical paper*: 960861, 1996.
- [115] Patterson, M., and Reitz, R. D., "Modeling the Effect of Fuel Spray Characteristics on the Diesel Engine Combustion and Emission," *SAE Technical paper*: 980131, 1998.